MICROCOPY RESOLUTION TEST CHART

NATIONAL BUREAU OF STANDARDS-1963-A

AWFAL-TR-87-3112

LOW DENSITY REAL GAS FLOWS ABOUT HYPERSONIC VEHICLES

J. J. Hoffman
R. S. Wong
T. R. Bussing
S. F. Birch

Boeing Aerospace Company
CFD Group/Engineering Technology
P.O. Box 3999
Seattle, Washington 98124

DTIC
ELECTE
MAY 05 1988
D

March 1988

Interim Report for Period September 1986 to September 1987

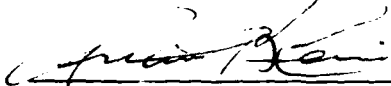Approved for public release; distribution is unlimited.

88   5 02 240

NOTICE

When Government drawings, specifications, or other data are used for any purpose other than in connection with a definitely Government-related procurement, the United States Government incurs no responsibility or any obligation whatsoever. The fact that the Government may have formulated or in any way supplied the said drawings, specifications, or other data, is not to be regarded by implication, or otherwise in any manner construed, as licensing the holder, or any other person or corporation; or as conveying any rights of permission to manufacture, use, or sell any patented invention that may in any way be related thereto.

This report has been reviewed by the Office of Public Affairs (ASD/PA) and is releaseable to the National Technical Information Service (NTIS). At NTIS, it will be available to the general public, including foreign nations.

This technical report has been reviewed and is approved for publication.

ARTHUR B. LEWIS
Project Engineer
High Speed Aero Performance Branch

VALENTINE DAHLEM, Chief
High Speed Aero Performance Branch
Aeromechanics Division

ALFRED C. DRAPER, Acting Chief
Aeromechanics Division

REPORT DOCUMENTATION PAGE

1a. REPORT SECURITY CLASSIFICATION UNCLASSIFIED		1b. RESTRICTIVE MARKINGS			
2a. SECURITY CLASSIFICATION AUTHORITY		3. DISTRIBUTION/AVAILABILITY OF REPORT Approved for public release. Distribution is unlimited.			
2b. DECLASSIFICATION/DOWNGRADING SCHEDULE					
4. PERFORMING ORGANIZATION REPORT NUMBER(S)		5. MONITORING ORGANIZATION REPORT NUMBER(S) AFWAL-TR-87-3112			
6a. NAME OF PERFORMING ORGANIZATION CFD Group/Engineering Technology Organization	6b. OFFICE SYMBOL (If applicable)	7a. NAME OF MONITORING ORGANIZATION			
6c. ADDRESS (City, State and ZIP Code) Boeing Aerospace Company P.O. Box 3999 Seattle, WA 98124		7b. ADDRESS (City, State and ZIP Code) Wright-Patterson Air Force Base Ohio 45433-6553			
8a. NAME OF FUNDING/SPONSORING ORGANIZATION	8b. OFFICE SYMBOL (If applicable)	9. PROCUREMENT INSTRUMENT IDENTIFICATION NUMBER F33615-86-C-3006			
8c. ADDRESS (City, State and ZIP Code)		10. SOURCE OF FUNDING NOS.			

		PROGRAM ELEMENT NO.	PROJECT NO.	TASK NO.	WORK UNIT NO.
		62201F	2404	07	91

11. TITLE *(Include Security Classification)*
Low Density Real Gas Flows about Hypersonic Vehicles

12. PERSONAL AUTHOR(S)
Hoffman, J.J., Wong, R.S., Bussing, T.R., Birch, S.F.

13a. TYPE OF REPORT Interim	13b. TIME COVERED FROM 86/9/25 TO 87/9/25	14. DATE OF REPORT (Yr., Mo., Day) March 1988	15. PAGE COUNT 109

16. SUPPLEMENTARY NOTATION

17.	COSATI CODES		18. SUBJECT TERMS (Continue on reverse if necessary and identify by block number)
FIELD	GROUP	SUB. GR.	Chemical reaction model; coupled Navier-Stokes/chemistry;
01	01		Electron density; flux splitting; Gauss-Seidel line relax-
			ation; hypersonic flow, implicit algorithm; Navier-Stokes,

19. ABSTRACT *(Continue on reverse if necessary and identify by block number)* nonequilibrium air chemistry; parallel processing, transport properties.

Phase I results of the development of a computational algorithm for the calculation of low density real gas flows about hypersonic vehicles is documented. Selection of the three components of the computational algorithm (a Navier-Stokes solution algorithm, a chemistry solution algorithm, and vectorization and parallel processing requirements for both algorithms), is described. Development of a nonequilibrium air chemistry reaction model is included, as well as studies of leeside models, turbulence models, and wall catalysis effects appropriate to the hypersonic flows to be considered. Mach 20 test cases were performed using the Navier-Stokes and chemistry algorithms, and a comprehensive sensitivity study was completed for the selection of an air chemistry model. Transport property calculations are also discussed. The components of the computational algorithm developed during Phase I will be assembled during Phase II into a unified computer code capable of accurately and efficiently calculating low density real gas flows about hypersonic vehicles.

20. DISTRIBUTION/AVAILABILITY OF ABSTRACT	21. ABSTRACT SECURITY CLASSIFICATION
UNCLASSIFIED/UNLIMITED ☒ SAME AS RPT. ☐ DTIC USERS ☐	UNCLASSIFIED

22a. NAME OF RESPONSIBLE INDIVIDUAL Arthur B. Lewis	22b. TELEPHONE NUMBER (Include Area Code) (513) 255-3439	22c. OFFICE SYMBOL AFWAL/FIMG

DD FORM 1473, 83 APR EDITION OF 1 JAN 73 IS OBSOLETE.

PREFACE

The work reported herein represents the interim technical report at the completion of Phase I of the Air Force Systems Command, Aeronautical Systems Division contract F33615-86-C-3006 "Low Density Real Gas Flows About Hypersonic Vehicles." The Air Force Project Engineer is Arthur B. Lewis. The work was conducted by the Computational Fluid Dynamics group of the Boeing Aerospace Company (BAC) Engineering Technology Organization. The BAC project manager is Dr. T. C. Nark, and the deputy program manager is Dr. S. F. Birch. BAC technical leads for Phase I were Dr. J. J. Hoffman and R. G. Hopcroft (algorithm) and Dr. T. R. Bussing and R. S. Wong (chemistry).

Accesion For		
NTIS CRA&I		✔
DTIC TAB		☐
Unannounced		☐
Justification		
By		
Distribution /		
Availability Codes		
Dist	Avail and / or Special	
A-1		

DTIC
COPY
INSPECTED
6

TABLE OF CONTENTS

LIST OF ILLUSTRATIONS

LIST OF ILLUSTRATIONS (Continued)

LIST OF ILLUSTRATIONS (Concluded)

TABLES

I. INTRODUCTION

Renewed interest in hypersonic flow calculations after nearly 20 years of reduced activity has revealed that our current calculation capability is effectively limited to inviscid flows or relatively benign viscous flows. Real hypersonic flows, however, have significant viscous and nonequilibrium chemistry effects. In many cases, the viscous layer constitutes a large fraction of the shock layer, and chemical nonequilibrium effects are strong.

There are currently no known computational analysis programs which can adequately and efficiently describe the low density real gas flows about hypersonic vehicles. It is generally accepted that, for continuum flows, the full Navier-Stokes equations accurately describe the fluid dynamic system. Most current computational programs, however, are generally based on some reduced form of the Navier-Stokes equations, such as the thin layer Navier-Stokes (TLNS), parabolized Navier-Stokes (PNS), and reduced Navier-Stokes (RNS) equations. Techniques based on these reduced equation sets necessarily contain simplifying assumptions which may invalidate their use for many problems of current interest. Additionally, many of the techniques based on the reduced equation sets are not suitable for including reacting gas chemistry effects.

The goal of the current contract effort is directed at producing a computer code which can accurately and efficiently predict trends in heating rates, pressures, forces, and moments on complex shapes in low-density flow at high Mach numbers, and will provide a realistic means for identifying real gas effects to assist in optimizing vehicle aerodynamics for hypersonic flight. This program is based on a coupled, three-dimensional, full Navier-Stokes/chemistry solution algorithm, and will solve the fluid dynamic and chemistry fields about hypersonic vehicles 150-200 nose radii long, with a target computational time of one hour.

The contract is divided into two phases: (I) Development of a Flow Model and Computational Algorithm, and (II) Program Development. The work reported herein describes the status of the contract at the completion of Phase I. Phase I consisted of six tasks: (1) computational algorithm, (2) leeside effects, (3) development of a chemical reaction model, (4) selection of reaction rates and equilibrium constants, (5) turbulence models, and (6) wall catalysis. Phase I results for Task (1) will be described in Section II, while results for Tasks (3) and (4) will be described in Section III, and results for Tasks (2) and (6) will be discussed in Section IV. Section V presents conclusions from Phase I results, and recommendations based on these results.

The work accomplished in Phase I, and reported in this technical report, forms a strong basis for the Phase II program development effort, and will result in a computer code which will accurately and efficiently calculate low density real gas flows about hypersonic vehicles.

II. COMPUTATIONAL ALGORITHM

2.1 INTRODUCTION

2.1.1 Statement of Work

Contract Task 4.2.1, "Computational Algorithm", required development of a computational algorithm for the study of low density real gas flows. The algorithm development consisted of three components: (1) a solution algorithm for the fluid dynamic (Navier-Stokes) equations, (2) a solution algorithm for appropriate reacting gas chemistry equations, and (3) vectorization and parallel processing considerations for the algorithms in (1) and (2). As stated by the request for proposal (RFP), the fluid dynamics of the shock layers and leeside effects requires full diffusion terms in the Navier-Stokes (NS) equations. Additionally, the real gas chemistry effects requires tracking of electron densities as well as species in the flowfield. The resulting complexity of the coupled NS/chemistry equations requires that parallel processing and vectorization of the algorithms be utilized to improve the runtime of the solution procedure.

2.1.2 Goals

The goal of the computational algorithm task was to develop NS and chemistry algorithms which could be used to accurately and efficiently calculate the low density real gas flowfield about hypersonic vehicles 150 to 200 nose radii long. Accurate solution of the fluid dynamics of such flows requires resolution of shocks, boundary layers, and leeside effects, while accurate solution of chemistry effects requires resolution of species concentrations and electron densities.

2.1.3 Approach

The approach selected for the computational algorithm task of Phase I consisted of

developing the NS solution algorithm and the chemistry algorithm separately (using existing codes), while simultaneously performing an analysis of parallel processing and vectorization requirements for both algorithms. Prototype NS and chemistry algorithms based on the MacCormack implicit algorithm (Refs. 1, 2) were chosen for further development. The selection of these prototype algorithms will be discussed in detail in Sections 2.2 and 2.3.

Phase I development of the NS algorithm consisted of demonstrating the use of the MacCormack implicit algorithm for calculating high Mach number flows. Chemistry algorithm development during Phase I consisted of evaluating MacCormack's (Ref. 2) two-dimensional (2D) high mach number calculations, studying the extension of this algorithm to three-dimensions, and studying the coupling of the chemistry algorithm with the NS algorithm. Vectorization and parallel processing requirements were studied throughout the course of Phase I, and included evaluations of hardware and software systems. Hardware evaluations of a number of different computing machines were performed, and multiprocessing software was also evaluated. The components of the computational algorithm (NS algorithm, chemistry algorithm, vectorization and parallel processing requirements) are described separately in Sections 2.2, 2.3, and 2.4, respectively. The intent here is to combine the results of these studies during the Phase II program development effort.

2.1.4 Phase I Computational Algorithm Summary

The Phase I computational algorithm development resulted in a NS algorithm capable of calculating hypersonic flows, and a chemistry algorithm compatible with the NS algorithm also capable of calculating hypersonic flows. Both algorithms have calculated flows about a blunt body near Mach 20. The hypersonic calculations are presented in Sections 2.2 and 2.3. Computer hardware and software evaluations in Phase I assessed the state-of-the-art in vectorization and parallel processing, and parts of the prototype NS algorithm were vectorized and multiprocessed. These results are discussed in Section 2.4.

4

2.2 NAVIER-STOKES SOLUTION ALGORITHM

2.2.1 Background

Accurate calculation of the reacting gas flowfield about a hypervelocity vehicle at high altitude requires an accurate description of the fluid dynamics of the flowfield. The fluid dynamics of hypersonic flows are characterized by thin shock layers which can be fully viscous. The viscous region affects the shock structure, which in turn affects the inviscid flow, leading to strong three-dimensional (3D) viscous/inviscid interactions (Refs. 3, 4). Some form of the Navier-Stokes equations must be used to model the flow since viscous effects will be important.

There are a number of different forms of the Navier-Stokes equations currently in use. Four of the most popular include parabolized Navier-Stokes (PNS), reduced Navier-Stokes (RNS), thin layer Navier-Stokes (TLNS), and full Navier-Stokes (FNS). PNS methods assume that upstream influence is negligible, and are therefore not suited for the current study since the strong viscous/inviscid interactions expected in the hypersonic flows of interest will create a strong streamwise dependence. RNS methods attempt to add streamwise dependence to the basic PNS equations through a pressure relaxation technique (Ref. 5). These methods are in general valid only for flows with weak streamwise interaction. For the current study, the extent of streamwise dependence may be large, especially in separated regions on the leeside of the body. Thus, RNS methods are also not suitable for the current study. TLNS methods retain streamwise derivatives, but only retain viscous terms in a direction normal to a surface (Ref. 6). For the problems to be considered in this contract, the three-dimensionality of the viscous shock layer, as well as the leeside separation region, requires that all three components of diffusion be modeled. Thus, TLNS methods will not satisfy the requirements for this contract.

The primary motivation for using any of the above reduced forms of the Navier-Stokes equations (PNS, RNS, TLNS) is the savings in computer time and storage

requirements resulting from such reductions. These reductions are necessarily accompanied by restrictions to their applications, making the reduced forms of the Navier-Stokes equations valid only for a certain range of problems. The current contract objective, to calculate three-dimensional viscous flows with complex viscous/inviscid interactions, does not completely satisfy the requirements for any of the reduced forms described above. Thus, the full Navier-Stokes equations are required to satisfy the objectives of this contract.

Until recently (in the past 10 years), it had been nearly impossible to numerically solve the full Navier-Stokes equations for any realistic aerodynamic configurations, due largely to the prohibitive computer time and storage requirements needed for grids capable of producing accurate flowfield calculations. With the emergence of "super computers", it is becoming feasible to solve the full Navier-Stokes equations for realistic geometries in a cost/time frame competitive with wind tunnel testing. Considering the fact that complex hypersonic flows are difficult, if not impossible, to model in the wind tunnel (and therefore very expensive), it can be seen that numerically solving the full Navier-Stokes equations for real problems of engineering interest is not as forbidding as it had been a decade ago.

Having selected the appropriate equation set (i.e. the full Navier-Stokes equations), it was necessary to select a solution technique. In the past 10-15 years, two solution methods for the full Navier-Stokes equations have received most of the computational fluid dynamics (CFD) community's attention: (1) the approximate factorization alternating direction implicit (ADI) technique of Beam and Warming (Refs. 7, 8), and (2) the implicit unfactored Gauss-Seidel line relaxation technique of MacCormack (Refs. 1, 9).

Approximately factored (ADI) techniques have long been known to suffer a factorization error which severely limits the computational time step, while the unfactored Gauss-Seidel (GS) line relaxation solution technique does not possess such a time step limitation. Additionally, Yee and Shinn (Refs. 10, 11) have noted that "there appears to be no straightforward way of utilizing ADI approaches for nonlinear system

cases with general stiff source terms." One of the primary goals of the current contract is to calculate the reacting gas properties of the flowfield, a calculation characterized by the presence of stiff chemistry source terms. The MacCormack unfactored GS algorithm is readily amenable to the incorporation of coupled chemistry equations with stiff source terms, and has already been demonstrated for 2D flow (Refs. 2, 10).

Based upon the above arguments, the MacCormack implicit unfactored GS line relaxation solution algorithm for the NS equations was selected for development under this contract.

2.2.2 Features of the Proposed Algorithm

The MacCormack implicit algorithm for the NS equations possesses a number of features which make it desirable for the current calculation of low density real gas flows about hypersonic vehicles. These features are summarized in this section.

Arbitrarily Transformed Coordinate System. The MacCormack implicit algorithm is written in terms of generalized curvilinear coordinates, allowing body fitted meshes to be used. Body fitted meshes facilitate geometry definition (even for complex 3D geometries), and also facilitate implementation of boundary conditions.

Arbitrary Boundary Condition Specification. The MacCormack implicit algorithm implements a full range of supersonic boundary conditions, including solid wall no-slip, solid wall free-slip, symmetry, inflow, outflow, and freestream conditions. These boundary conditions are treated implicitly, thereby maintaining the stability and robustness of the basic algorithm.

Full Viscous Terms. As mentioned in the RFP, retention of three components of the viscous terms is critical for accurate calculation of the viscous region in the shock layer, as well as for leeside effects where large-scale separation is expected. In the MacCormack implicit algorithm, full viscous terms are retained in the explicit part of the algorithm (including cross-derivative terms), while the diagonal components of the transformed diffusion terms are retained in the implicit part of the algorithm. The

combined algorithm exhibits the character of full viscous terms, and will allow accurate calculation of the shock layer and leeside effects.

Inviscid Flux Splitting. Finite difference approximations to the NS equations suffer from discretization errors which restrict the stability and robustness of the formulation unless some form of artificial dissipation is added. In the past, artificial dissipation for the NS equations most usually consisted of some fourth order dissipation function, such as that described by Beam and Warming (Ref. 7), or a combination of second and fourth order dissipation, such as that proposed by Jameson (Ref. 12). The disadvantage of such artificial dissipation functions is that they are relatively empirical, and the constants can be adjusted without regard to the physics of the flowfield.

Total Variation Diminishing (TVD) schemes represent another method for adding artificial dissipation to the governing equations. TVD schemes have been shown by Yee (Ref. 13) to be non-oscillatory near strong shocks. TVD techniques are computationally intensive, though, and are not feasible for use in the present study given the computational time constraints specified by the contract.

More recently, there has been renewed interest in the flux splitting procedure of Steger and Warming (Ref. 14). Initially developed for the Euler equations, flux splitting treats the inviscid terms as combinations of forward and backward facing contributions, depending upon the sign of the eigenvectors. In this manner, flux splitting closely models the physics of the flowfield. Additionally, since the difference schemes are one-sided, the formulation is inherently dissipative (for first order flux splitting), thereby eliminating the need for an arbitrary artificial dissipation term. Flux splitting the inviscid fluxes also increases diagonal dominance of the block tridiagonal matrix obtained from the implicit governing equation, thereby enhancing the stability of the tridiagonal matrix inversion.

Gauss-Seidel Line Relaxation Solution Procedure. By utilizing the unfactored block tridiagonal matrix structure obtained by linearizing the implicit governing equation, the MacCormack implicit algorithm does not exhibit the time step restrictions found in the approximate factorization techniques. The block tridiagonal is solved using Gauss-

Seidel (GS) line relaxation, solving a tridiagonal matrix for lines along a prescribed direction. GS sweeps update the solution in the remaining two directions. Convergence for each time step is obtained in approximately two to three iterations (sweeps), due in part to the use of inviscid flux vector splitting which enhances the stability of the solution procedure.

Chemistry Algorithm Compatibility. The basic MacCormack implicit algorithm is capable of incorporating an arbitrary number of chemistry equations. The resulting *fully-coupled system more accurately represents the physics of the system than do* lagged chemistry approaches. Additionally, the implicit treatment of the chemistry equations removes the "stiffness" problem generally associated with explicit solutions to the NS/chemistry equations. The solution procedure retains the GS line relaxation technique described for the NS equations. By generalizing the chemistry equations, an arbitrary number of chemistry equations may be added without affecting the basic solution procedure. Details of the chemistry algorithm will be discussed in Section 2.3.

2.2.3 Implicit Algorithm Development

The MacCormack implicit algorithm for the Navier-Stokes equations without chemistry solves the full set of equations (conservation of mass, x-momentum, y-momentum, z-momentum, and energy) in strong conservation form:

$$\frac{\partial U'}{\partial t} + \frac{\partial F'}{\partial x} + \frac{\partial G'}{\partial y} + \frac{\partial H'}{\partial z} = 0, \tag{1}$$

where

$$U' = \left[\rho, \rho u, \rho v, \rho w, e \right]^T$$

represents the (conserved) solution vector, with ρ = density, u, v, w, = cartesian components of velocity, and e = total energy per unit volume. Here, primes denote the

9

nontransformed (physical) flux vectors, and superscript T denotes the transpose of the solution vector.

The first step in the development of the implicit governing equation is to split the flux vectors F', G', H' into inviscid and viscous contributions:

$$F' = \begin{bmatrix} \rho u \\ \rho u^2 + p \\ \rho uv \\ \rho uw \\ u(e+p) \end{bmatrix} + \begin{bmatrix} 0 \\ -\mu_B\left[\dfrac{\partial u}{\partial x} + \dfrac{\partial v}{\partial y} + \dfrac{\partial w}{\partial z}\right] - 2\mu\dfrac{\partial u}{\partial x} \\ \tau_{xy} \\ \tau_{xz} \\ u\left[-\mu_B\left(\dfrac{\partial u}{\partial x} + \dfrac{\partial v}{\partial y} + \dfrac{\partial w}{\partial z}\right) - 2\mu\dfrac{\partial u}{\partial x}\right] + v\tau_{xy} + w\tau_{xz} - \lambda\dfrac{\partial T}{\partial x} \end{bmatrix} . \quad (1a)$$

$$G' = \begin{bmatrix} \rho v \\ \rho vu \\ \rho v^2 + p \\ \rho vw \\ v(e+p) \end{bmatrix} + \begin{bmatrix} 0 \\ \tau_{yx} \\ -\mu_B\left[\dfrac{\partial u}{\partial x} + \dfrac{\partial v}{\partial y} + \dfrac{\partial w}{\partial z}\right] - 2\mu\dfrac{\partial v}{\partial y} \\ \tau_{yz} \\ u\tau_{yx} + v\left[-\mu_B\left(\dfrac{\partial u}{\partial x} + \dfrac{\partial v}{\partial y} + \dfrac{\partial w}{\partial z}\right) - 2\mu\dfrac{\partial v}{\partial y}\right] + w\tau_{yz} - \lambda\dfrac{\partial T}{\partial y} \end{bmatrix} . \quad (1b)$$

$$H' = \begin{bmatrix} \rho w \\ \rho wu \\ \rho wv \\ \rho w^2 + p \\ w(e+p) \end{bmatrix} + \begin{bmatrix} 0 \\ \tau_{zx} \\ \tau_{zy} \\ -\mu_B\left[\dfrac{\partial u}{\partial x} + \dfrac{\partial v}{\partial y} + \dfrac{\partial w}{\partial z}\right] - 2\mu\dfrac{\partial w}{\partial z} \\ u\tau_{zx} + v\tau_{zy} + w\left[-\mu_B\left(\dfrac{\partial u}{\partial x} + \dfrac{\partial v}{\partial y} + \dfrac{\partial w}{\partial z}\right) - 2\mu\dfrac{\partial w}{\partial z}\right] - \lambda\dfrac{\partial T}{\partial z} \end{bmatrix} . \quad (1c)$$

where the inviscid terms are contained in the left-hand vectors, the viscous terms are contained in the right-hand vectors, and

$$\iota_{xy} = \iota_{yx} = -\mu\left(\frac{\partial u}{\partial y} + \frac{\partial v}{\partial x}\right),$$

$$\iota_{xz} = \iota_{zx} = -\mu\left(\frac{\partial u}{\partial z} + \frac{\partial w}{\partial x}\right), \tag{1d}$$

$$\iota_{yz} = \iota_{zy} = -\mu\left(\frac{\partial v}{\partial z} + \frac{\partial w}{\partial y}\right),$$

with p = pressure, T = temperature, μ = dynamic viscosity, μ_B = $-(\frac{2}{3})\mu$ = bulk viscosity, and λ = coefficient of thermal conductivity. Pressure is related to density and energy through an equation of state, $p = p(\rho, e)$.

Transformed Governing Equations. For grids clustered near a body the cartesian coordinate system in Equation (1) results in a nonuniform grid, and requires special weighting considerations in the finite difference approximations to the governing equations. The preferred procedure is to perform a generalized coordinate transformation from the cartesian (x, y, z) coordinate system to a generalized curvilinear coordinate system (ξ, η, ζ). The transformed governing equations are still written in strong conservation form:

$$\frac{\partial U}{\partial t} + \frac{\partial F}{\partial \xi} + \frac{\partial G}{\partial \eta} + \frac{\partial H}{\partial \zeta} = 0, \tag{2}$$

with the following definitions:

$$U = U'J^{-1},$$

$$F = \left[F'\xi_x + G'\xi_y + H'\xi_z\right]J^{-1},$$

11

$$G = \left[F'\eta_x + G'\eta_y + H'\eta_z \right] J^{-1}, \tag{2a}$$

$$H = \left[F'\zeta_x + G'\zeta_y + H'\zeta_z \right] J^{-1},$$

where $\xi_x, \xi_y, \xi_z, \eta_x, \eta_y, \eta_z, \zeta_x, \zeta_y, \zeta_z$ are metrics of the transformation, J is the Jacobian of the transformation, and the nontransformed (primed) flux vectors are defined in Equation (1). The transformed coordinate system is uniform, and finite differences may be applied directly to the governing equations without weighting functions.

Formulation of the Implicit Governing Equation. The procedure for deriving the implicit governing equation from Equation (2) is summarized below. The derivation is begun by taking the time derivative of Equation (2) and interchanging the order of differentiation. Next, Jacobians of the inviscid flux vectors are taken with respect to the solution vector U, and the viscous flux vectors are written directly in terms of $\partial U/\partial t$. Multiplying by Δt to obtain the delta form of the governing equations yields:

$$\frac{\partial}{\partial t} \left[\Delta t \frac{\partial U}{\partial t} \right] + \left[\frac{\partial}{\partial \xi} A + \frac{\partial}{\partial \xi} \left(F_\xi \frac{\partial}{\partial \xi} + F_\eta \frac{\partial}{\partial \eta} + F_\zeta \frac{\partial}{\partial \zeta} \right) N_f \right] \Delta t \frac{\partial U}{\partial t}$$

$$+ \left[\frac{\partial}{\partial \eta} B + \frac{\partial}{\partial \eta} \left(G_\xi \frac{\partial}{\partial \xi} + G_\eta \frac{\partial}{\partial \eta} + G_\zeta \frac{\partial}{\partial \zeta} \right) N_f \right] \Delta t \frac{\partial U}{\partial t}$$

$$+ \left[\frac{\partial}{\partial \zeta} C + \frac{\partial}{\partial \zeta} \left(H_\xi \frac{\partial}{\partial \xi} + H_\eta \frac{\partial}{\partial \eta} + H_\zeta \frac{\partial}{\partial \zeta} \right) N_f \right] \Delta t \frac{\partial U}{\partial t} = 0, \tag{3}$$

where A, B, C are the Jacobians of the inviscid flux vectors with respect to the solution vector, $F_\xi, F_\eta, F_\zeta, G_\xi, G_\eta, G_\zeta, H_\xi, H_\eta, H_\zeta$, are the nine components of the (transformed) viscous matrices, and N_f is a matrix relating the nonconservative solution vector V ($= [\rho, u, v, w, e_i]^T$) to the conservative solution vector U. Note that the internal energy (e_i) per unit mass is related to the total energy per unit volume (e) by $e = \rho[e_i + \frac{1}{2}(u^2 + v^2 + w^2)]$.

Expanding the time derivative in Equation (3) in a forward difference yields:

$$\frac{\partial}{\partial t}\left[\Delta t \frac{\partial U}{\partial t}\right] = \frac{1}{\Delta t}\left\{\left[\Delta t \frac{\partial U}{\partial t}\right]^{n+1} - \left[\Delta t \frac{\partial U}{\partial t}\right]^{n}\right\}. \tag{4}$$

Defining the following:

$$\Delta U^{n} - \text{explicit change} = \left[\Delta t \frac{\partial U}{\partial t}\right]^{n},$$

$$\text{and } \delta U^{n+1} = \text{implicit change} = \left[\Delta t \frac{\partial U}{\partial t}\right]^{n+1}, \tag{5}$$

and substituting Equations (4) - (5) into Equation (3) yields (after rearranging):

$$\left\{I + \Delta t \left[\frac{\partial}{\partial \xi}A + \frac{\partial}{\partial \xi}\left(F_{\xi}\frac{\partial}{\partial \xi} + F_{\eta}\frac{\partial}{\partial \eta} + F_{\zeta}\frac{\partial}{\partial \zeta}\right)N_{f}\right]\right.$$

$$+ \Delta t \left[\frac{\partial}{\partial \eta}B + \frac{\partial}{\partial \eta}\left(G_{\xi}\frac{\partial}{\partial \xi} + G_{\eta}\frac{\partial}{\partial \eta} + G_{\zeta}\frac{\partial}{\partial \zeta}\right)N_{f}\right]$$

$$\left. + \Delta t \left[\frac{\partial}{\partial \zeta}C + \frac{\partial}{\partial \zeta}\left(H_{\xi}\frac{\partial}{\partial \xi} + H_{\eta}\frac{\partial}{\partial \eta} + H_{\zeta}\frac{\partial}{\partial \zeta}\right)N_{f}\right]\right\}\delta U^{n+1} = \Delta U^{n}, \tag{6}$$

where I is the identity matrix. Equation (6) represents the fully-implicit governing equation for the 3D NS equations.

Flux Splitting Add-on. As was discussed earlier, most finite difference representations of the NS equations require some form of artificial dissipation to maintain numerical stability. Inviscid flux vector splitting has been selected to provide the artificial dissipation, since *splitting more closely models the flow physics* than empirical artificial dissipation functions.

Flux vector splitting is accomplished at the computational cell face level. The flux at each cell face is comprised of two components, one forward facing (associated with

13

positive eigenvalues), and one backward facing (associated with negative eigenvalues). Non-flux-split procedures approximate the flux at a cell face as a single component, effectively central differencing the flux. First order flux splitting schemes forward difference negative eigenvalue flux contributions and backward difference positive eigenvalue flux contributions. For subsonic flows where both positive and negative eigenvectors exist, the procedure is equivalent to the central difference form. For supersonic flows, where the eigenvectors are all the same sign, the flux splitting results in a one-sided difference. This one-sided difference will more effectively capture the physics of shock waves (where discontinuities in properties exist), while at the same time providing the necessary dissipation to stabilize the solution procedure.

Flux splitting is implemented into Equation (6) by first diagonalizing the inviscid flux vectors (**A, B, C**) and splitting the eigenvectors into positive and negative contributions:

$$A = S_A \Lambda_A S_A^{-1} = S_A \left(\Lambda_A^+ + \Lambda_B^- \right) S_A^{-1} = A^+ + A^- ,$$

$$B = S_B \Lambda_B S_B^{-1} = S_B \left(\Lambda_B^+ + \Lambda_B^- \right) S_B^{-1} = B^+ + B^- , \tag{7}$$

$$C = S_C \Lambda_C S_C^{-1} = S_C \left(\Lambda_C^+ + \Lambda_C^- \right) S_C^{-1} = C^+ + C^- ,$$

where **S, S^{-1}** represent the matrices which diagonalize the inviscid flux vectors, Λ represents the diagonalized matrix of eigenvalues, and superscripts + and - indicate positive and negative contributions, respectively. The significance of this splitting operation will become apparent when the governing equations are finite differenced, as the positive contributions will be backward differenced, and the negative contributions will be forward differenced.

Substituting the flux split inviscid terms in Equation (7) into the implicit governing Equation (6) yields the flux split form of the governing equations:

14

$$\left\{ I + \Delta t \left[\frac{\partial}{\partial \xi} A^+ + \frac{\partial}{\partial \xi} A^- + \frac{\partial}{\partial \eta} B^+ + \frac{\partial}{\partial \eta} B^- + \frac{\partial}{\partial \zeta} C^+ + \frac{\partial}{\partial \zeta} C^- \right] \right\} \partial U^{n+1}$$

$$+ \left\{ \Delta t \left[\frac{\partial}{\partial \xi} \left(F_\xi \frac{\partial}{\partial \xi} + F_\eta \frac{\partial}{\partial \eta} + F_\zeta \frac{\partial}{\partial \zeta} \right) N_f \right. \right.$$

$$+ \frac{\partial}{\partial \eta} \left(G_\xi \frac{\partial}{\partial \xi} + G_\eta \frac{\partial}{\partial \eta} + G_\zeta \frac{\partial}{\partial \zeta} \right) N_f$$

$$\left. \left. + \frac{\partial}{\partial \zeta} \left(H_\xi \frac{\partial}{\partial \xi} + H_\eta \frac{\partial}{\partial \eta} + H_\zeta \frac{\partial}{\partial \zeta} \right) N_f \right] \right\} \delta U^{n+1} = \Delta U^n , \tag{8}$$

where the first set of brackets surround the inviscid terms, and the second set of brackets surround the viscous terms. Here, δU^{n+1} represents the implicit change, and ΔU^n represents the explicit change, as defined in Equation (5).

Solution Procedure. The first step in the solution process consists of discretizing the governing equation (Equation (8)) by approximating the derivative terms with finite differences. As noted earlier, the following rules apply to the discretization process: (1) positive inviscid fluxes are backward differenced, (2) negative inviscid fluxes are forward differenced, and (3) viscous fluxes are central differenced. Using these rules, the resulting finite difference approximation to Equation (8) becomes:

$$\left\{ I + \Delta t \left[D_{-\xi} A^+ + D_{+\xi} A^- + D_{-\eta} B^+ + D_{+\eta} B^- + D_{-\zeta} C^+ + D_{+\zeta} C^- \right] \right\} \delta U^{n+1}$$

$$+ \Delta t \left\{ D_{-\xi} \left(F_\xi D_{+\xi} + F_\eta D_{+\eta} + F_\zeta D_{+\zeta} \right) N_f \right.$$

$$+ D_{-\eta} \left(G_\xi D_{+\xi} + G_\eta D_{+\eta} + G_\zeta D_{+\zeta} \right) N_f$$

$$\left. + D_{-\zeta} \left(H_\xi D_{+\xi} + H_\eta D_{+\eta} + H_\zeta D_{+\zeta} \right) N_f \right\} \delta U^{n+1} = \Delta U^n , \tag{9}$$

where D- indicates backward differences, D+ indicates forward differences, and subscripts ξ, η, ζ indicate the difference direction. Note that D+ D- is equivalent to a central difference.

Applying the difference operators to Equation (9) and collecting like terms yields the discretized form of the governing equations:

$$a_1^{n+1} \delta U_{i,j+1,k}^{n+1} + a_0^{n+1} \delta U_{i,j,k}^{n+1} + a_2^{n+1} \delta U_{i,j-1,k}^{n+1} \tag{10}$$

$$+ a_3^{n+1} \delta U_{i+1,j,k} + a_4^{n+1} \delta U_{i-1,j,k} + a_5^{n+1} \delta U_{i,j,k+1} + a_6^{n+1} \delta U_{i,j,k-1} = \Delta U_{i,j,k}^{n} \ ,$$

where the constants a_1 through a_6 are defined as follows:

$$a_0^{n+1} = I + \Delta t \left\{ -\left[A_{i-\frac{1}{2},j,k}^{-} + \left(F_\xi N_f \right)_{i-\frac{1}{2},j,k} \right] + \left[A_{i+\frac{1}{2},j,k}^{+} + \left(F_\xi N_f \right)_{i+\frac{1}{2},j,k} \right] \right.$$

$$-\left[B_{i,j-\frac{1}{2},k}^{-} + \left(G_\eta N_f \right)_{i,j-\frac{1}{2},k} \right] + \left[B_{i,j+\frac{1}{2},k}^{+} + \left(G_\eta N_f \right)_{i,j+\frac{1}{2},k} \right]$$

$$\left. -\left[C_{i,j,k-\frac{1}{2}}^{-} + \left(H_\zeta N_f \right)_{i,j,k-\frac{1}{2}} \right] + \left[C_{i,j,k+\frac{1}{2}}^{+} + \left(H_\zeta N_f \right)_{i,j,k+\frac{1}{2}} \right] \right\} ,$$

$$a_1^{n+1} = \Delta t \left\{ B_{i,j+\frac{1}{2},k}^{-} + \left(G_\eta N_f \right)_{i,j+\frac{1}{2},k} \right\}^{n+1} ,$$

$$a_2^{n+1} = \Delta t \left\{ -B_{i,j-\frac{1}{2},k}^{+} + \left(G_\eta N_f \right)_{i,j-\frac{1}{2},k} \right\}^{n+1} .$$

$$a_3^{n+1} = \Delta t \left\{ A_{i+\frac{1}{2},j,k}^{-} + \left(F_\xi N_f \right)_{i+\frac{1}{2},j,k} \right\}^{n+1} ,$$

$$a_4^{n+1} = \Delta t \left\{ -A_{i-\frac{1}{2},j,k}^{+} + \left(F_\xi N_f \right)_{i-\frac{1}{2},j,k} \right\}^{n+1} ,$$

16

$$a_5^{n+1} = \Delta t \left\{ C_{i,j,k+\frac{1}{2}}^- + \left(H_\xi N_f \right)_{i,j,k+\frac{1}{2}} \right\}^{n+1},$$

$$a_6^{n+1} = \Delta t \left\{ -C_{i,j,k-\frac{1}{2}}^+ + \left(H_\xi N_f \right)_{i,j,k-\frac{1}{2}} \right\}^{n+1},$$

with subscript 1/2 referring to cell faces. Note that only diagonal components of the viscous fluxes (F_ξ, G_η, H_ζ) have been retained in Equation (10). There is no restriction in principle requiring exclusion of the cross-derivative terms; however, the implementation of these terms is difficult due to the coordinate transformation metrics. It is not expected that neglecting the cross-derivative terms on the implicit side of Equation (10) will significantly affect the stability of the implicit algorithm, since full viscous terms are still retained in the calculation of the explicit change (ΔU^n) in Equation (10).

Equation (10) is nonlinear due to the dependence of the coefficients a_0 - a_6 on the solution vector. Solution of Equation (10) is not practical by any current solution technique. Two assumptions are needed to make the solution feasible. First, the coefficients a_0 through a_6 in Equation (10) are linearized to time level n. The resulting equation represents a block septadiagonal, whose solution is still not practical for the problems to be considered in this contract using current solution techniques. Second, selected terms are lagged such that the resulting equation reduces to a block tridiagonal matrix, for which efficient solution techniques do exist.

There are three choices for the tridiagonal structure, corresponding to the three coordinate directions (denoted here as i, j, k). It is desired to utilize the tridiagonal (implicit) solution update along lines normal to the steepest flow gradients, such as will be found normal to a solid wall and across a shock wave. For simplicity, it is assumed here that the direction of steepest gradients is normal to the j = constant lines; the generalization to the other two directions (i, k) is straight forward.

To create a tridiagonal structure in the j-direction, only terms with subscripts (i, j+1, k), (i, j, k), and (i, j-1, k) are retained on the left-hand side of Equation (10).

Noting also that the coefficients a_0 through a_6 have been linearized to time level n, Equation (10) becomes:

$$a_1^n \delta U_{i,j+1,k}^{n+1} + a_0^n \delta U_{i,j,k}^{n+1} + a_2^n \delta U_{i,j-1,k}^{n+1} =$$

$$\Delta U_{i,j,k}^n - a_3^n \delta U_{i+1,j,k}^n - a_4^n \delta U_{i-1,j,k}^n - a_5^n \delta U_{i,j,k+1}^n - a_6^n \delta U_{i,j,k-1}^n \cdot \tag{11}$$

Similar equations may be written in the i and k directions.

Equation (11) represents a block tridiagonal algorithm which is implicit in the j-direction for updating the solution vector $\mathbf{U}$. Due to lagging the i- and k-direction terms, a Gauss-Seidel line relaxation solution procedure is used, with each time step consisting of two or more sweeps in the i- and k-directions, with a tridiagonal matrix solution for each j-line. Experience has shown that two to three sweeps are sufficient to obtain a converged solution for each time step.

MacCormack's baseline implicit algorithm has a predictor-corrector format (Ref. 1), with the following six-step solution process:

a. Calculate the explicit delta (predictor):

$$\Delta U_{i,j,k}^n = -\Delta t \left\{ D_{-\xi} F_{inv}^+ + D_{+\xi} F_{inv}^- + D_{\pm\xi} F_{vis} \right\}$$

$$-\Delta t \left\{ D_{-\eta} G_{inv}^+ + D_{+\eta} G_{inv}^- + D_{\pm\eta} G_{vis} \right\}$$

$$-\Delta t \left\{ D_{-\zeta} H_{inv}^+ + D_{+\zeta} H_{inv}^- + D_{\pm\zeta} H_{vis} \right\} \cdot$$

where D_- indicates backward differences, D_+ indicates forward differences, and $D_\pm$ indicates either a forward or backward difference. Here, subscript inv denotes inviscid terms and subscript vis denotes viscous terms. The differencing scheme for the viscous terms is alternated from the predictor to the corrector step, resulting in (effectively)

central differenced viscous terms. Full viscous terms are retained in the viscous flux vectors. Note that flux splitting has been applied to the inviscid flux terms in the calculation of the explicit delta.

b. Calculate the implicit delta (predictor), by solving Equation (11) for $\delta U_{i,j,k}^{\overline{n+1}}$, where the overbar denotes an intermediate solution.

c. Intermediate (predictor) update:

$$\delta U_{i,j,k}^{n+1} = U_{i,j,k}^{n} + \delta U_{i,j,k}^{\overline{n+1}}$$

d. Calculate explicit delta (corrector), by repeating step (a) with alternated difference directions.

e. Calculate the implicit delta (corrector), by solving Equation (11) for $\delta U_{i,j,k}^{n+1}$.

f. Solution update:

$$U_{i,j,k}^{n+1} = \tfrac{1}{2}\left\{ U_{i,j,k}^{n} + \delta U_{i,j,k}^{\overline{n+1}} + \delta U_{i,j,k}^{n+1} \right\}.$$

As part of this contract effort, a one-step version of the solution algorithm is being investigated. The primary advantage of a one-step solution process is the 50% savings in the computational time associated with the predictor/corrector solution. The one-step solution procedure is summarized below:

a. Calculate explicit delta:

$$\Delta U_{i,j,k}^{n} = -\Delta t \left\{ D_{-\xi}\, F_{inv}^{+} + D_{+\xi}\, F_{inv}^{-} + D_{\pm\xi}\, F_{vis} \right\}$$

$$-\Delta t \left\{ D_{-\eta}\, G_{inv}^{+} + D_{+\eta}\, G_{inv}^{-} + D_{\pm\eta}\, G_{vis} \right\}$$

$$-\Delta t \left\{ D_{-\zeta}\, H_{inv}^{+} + D_{+\zeta}\, H_{inv}^{-} + D_{\pm\zeta}\, H_{vis} \right\},$$

b. Calculate implicit delta for $\delta U_{i,j,k}^{n+1}$ from Equation (11).

c. Update the solution:

$$U_{i,j,k}^{n+1} = U_{i,j,k}^{n} + \delta U_{i,j,k}^{n+1}.$$

Although the one-step procedure described above appears to be a logical choice, a number of issues regarding the correct form of the differencing schemes used in the one-step procedure will need to be addressed. In particular, it is not clear if the central differencing of the viscous terms, which was achieved by alternated one-sided differences in the predictor and corrector steps, must be accomplished in one step, or if the central difference which occurs after every two computational steps (retaining the predictor-corrector format) is sufficient. Additionally, the similarity matrices used to diagonalize the inviscid fluxes must be evaluated at face centers. In the predictor-corrector solution, these centered values are obtained by alternated one-sided approximations in the predictor and corrector steps. Again, the one-step procedure will only obtain a centered value after two computational steps if the original predictor-corrector format is retained. These topics will be addressed during Phase II of this contract.

2.2.6 Test Cases

The flow physics associated with hypersonic low density real gas flows can be broadly categorized into four parts: (1) weak (oblique) shocks, (2) strong (normal) shocks, (3) boundary layer/heat transfer, and (4) chemical nonequilibrium effects. Items (1)-(3) pertain to the fluid dynamics of the flow, and are critical features in the determination of item (4). Two test cases were created in Phase I to evaluate the prototype Navier-Stokes (fluid dynamics) solution algorithm. These cases were selected to attempt to isolate flow features (1) and (2) described above. Test Case 1 consisted of a compression corner, and attempted to isolate a weak (oblique) shock, while Test Case

2 consisted of a 3D/axisymmetric blunt nose region which attempted to isolate a strong (normal) shock. Emphasis at this stage of the contract was on determining whether the prototype NS solution algorithm could accurately predict gross flow features at high Mach numbers. No attempt was made to analyze fine flow details, and for this reason no boundary layer/heat transfer studies were conducted at this time; nor were there any attempts to compare the results obtained from the two test cases to experimental data. It was considered sufficient for present purposes to demonstrate global features of the solver for high Mach number flows.

Test Case 1: Compression Corner. The geometry for the 3D compression corner consisted of a 1 inch (0.0254m) long flat plate followed by an 11.3 degree half-angle ramp. A coarse 50 x 20 mesh, shown in Figure 1, was used in the two-dimensional plane, and 3 grid cells were used in the spanwise direction. The plate width was taken as 0.1 inch. Test conditions for this test case are summarized below.

Mach number:	20.0	
Freestream velocity:	5906 m/s	(19377 ft/s)
Static pressure:	40000 N/m^2	(835lb$_f$/ft^2)
Static temperature:	216.7K	(390°R)

The Reynolds number for this case was 6.2 (10^6), based on the plate length.

The test case assumed an ideal gas, and the wall was considered to be adiabatic.
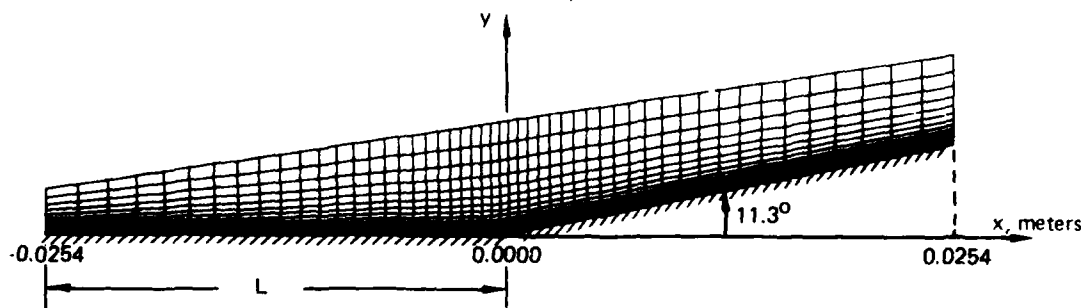
Figure 1. 50 x 20 Grid in Two-Dimensional Plane for Three-Dimensional Compression Corner Oblique Shock Test Case

The solution converged in approximately 80 implicit steps. Parts (a), (b), and (c) of Figure 2 show the Mach, pressure, and temperature contours, respectively. The y-scale has been expanded in Figure 2 for clarity. Note that the calculation predicts the gross

(a) Mach Contours

(b) Pressure Contours

(c) Temperature Contours
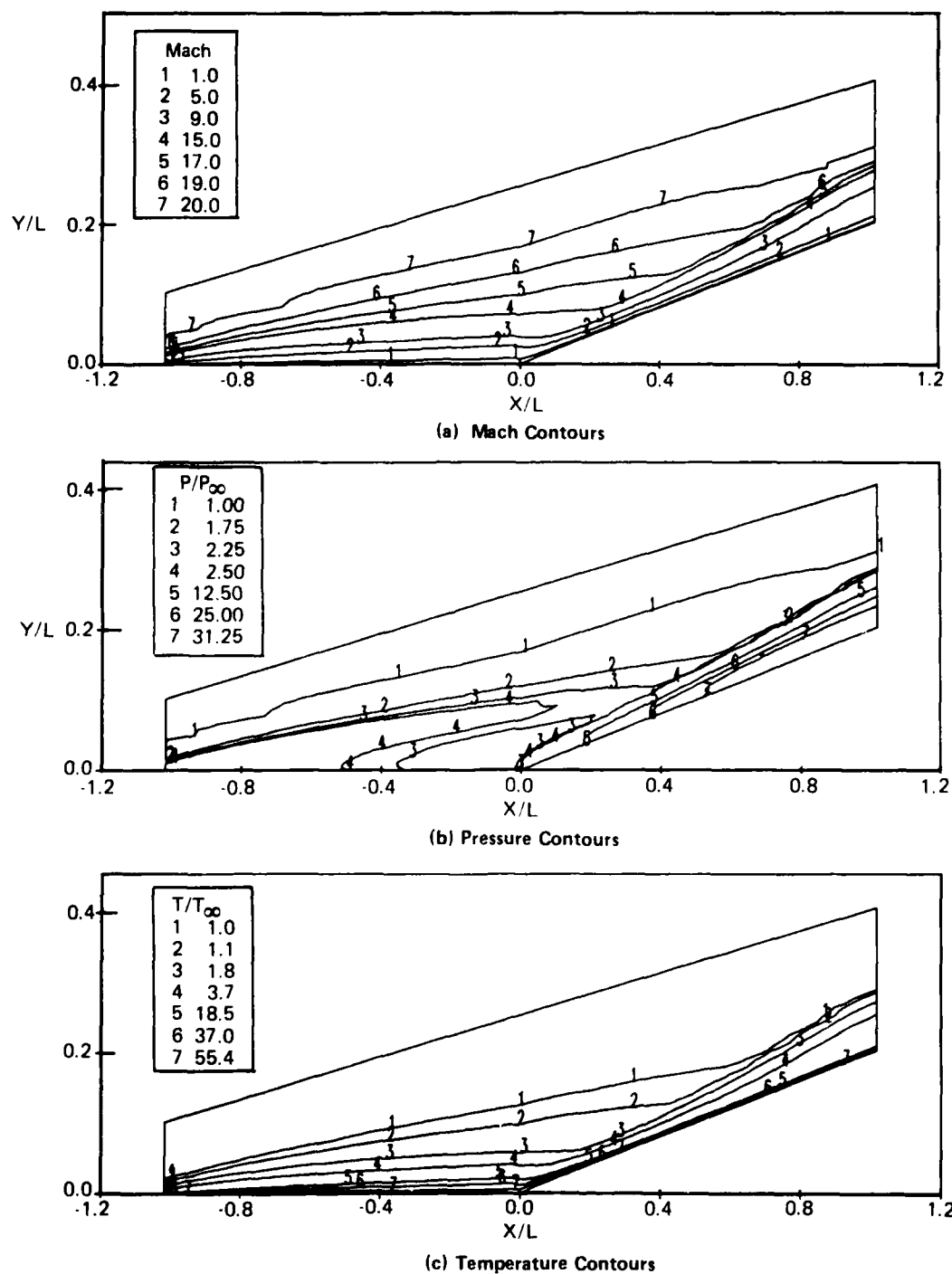
Figure 2. Calculated Results for Three-Dimensional Compression Corner Test Case

physical features of the flowfield, including the leading edge shock which impinges the shock from the compression corner. The shock angle of $15°$ compares well with that for an 11.3 degree half-angle wedge given by Ref. 15.

Test Case 2: 3D Blunt Nose. The second test case was extracted from a geometry created for the 1987 Parabolized Navier-Stokes (PNS) workshop, held 23-24 September 1987 at Wright Patterson AFB. The geometry used here considered only the nose region of the PNS workshop model, including the 1 inch (0.0254m) diameter blunt nose and a 3 nose radii long section of the 5 degree ramp attached to the nose. Again, the intent here was to study gross physical characteristics of an isolated strong (normal) shock to determine the ability of the prototype algorithm to calculate strong shocks at high Mach numbers. The test conditions were the same as for the PNS workshop, with the exception that the solid wall was assumed to be adiabatic for this case. The test conditions are summarized below:

Mach number:	20	
Freestream velocity:	6596 m/s	(21633 ft/s)
Static pressure:	$79.779 N/m^2$	$(1.67 lb_f/ft^2)$
Static temperature:	270.65K	$(488°R)$

The Reynolds number (based on nose radius) was 10^4.

A 35x30 mesh, shown in Figure 3, was used in the 2D plane. Three cells covering 15 degrees were used in the circumferential direction. The outer boundary was located 0.25 nose radii upstream from the nose tip, and the shock was captured by the calculation. A converged solution was obtained in approximately 100 implicit steps, and the results are shown in Figure 4. Part a of Figure 4 shows the Mach contours for the flowfield, and clearly shows a well-defined normal shock near the nose. The shock standoff distance was approximately 0.20 times the nose radius, consistent with that

Figure 3. 35 x 30 Grid in Two-Dimensional Plane for Three-Dimensional Blunt Nose Normal Shock Test Case
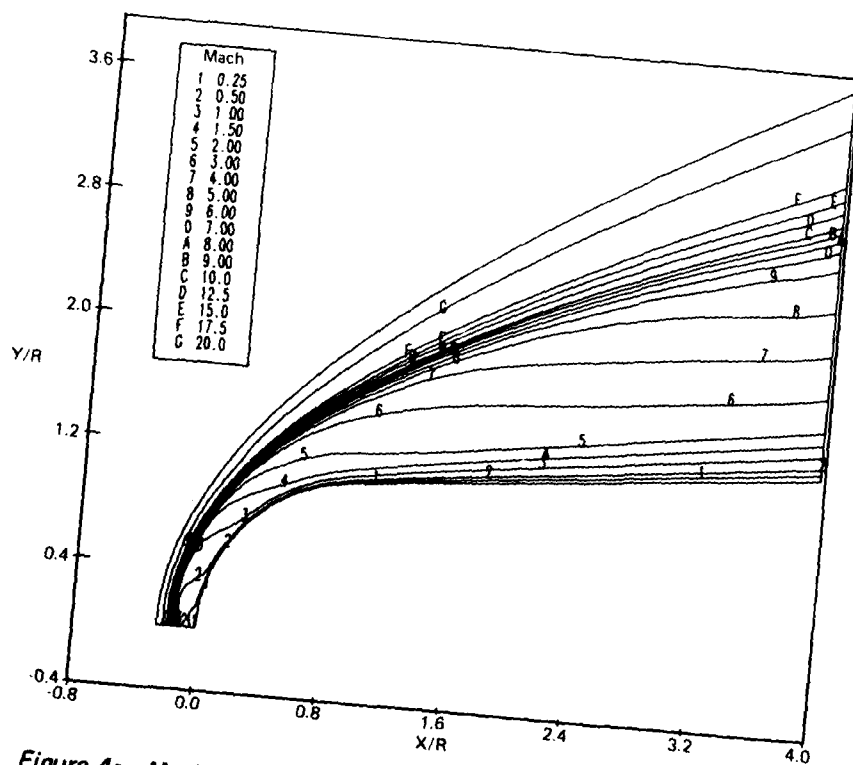
Figure 4a. Mach Contours for Three-Dimensional Blunt Nose Test Case
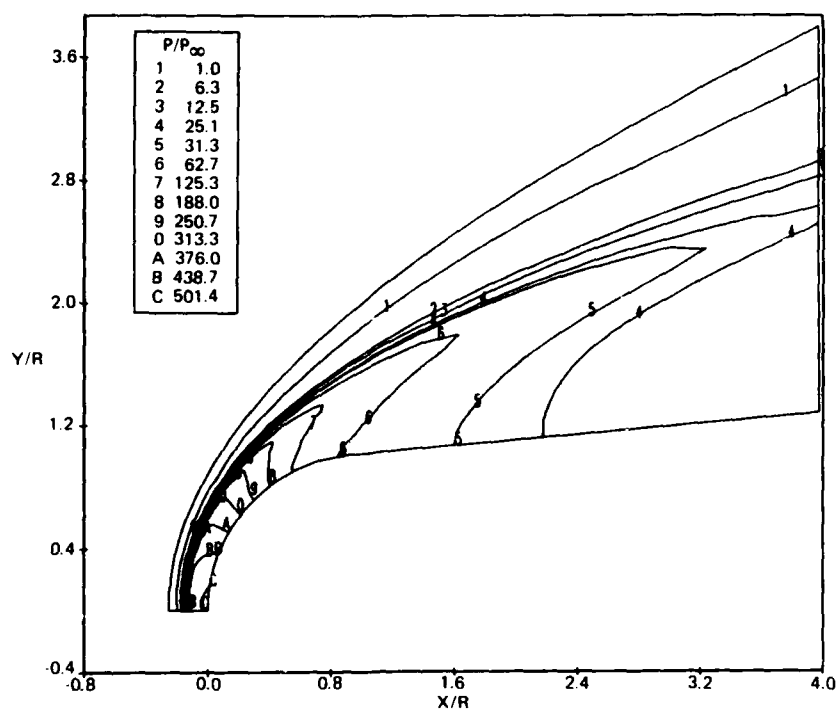
Figure 4b. Pressure Contours for Three-Dimensional Blunt Nose Test Case
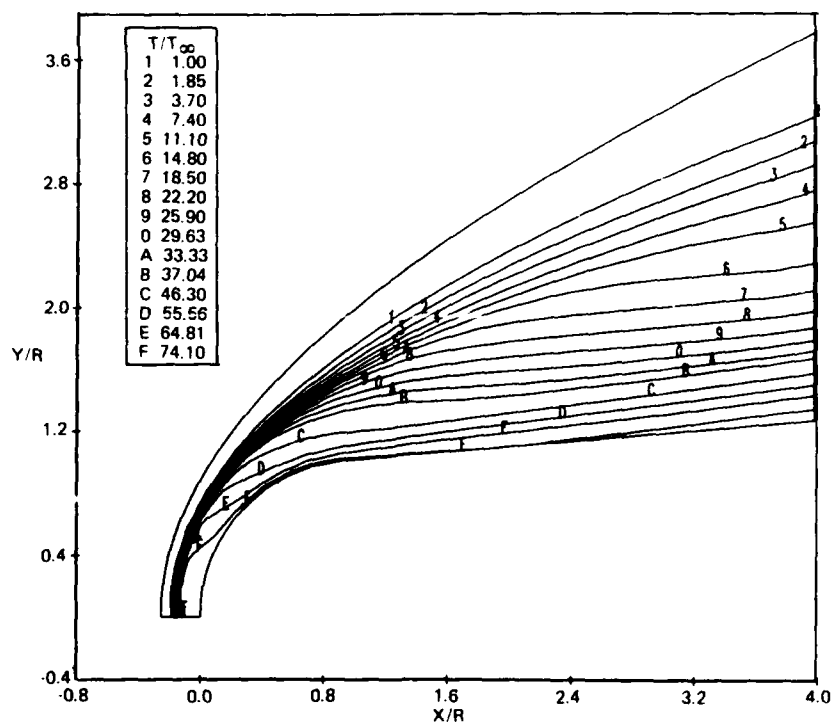
Figure 4c. Temperature Contours for Three-Dimensional Blunt Nose Test Case
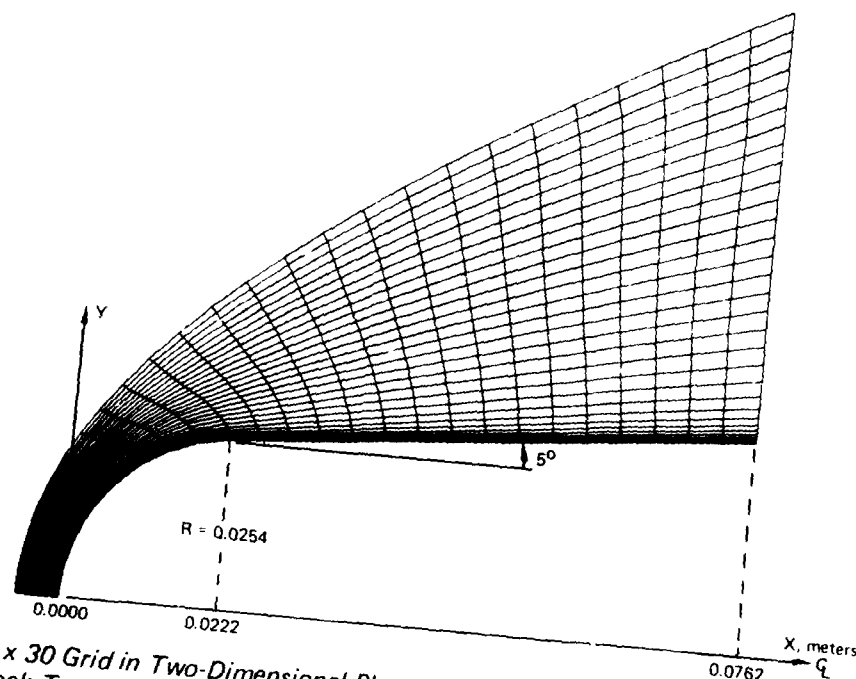
25

given by Liepmann and Roshko (Ref. 16). Parts (b) and (c) of Figure 4 show pressure and temperature contours, respectively.

2.3 NONEQUILIBRIUM CHEMISTRY ALGORITHM

2.3.1 Background

Hypersonic vehicles at high altitude encounter an environment characterized by low density effects and reacting gas chemistry. Therefore, it is required that a reacting gas chemistry equation set be solved. There are four basic methods for including the chemistry equations with the fluid dynamic (NS) equations: (1) uncoupled explicit, (2) uncoupled implicit, (3) coupled point-implicit, (4) coupled fully-implicit. Of these four choices (1) is the simplest to implement but represents the least amount of flow physics, while (4) is the most difficult to implement, and best describes the flow physics associated with the reacting gas flowfield. For relatively benign environments, the lagged methods (1), (2) are probably sufficient; however, for the hostile environments to be encountered by high altitude hypersonic vehicles, it is believed that it will be necessary to couple the chemistry equation set to the fluid dynamic equation set.

Fully-implicit coupling of the NS/chemistry equations has been chosen for development under this contract since, at this time, it appears to represent the best prospect for alleviating the stiffness problem. A system of equations is described as stiff if some components of the solution respond very quickly to system perturbations (i.e., have short time scales) while others respond slowly (i.e., have long time scales). The differences in response times can be due to differences in response times between the various equation sets describing the flow, such as the fluid dynamic and chemistry equations, or it can be due to large differences in the time scales characterizing different regions of the flowfield. Explicit solution techniques generally have stability restrictions that relate the maximum allowable time step to the fastest characteristic time scale, and therefore often require large numbers of computational steps, with

correspondingly large computational costs. Implicit solution techniques do not exhibit these stability restrictions and can therefore use much larger time steps.

One disadvantage of using a fully-coupled implicit approach is associated with the size of the block matrix to be solved. For a large number of chemical equations, the additional cost to solve the block matrix may be prohibitive. For the equation set to be used here, it is not felt that the additional computational time will be excessive. Development of the coupled equation set is described in Section III.

For the test cases to be considered in the present contract, nine species have been identified as critical for accurate flowfield calculation, including electron density. The fully-coupled 3D NS/chemistry equation set represents a block 14×14 matrix (original 5×5 for NS plus 9×9 for chemistry). Since the equation set is fully-coupled, it is desired that the solution technique for the coupled set be the same as for the fluid dynamic equations. Thus, the MacCormack algorithm (Ref. 2), extended to include an arbitrary number of chemical equations, has been selected as the algorithm for solving the coupled NS/chemistry equation set.

It should be noted here that not all nine species will have significant effects in all areas of the flowfield. Therefore, an equation-adaptive capability is being investigated which would allow a reduced equation set to be solved in flowfield regions where some species may not significantly affect the solution. In such cases, the flexibility of the MacCormack coupled NS-chemistry algorithm could be exploited by reducing the size of the block matrix to be solved, thereby resulting in a savings in computer time. Inclusion of this feature will be contingent upon determination of the generality of such a feature, as well as the determination of whether the code can automatically adjust the equation set, or if the user will be required to specify the range of validity for each chemical species. It is felt at present that the equation set should not be arbitrarily user-specified, and that the full equation set should be retained unless some well-defined general rules, such as concentration limits for each species, can be defined for automatically adjusting the equation set.

2.3.2 Features of the Solution Algorithm

There are a number of features associated with extending the MacCormack algorithm to include chemistry. Implementation of the fully-coupled chemistry algorithm is straightforward since it follows the same procedure used for developing the MacCormack implicit algorithm for the NS equations. Additionally, the fully-coupled chemistry along each Gauss-Seidel solution line provides the most accurate description of the flow physics by solving the fluid dynamic and chemistry effects simultaneously. As noted earlier, a third advantage (not unique to this approach) is that the implicit treatment of the chemistry source terms removes the chemistry stiffness problem, and permits larger time steps more consistent with an implicit solution algorithm to be taken. The MacCormack algorithm extension to include chemistry is general, implying that an arbitrary number of species chemistry equations may be added, with the only limitation being computational (i.e. solving the larger matrix) rather than physical (i.e. any number of species may be modeled). Finally, MacCormack and Candler (Ref. 2) have demonstrated the chemistry algorithm for a two-dimensional blunt nose at hypersonic velocity. Recently, Shinn, Yee, and Uenishi demonstrated this algorithm in 3D (Ref. 10) using a TVD approach. The MacCormack-Candler test case will be described in Section 2.3.4.

2.3.3 Chemistry Algorithm Development

The chemistry algorithm will be discussed here in terms of the coupled fluid dynamics/chemistry algorithm for completeness. The MacCormack algorithm for the NS equations with coupled nonequilibrium chemistry solves the following equation set (in strong conservation form):

$$\frac{\partial U_c'}{\partial t} + \frac{\partial F_c'}{\partial x} + \frac{\partial G_c'}{\partial y} + \frac{\partial H_c'}{\partial z} = \dot{W}, \tag{12}$$

where primes again denote nontransformed (cartesian) quantities, and subscript c distinguishes the coupled fluid dynamic/chemistry vectors in Equation (12) from the

28

fluid dynamic vectors in Equation (1). Here, $U'_c = [\rho_1, \ldots, \rho_{N_S}, \rho u, \rho v, \rho w, e]^T$ denotes the (conservative) solution vector, with $\rho_1, \ldots, \rho_{N_S}$ representing the species densities for species 1 through N_S (N_S = number of species), $\rho = \sum_{s=1}^{N_S} \rho_s$ represents the total density, u, v, w represent the Cartesian velocity components, and e represents the energy per unit volume. The chemistry source term ($\dot{W}$) is written in the transposed form $\dot{W} = [\dot{\omega}_1, \ldots, \dot{\omega}_{N_S}, 0, 0, 0, 0]^T$, where $\dot{\omega}_1 \to \dot{\omega}_{N_S}$ represent the source terms for each species. The determination of these source terms is deferred until Section III.

The coupled fluid dynamics/chemistry flux vectors (F'_c, G'_c, H'_c) are again split into inviscid and viscous parts, and are written in cartesian coordinates as follows:

$$
F'_c = \begin{bmatrix} \rho_1 u \\ \cdot \\ \cdot \\ \cdot \\ \cdot \\ \rho_{N_S} u \\ \rho u^2 + p \\ \rho uv \\ \rho uw \\ u(e+p) \end{bmatrix} + \begin{bmatrix} \rho_1 \hat{u}_1 \\ \cdot \\ \cdot \\ \cdot \\ \rho_{N_S} \hat{u}_{N_S} \\ -\mu_B \left[\frac{\partial u}{\partial x} + \frac{\partial v}{\partial y} + \frac{\partial w}{\partial z} \right] - 2\mu \frac{\partial u}{\partial x} \\ \tau_{xy} \\ \tau_{xz} \\ u \left[-\mu_B \left[\frac{\partial u}{\partial x} + \frac{\partial v}{\partial y} + \frac{\partial w}{\partial z} \right] - 2\mu \frac{\partial u}{\partial x} \right] + v\tau_{xy} + w\tau_{xz} - \lambda \frac{\partial T}{\partial x} + \sum_{s=1}^{N_S} \rho_s h_s \hat{u}_s \end{bmatrix} ,
\tag{12a}
$$

$$
G'_c = \begin{bmatrix} \rho_1 v \\ \cdot \\ \cdot \\ \cdot \\ \rho_{N_S} v \\ \rho vu \\ \rho v^2 + p \\ \rho vw \\ v(e+p) \end{bmatrix} + \begin{bmatrix} \rho_1 \hat{v}_1 \\ \cdot \\ \cdot \\ \cdot \\ \rho_{N_S} \hat{v}_{N_S} \\ \tau_{yx} \\ -\mu_B \left[\frac{\partial u}{\partial x} + \frac{\partial v}{\partial y} + \frac{\partial w}{\partial z} \right] - 2\mu \frac{\partial v}{\partial y} \\ \tau_{yz} \\ u\tau_{yx} + v \left[-\mu_B \left[\frac{\partial u}{\partial x} + \frac{\partial v}{\partial y} + \frac{\partial w}{\partial z} \right] - 2\mu \frac{\partial v}{\partial y} \right] + w\tau_{yz} - \lambda \frac{\partial T}{\partial y} + \sum_{s=1}^{N_S} \rho_s h_s \hat{v}_s \end{bmatrix} ,
\tag{12b}
$$

$$H'_c = \begin{bmatrix} \rho_1 w \\ \cdot \\ \cdot \\ \cdot \\ \rho_{N_s} w \\ \rho wu \\ \rho wv \\ \rho w^2 + p \\ w(c+p) \end{bmatrix} + \begin{bmatrix} \rho_1 \hat{w}_1 \\ \cdot \\ \cdot \\ \cdot \\ \rho_{N_s} \hat{w}_{N_s} \\ \tau_{zx} \\ \tau_{zy} \\ -\mu_B\left[\dfrac{\partial u}{\partial x}+\dfrac{\partial v}{\partial y}+\dfrac{\partial w}{\partial z}\right]-2\mu\dfrac{\partial w}{\partial z} \\ u\tau_{zx}+v\tau_{zy}+w\left[-\mu_B\left(\dfrac{\partial u}{\partial x}+\dfrac{\partial v}{\partial y}+\dfrac{\partial w}{\partial z}\right)-2\mu\dfrac{\partial w}{\partial z}\right]-\lambda\dfrac{\partial T}{\partial z}+\sum_{s=1}^{N_s}\rho_s h_s \hat{w}_s \end{bmatrix} ,$$

(12c)

where inviscid terms are contained in the left-hand vectors, viscous terms are contained in the right-hand vectors, and

$$\tau_{xy} = \tau_{yx} = -\mu\left(\frac{\partial u}{\partial y} + \frac{\partial v}{\partial x}\right),$$

$$\tau_{xz} = \tau_{zx} = -\mu\left(\frac{\partial u}{\partial z} + \frac{\partial w}{\partial x}\right),$$

(12d)

$$\tau_{yz} = \tau_{zy} = -\mu\left(\frac{\partial v}{\partial z} + \frac{\partial w}{\partial y}\right),$$

with p = pressure, T = temperature, λ = coefficient of thermal conductivity, μ = dynamic viscosity, $\mu_B = -\frac{2}{3}\mu$ = bulk viscosity, h_s = specific enthalpy of species s, and $\hat{u}_1 \to \hat{u}_{N_S}$, $\hat{v}_1 \to \hat{v}_{N_S}$, $\hat{w}_1 \to \hat{w}_{N_S}$ represent the Cartesian diffusion velocities for species 1 through N_S. From Candler and MacCormack (Ref. 2), it is noted that the diffusion velocities are proportional to the gradients of the species concentrations, assuming that pressure, thermal, and body force effects on the diffusion velocities are negligible. Thus, the diffusion velocities may be written in the form:

$$\rho_s \hat{u}_s = -\rho D_s \frac{\partial C_s}{\partial x},$$

30

$$\rho_s \, \hat{v}_s = -\rho D_s \, \frac{\partial C_s}{\partial y} \, , \qquad\qquad (12e)$$

$$\rho_s \, \hat{w}_s = -\rho D_s \, \frac{\partial C_s}{\partial z} \, ,$$

where D_s is the specie concentration diffusion coefficient, and C_s is the specie concentration. The translational, vibrational, and rotational energy modes have been omitted in the coupled governing equations described above. These three energy modes are assumed to be in equilibrium, for reasons to be discussed in Section III.

Note that a species continuity equation is written for each species, with no global species continuity equation, as opposed to the alternative form of writing N_S-1 species continuity equations plus a global continuity equation. Yee and Shinn (Ref. 11) have noted that the present form is equivalent to the form utilizing the global species continuity equation, but has the advantage that the eigenvectors of this system are easier to determine.

Comparing Equations (1) and (12), it can be seen that the chemistry equations modify both the inviscid and viscous flux vectors. The global continuity equation in the inviscid matrices of Equation (1) is replaced with specie continuity equations for each of the N_S species. In the viscous matrices, the continuity contribution (which was originally zero) is replaced by the diffusion velocity contributions from each of the N_S species. The diffusion velocities also contribute to the energy term in the viscous matrices. Since the original form of the flux vectors is not changed, the Gauss-Seidel relaxation solution procedure developed for the NS equations will also apply to the coupled equation set in Equation (12).

Solution Procedure. The mathematical treatment of the coupled fluid dynamics/chemistry equation set is similar to that described in Section 2.2, and will only be summarized here. The cartesian form of Equation (12) is transformed to generalized curvilinear coordinates (ξ, η, ζ), and the implicit governing equation is formulated from the transformed equation set. Once again, the inviscid flux vectors are split into positive and negative contributions (based on eigenvalue sign), so that forward finite

differences can be applied to negative contributions and backward finite differences can be applied to positive contributions. The implicit governing equation for the 3D flux-split fully-coupled NS/chemistry equation set becomes:

$$\left\{ I + \Delta t \left[D_{-\xi} A_c^+ + D_{+\xi} A_c^- + D_{-\eta} B_c^+ + D_{+\eta} B_c^- + D_{-\zeta} C_c^+ + D_{+\zeta} C_c^- - \frac{\partial \dot{W}}{\partial U} \right] \right\} \delta U_c^{n+1}$$

$$+ \Delta t \left\{ D_{-\xi} \left(F_{c_\xi} D_{+\xi} \right) N_c + D_{-\eta} \left(G_{c_\eta} D_{+\eta} \right) N_c + D_{-\zeta} \left(H_{c_\zeta} D_{+\zeta} \right) N_c \right\} \delta U_c^{n+1} = \Delta U_c^n , \quad (13)$$

where Δt is the time step, I is the identity matrix, D_- indicates backward differences, D_+ indicates forward differences, and N_c denotes the matrix relating the nonconserved solution vector to the conserved solution vector. Note that, as was the case in the fluid dynamic algorithm, only diagonal components of the viscous stresses are retained in the implicit formulation, while full viscous terms are retained in the explicit change (ΔU_c^n), and subscript c denotes vectors associated with coupled NS/chemistry equations. Equation (13) is solved by the same procedure described in Section 2.2.5, the only difference being the size of the block tridiagonal to be solved. The solution of Equation (13) will provide accurate flowfield calculations for low density real gas flows about hypersonic vehicles.

2.3.4 Test Case

The coupled NS/chemistry algorithm has been used by MacCormack and Candler (Ref. 2) to calculate the nonequilibrium chemistry flow about a two-dimensional sphere-cone at Mach 18. Test conditions for the calculation were as follows:

Mach number:	17.94	
Freestream Velocity:	5940 m/s	(19488 ft/s)
Static Pressure:	79.779 N/m^2	(1.67 lbf/ft^2)
Static Temperature:	270.65K	(487°R)

The nose radius of the blunt body was 0.2 meters (7.9 inches) and the cone section had a half-angle of 10 degrees. The Reynolds number based on nose radius was 7.16 (10^4). An isothermal wall temperature of 1500K (2700°R) was assumed, and five gas species (N_2, O_2, NO, N, O) and three vibrational energies were included. Shock-fitting was used to fit the strong bow shock. The results presented in Figures 5 through 8 were obtained in approximately 150 implicit steps using a 30×30 grid. As was the case for the NS algorithm test cases described in Section 2.2.6, the intent here was to assess the ability of the chemistry algorithm to calculate gross flow features of hypersonic flows. No attempt was made to validate the algorithm to confirm the accuracy of the fine flow details. The figures presented here are intended only to demonstrate global calculation capability.

Figure 5 shows mass concentrations on the stagnation streamline for the four minor species (O_2, NO, N, and O) versus axial distance along the missile, while Figures 6 (a-e) present 2D contours of mass concentration for each of the five gas species. Temperature ratios on the stagnation streamline versus axial distance along the model are shown in Figure 7 for the translational-rotational temperature (T) and the three vibrational temperatures for N_2, NO, and O. Figure 8a presents 2D contours of the translational-rotational temperature, while Figure 8b presents 2D contours for the vibrational temperature of N_2.

Figure 5. Mass Concentration on Stagnation Streamline
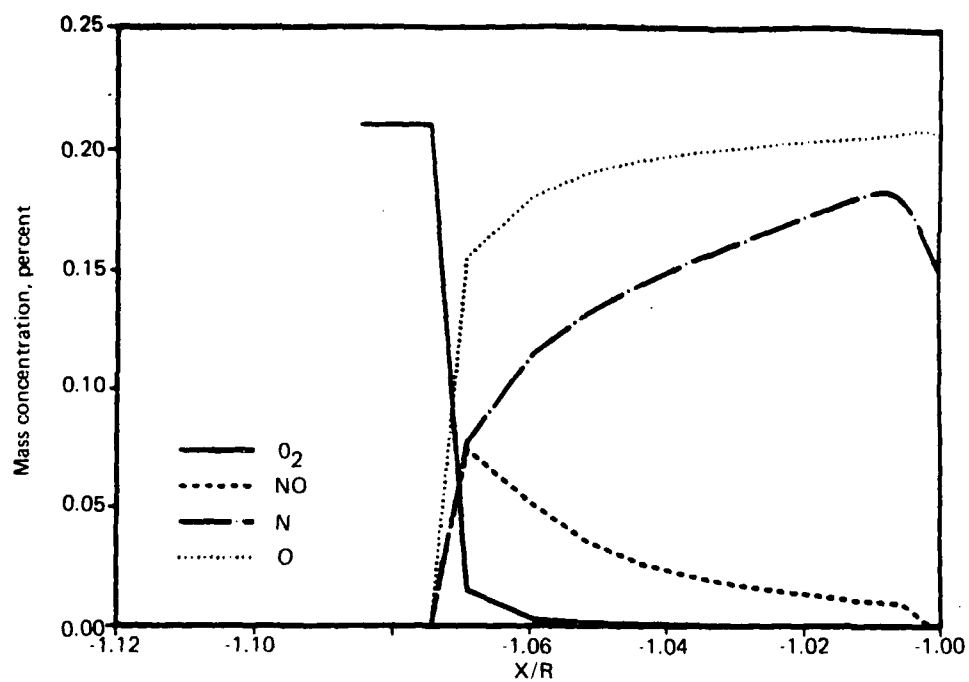

Figure 6a. Contours of Mass Concentration of N_2 (Percent)

34

Figure 6b. Contours of Mass Concentration of O_2 (Percent)

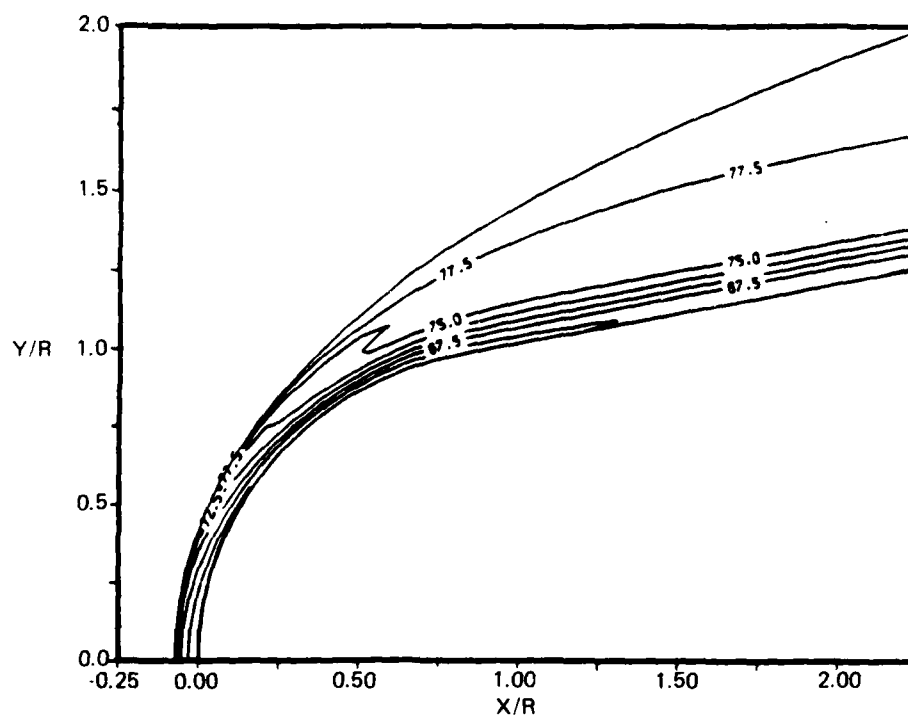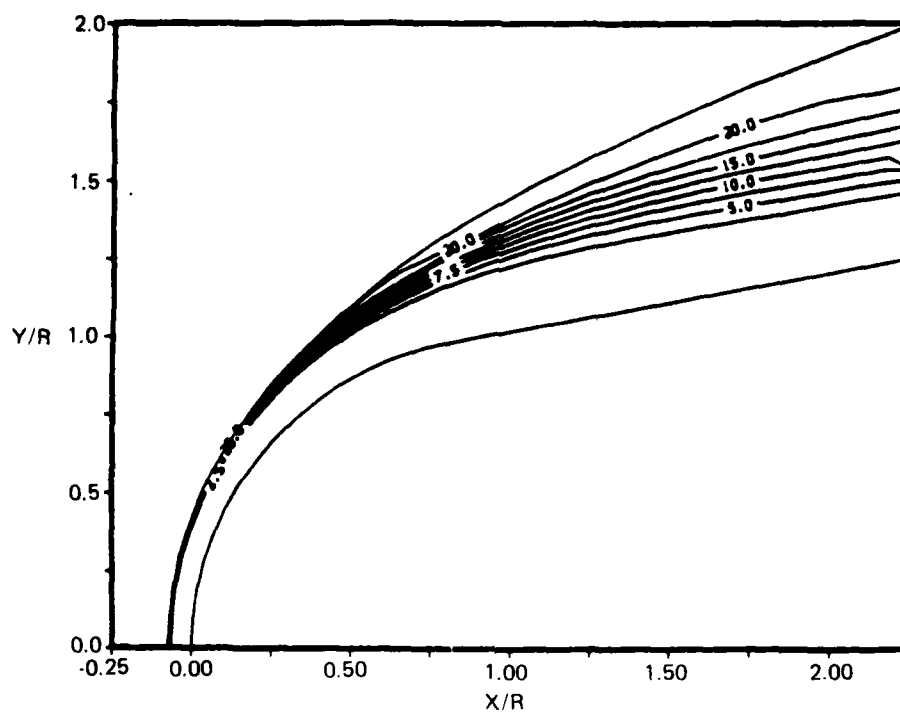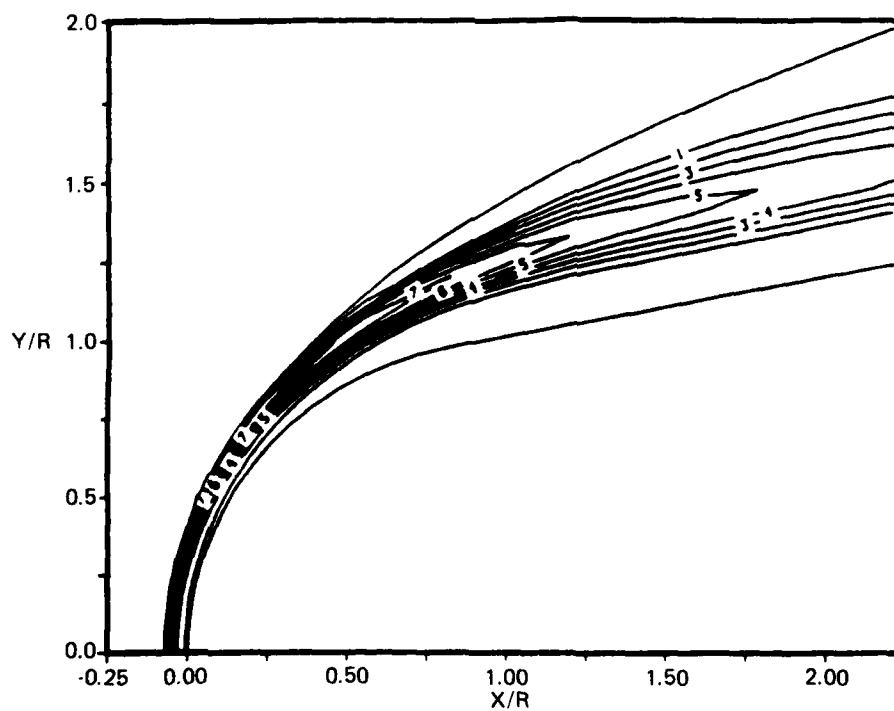*Figure 6c. Contours of Mass Concentration of NO (Percent)*
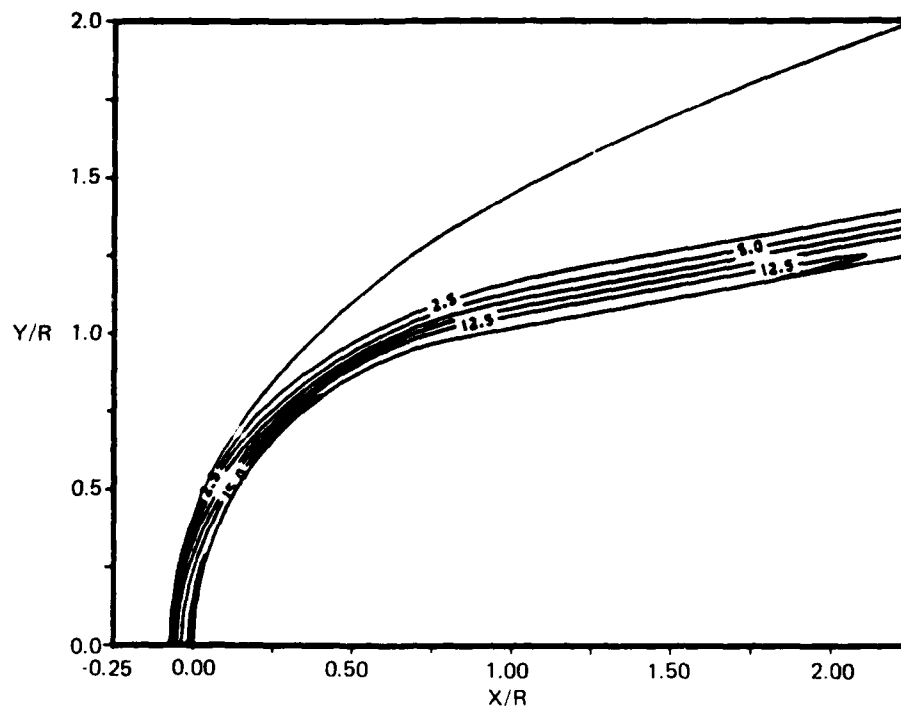
35

Figure 6d. Contours of Mass Concentration of N (Percent)
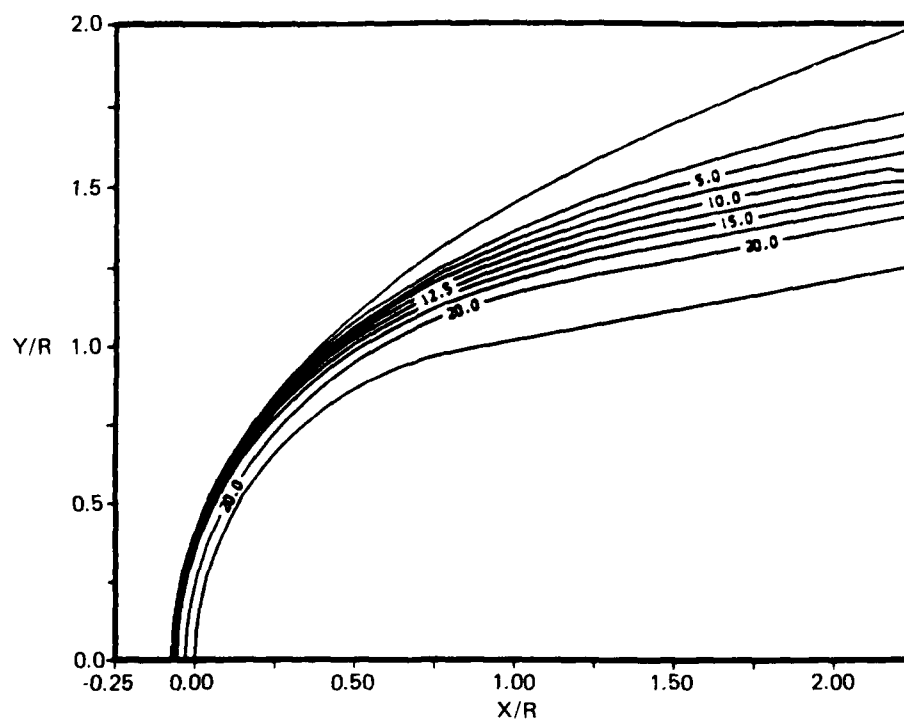

Figure 6e. Contours of Mass Concentration of O (Percent)
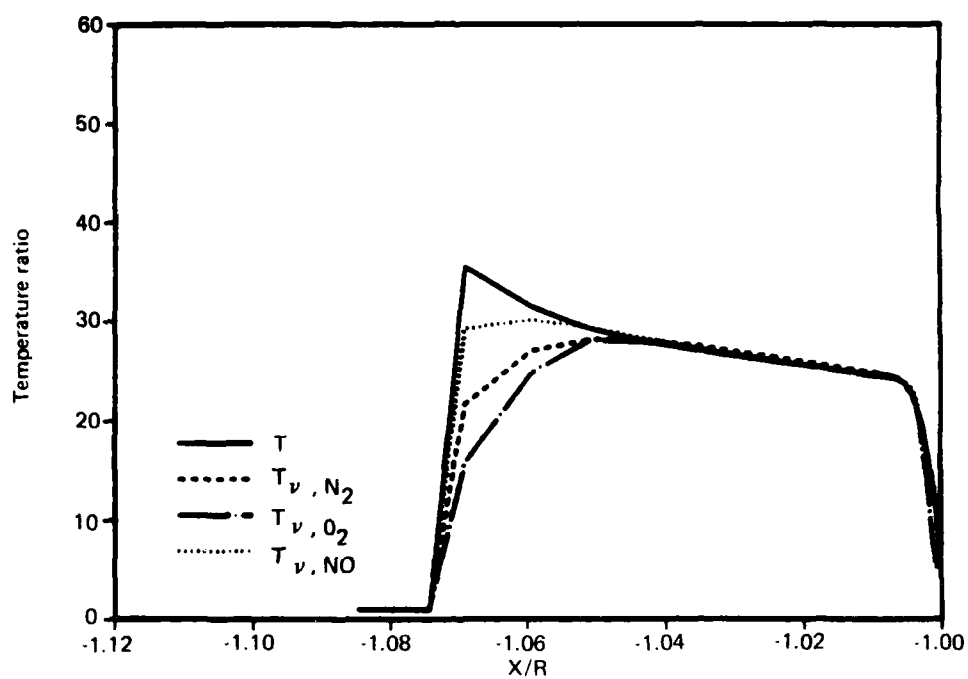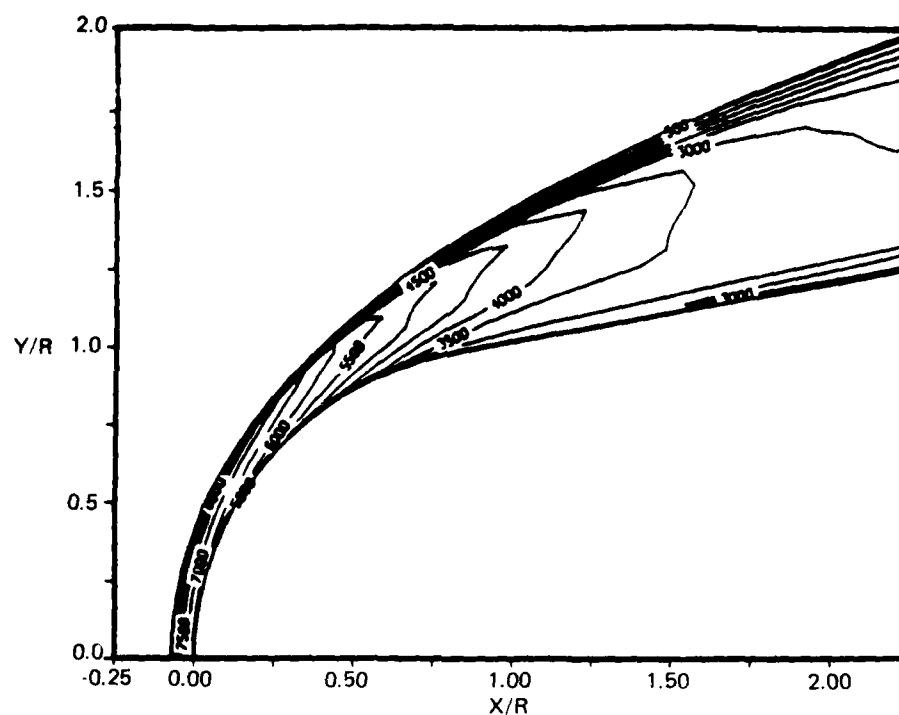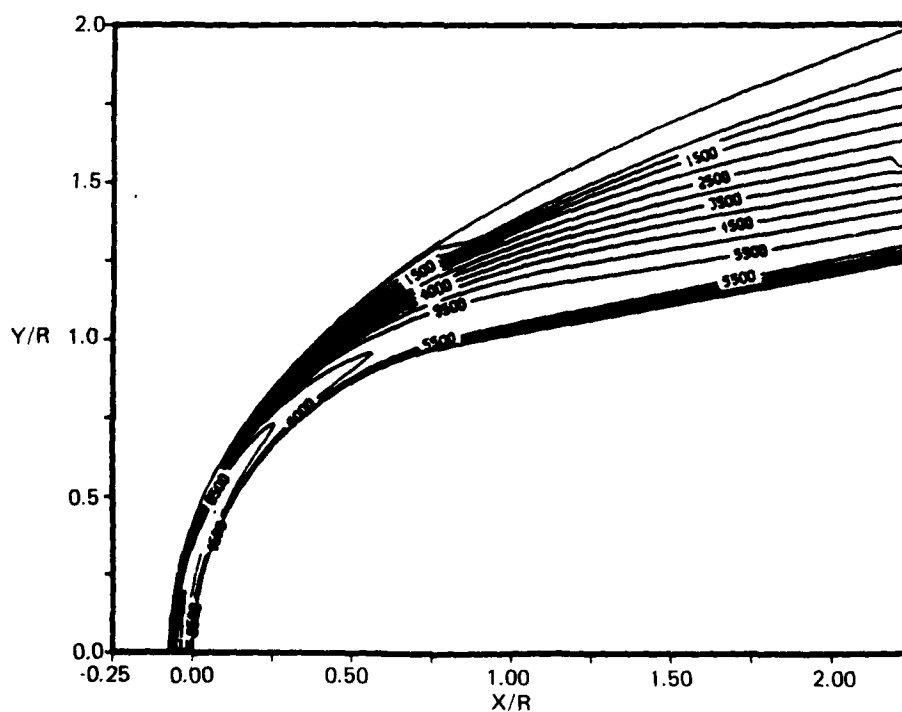
Figure 7. Temperature Ratios on Stagnation Streamline

(a) Translational-Rotational Temperature Contours (Kelvin)

(b) Vibrational Temperature of N_2 Contours (Kelvin)

Figure 8. Two-Dimensional Temperature Contours

2.4 VECTORIZATION AND PARALLEL PROCESSING

2.4.1 Background

The goal of this contract is to accurately and efficiently (i.e., one hour or less) calculate low density reacting gas flows about hypersonic vehicles 150-200 nose radii in length. Sections 2.2 and 2.3 have described in detail the algorithms which will be used to solve the coupled 3D Navier-Stokes/chemistry equation set. Adequate flowfield resolution in boundary layers, near shocks, and in the leeside separation regions will require a large number of grid points to discretize the flowfield. The resulting computational effort will probably not be capable of meeting the stated time goal on a single processor machine. Therefore, it is required that parallel processing and vectorization of the solution algorithms be accomplished. The Phase I effort in this area consisted of assessing the parallel processing and vectorization potential for the Navier-Stokes and chemistry solution algorithms. A two-fold approach was chosen: (1) assessment of current state-of-the-art in vectorization and parallel processing hardware and software, and (2) demonstration of parallel processing and vectorization on a prototype Navier-Stokes solution algorithm. These topics will be discussed separately.

2.4.2 Assessing the State-of-the-Art

Recent developments in the supercomputing environment (in the past 10 years), have rapidly advanced the state-of-the-art. Projections for the next five years, with respect to computing speed and storage, are perhaps even more ambitious. Within the past two years, a number of mini-supercomputers have been developed, in addition to continued development of recognized supercomputers such as the Cray series of computers.

The supercomputer environment can be described by two factors: (1) computer hardware (architecture, processors, storage), and (2) software systems. These two factors are not mutually exclusive, as the software systems are generally highly dependent upon the computer system architecture. However, the discussion here will be

39

restricted to software for vectorization and parallel processing only, and the two topics will be described independently.

Hardware. By far the most well-known supercomputers in use today are the Cray series of computers. The Cray machines represent a number of different computer architectures, ranging from the silicon technology of the Cray-1 to the gallium arsenide technology projected for the Cray-3 (due out in 1992). Each architecture strives to minimize clock time while maximizing computing efficiency. As such, there are trade-offs to be made; for instance, chaining was omitted in the Cray-2 due to physical dimensional limitations of the capacitors to be used for chaining. Another problem facing both the Cray-XMP and Cray-2 is memory contention between multiple CPUs. Both of these problems can be alleviated by means of local memory which reduces the number of fetches and stores to main memory. With memory contention reduced, Cray plans to implement up to 64 processors on the Cray-3.

The success achieved by the Cray series of computers has led to the creation of a number of computer companies whose goal is to develop mini-supercomputers. These mini-supercomputers seek to provide computational power approaching that of the Cray computers at a proportionately lower cost. Many of these machines are intended to be dedicated single user or multiple (2 or 3) user systems, with the hope that the throughput from the mini-supercomputers will be cost-effective when compared to the more powerful (but frequently overloaded) Cray machines. Therefore, a realistic assessment of the state-of-the-art in computer hardware should include a study of the mini-supercomputers available today.

The mini-supercomputer companies have shown much interest in the prototype Navier-Stokes code upon which this contract effort is being based. To date, the prototype code has served as a benchmark for the FPS, ALLIANT, and INTEL mini-supercomputers, as well as for the SCS-40 and CONVEX mini-supercomputers. The latter two computers are currently being evaluated in-house by the Boeing Aerospace Company at the Kent Space Center. Results of these benchmark tests are proprietary.

The architectures of the FPS, SCS-40, and CONVEX computers are similar, in that

they are all single processor machines. The ALLIANT has eight processors and the Intel computer has a multiprocessor hypercube architecture which required substantial source code modifications before the benchmark could be calculated. All of the mini-supercomputers permitted some degree of vectorization. However, it is still felt that, for the purposes of the current contract, the target machine for Phase II of the study should be a Cray series computer. The Cray system computers are more powerful than the mini-supercomputers, and have a more established software system for vectorization and parallel processing than the relatively new mini-supercomputers available today.

Software. The software systems on the aforementioned mini-supercomputers are currently in various stages of development, with many of the systems (directly or indirectly) trying to mimic the software systems from Cray Research. Therefore, the discussion here will focus on recent developments in Cray Research software.

Vectorization still represents the most basic method for improving code performance, and is executed on a single processor. *Vectorization consists of arranging* nested DO loops such that the longest vector occupies the innermost loop. The only requirement for vectorization is that all DO loop index dependencies be removed on this inner (vector) loop. Vectorization alone can result in significant reduction in computer run times.

Additional increases in computer code efficiency can be realized by multi-processing a vectorized code. Cray Research currently utilizes two techniques to accomplish parallel processing-namely, macrotasking and microtasking. Macrotasking, which consists of adding compiler directives around large blocks of coding that may be executed simultaneously on multiple processors, has existed for some time and is well-documented. Microtasking is a more recent software development, and consists of adding compiler directives around small blocks of coding which may be executed simultaneously on multiple processors.

Microtasking is basically a more refined version of macrotasking. The selection of microtasked blocks is more complicated than the selection of macrotasked blocks;
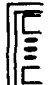
41

however, Cray will be introducing a CFT77 compiler (release 2.0 for the X-MP and release 2.1 for the Cray-2) which will automatically microtask (Ref. 17). Additionally, Cray will be introducing a new compiler directive DO GLOBAL LONG VECTOR, which will identify long vector loops for special treatment.

2.4.3 Vectorization and Multiprocessing Demonstration

An explicit algorithm version of the prototype three-dimensional Navier-Stokes code under development in this contract was vectorized, and a test case was run on a Cray X-MP using a single processor. A flowtrace of the solution process showed that 85% of the CPU time was spent in the solution module, where all 86 DO loops vectorized.

The vectorized code was then multiprocessed by microtasking the explicit solution module. A schematic of the microtasking operation is shown in Figure 9, including compiler directives for the Cray X-MP COS 1.14 compiler. The microtasked version of the code was run successfully on the Cray X-MP/24 (2 processors) and Cray X-MP/48 (4

```
CMIC$  GETCPUS
CMIC$  MICRO
CMIC$  PROCESS

CMIC$  ENDPROCESS
CMIC$  DOGLOBAL
                }  28 inner vector loops

CMIC$  DOGLOBAL
                }  28 inner vector loops

CMIC$  DOGLOBAL
                }  28 inner vector loops

CMIC$  PROCESS

CMIC$  ENDPROCESS
CMIC$  RELCPUS
```

Figure 9. Multiprocessing the Explicit Algorithm on a Cray X-MP

processors). Additionally, the test case was run on 1, 2, 4, and 8 processors on the ALLIANT mini-supercomputer, as well as 16 processors on the Intel Hypercube.

Similar vectorization and multiple processing operations will be performed on the code under development in the current contract. It is expected that with vectorization and multiple processing, the contract objectives of calculating (in less than 1 hour) the reacting gas flowfield about bodies 150-200 nose radii long will be satisfied.

III. AIR CHEMISTRY REACTION MODEL AND WALL CATALYSIS

3.1 INTRODUCTION

The purpose of this section is to describe the work performed on the subtasks for developing an air chemistry reaction model and the selection of reaction rates and equilibrium constants. Figure 10 summarizes the procedure taken in this phase of the contract.
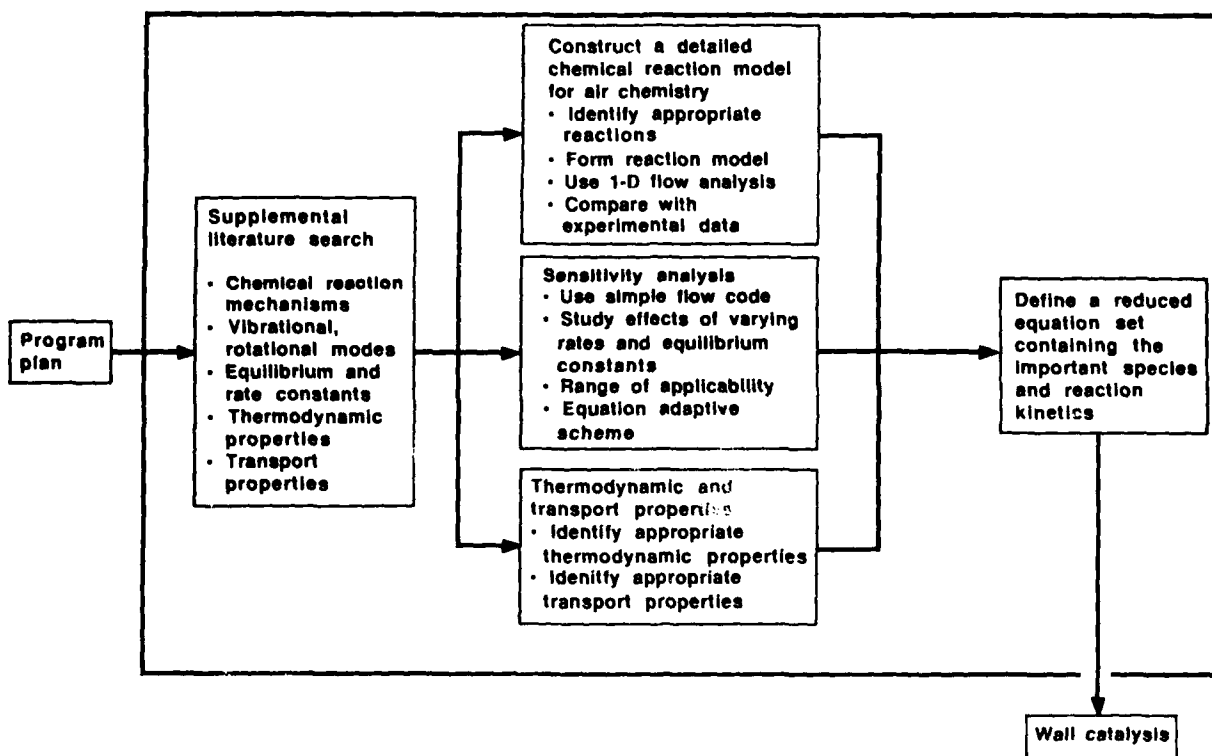
Figure 10. Subtasks for Developing a Chemistry Reaction Model and the Selection of Reaction Rates and Equilibrium Constants

The sequence of steps included a supplemental literature search, construction of a detailed air chemistry reaction model, a sensitivity analysis, and an examination of thermodynamic and transport properties methodology. By performing these tasks a reduced set of equations containing the important air species and reaction kinetics was assembled. Finally, the boundary conditions are discussed.

3.2 DESCRIPTION OF GENERALIZED EQUATIONS

The following section discusses the generalized equations that can be used to model hypersonic flows. For hypersonic flow, the temperatures produced around the vehicle can excite rotation, vibration, chemical ionization, electron excitation modes, and chemical disassociation. An example of chemical and thermal nonequilibrium regimes about the stagnation region of a blunt body is depicted in Figure 11.
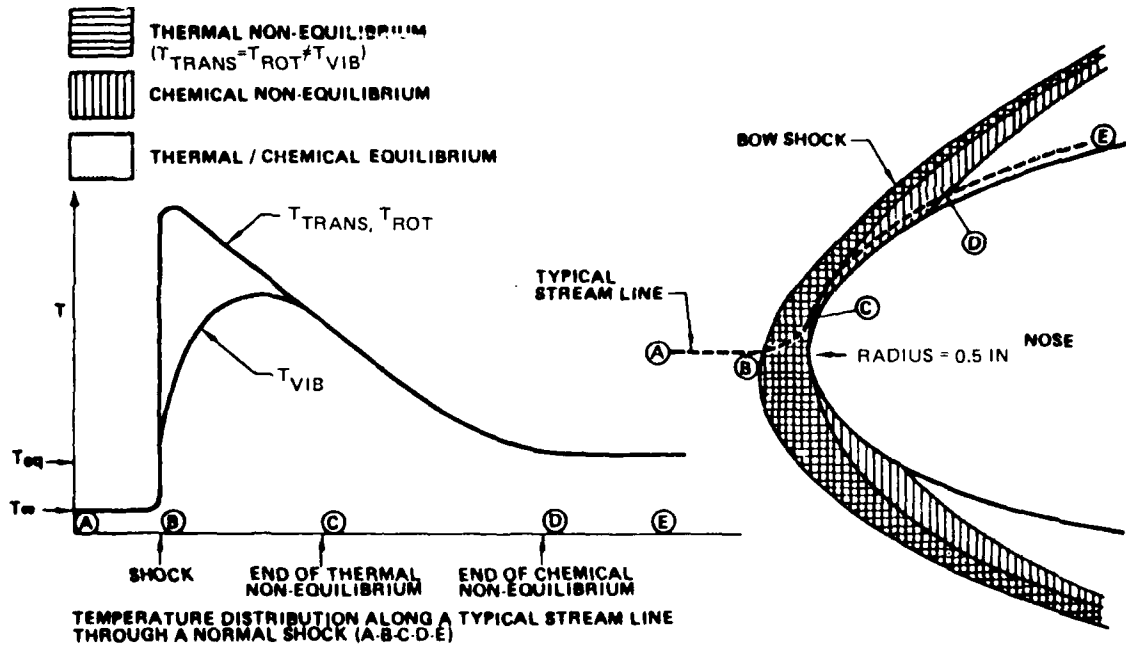
Figure 11. *Thermal and Chemical Nonequilibrium Regions About a Stagnation Point*

The governing equation for the coupled fluid dynamic/chemistry equation set can be written in strong conservation form:

$$\frac{\partial U_c'}{\partial t} + \frac{\partial F_c'}{\partial x} + \frac{\partial G_c'}{\partial y} + \frac{\partial H_c'}{\partial z} = \dot{W}, \tag{14}$$

where U_c' represents the conservative solution vector, F_c', G_c', H_c' represent the coupled fluid dynamic/chemistry flux vectors, and $\dot{W}$ represents the chemistry source terms. Primes denote cartesian (nontransformed) quantities.

A generalized transport equation can be constructed for each of the nonequilibrium

45

processes which comprise the chemical source term in Equation (14) (Ref. 18). For a given chemistry model a general reaction can be written as

$$\sum_{s=1}^{N_S} a_{rs} C_s \underset{k_{br}}{\overset{k_{fr}}{\rightleftharpoons}} \sum_{s=1}^{N_S} b_{rs} C_s, r = 1, \ldots, N_R \tag{15}$$
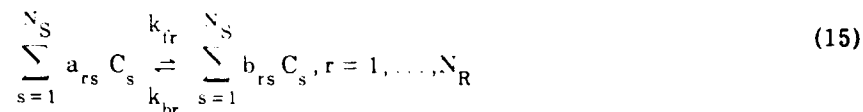
where a_{rs}, b_{rs} are the stoichiometric coefficients, C_s are the reactant and product species, N_S, N_R are the number of species and reaction paths, and k_{fr}, k_{br} are the forward and backward reaction rates, respectively.

The law of mass action states that the rate of change of concentration of species s by reaction r is given by

$$\left(\dot{C}_s\right)_r = \left(b_{rs} - a_{rs}\right) \left[k_{fr} \prod_{s=1}^{N_S} \left(C_s\right)^{a_{rs}} - k_{br} \prod_{s=1}^{N_S} \left(C_s\right)^{b_{rs}} \right] . \tag{16}$$

The rate change in concentration of species s by all N_R reactions is then found by summing the contributions from each reaction.

$$\dot{C}_S = \sum_{r=1}^{N_R} \left(\dot{C}_s\right)_r \tag{17}$$

Finally, the production rate of species s is found from

$$\dot{\omega}_s = \dot{C}_s m_s . \tag{18}$$

The forward reaction rates are computed from the Arrhenius Law:

$$k_{fr} = A_r(T)^{N_r} \exp\left(-E_r/T\right) , \tag{19}$$

for each reaction r. The coefficients, A_r, N_r and E_r are experimentally determined constants. The reverse rates can be found, given the forward rate and equilibrium constant K_{eq} for each reaction, as

$$k_{br} = k_{fr} / K_{eq} . \tag{20}$$

46

where K_{eq} is determined from the Gibbs free energy and is derived in Ref. 19.

Thus, it can be seen that the source term for species s is coupled to all of the reaction paths containing specie s. The reaction equations could represent O_2 disassociation as
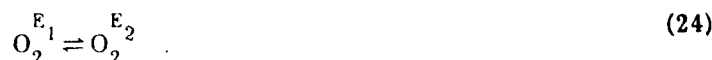
$$O_2 \rightleftharpoons O + O \quad , \tag{21}$$
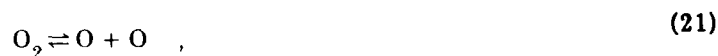
a reaction representing a diatomic molecule undergoing a transition from one vibrational state (V1) to another vibrational state (V2) as

$$O_2^{V_1} \rightleftharpoons O_2^{V_2} \quad , \tag{22}$$

an ionization reaction for NO as

$$NO \rightleftharpoons NO^+ + e^- \quad , \tag{23}$$

or an electronic excitation reaction for O_2 going from an E1 excited mode to an E2 excited mode

$$O_2^{E_1} \rightleftharpoons O_2^{E_2} \quad . \tag{24}$$

Reactions of these types can exist for other species. In fact, the number of possible reactions needed to model air chemistry is very large. A discussion of which reaction equations are important can be found in Section 3.3.

Finally, to close the equation set, an expression for the total internal energy is needed. The total internal energy can be written as

$$e_i = e_{trans} + e_{rot} + e_{vib} + e_{diss} + e_{elect} + e_{kin} \quad , \tag{25}$$

where e_{trans} represents the contribution due to translation; e_{rot}, the internal energy due to rotation; e_{vib}, the internal energy due to vibration; e_{diss}, the internal energy due to chemical disassociation/association; e_{elect}, the internal energy due to electronic states; and e_{kin} is the kinetic energy in the flow.

47

Each of these energy quantities is a function of the various specie concentrations and may not be in equilibrium. This represents the general partial differential equation set describing a chemical reaction system. Considerable reduction and simplification of the equations is possible. The mechanism for reducing the complexity of the problem is discussed in Section 3.3.

Typically, if all of the internal energy modes are in equilibrium, then the total internal energy can be represented by a polynomial in temperature. Reference 20 gives an example of how this is implemented.

Due to the potential importance of the electron distribution in the flow field, ionizational effects will be modeled. Ionization will be modeled by incorporating reaction mechanisms and transport equations for both ions and electrons.

One simplification, which has been used by several researchers including Vincenti (Ref. 21) and Wagener (Ref. 22) involves combining the various nonequilibrium vibration modes into a single equation for the nonequilibrium vibrational energy. The simplification results by assuming that a diatomic molecule behaves like a simple harmonic oscillator. With this assumption, a transport equation can be written for the nonequilibrium vibrational energy as

$$\frac{\partial(\rho e_{vib})}{\partial t} + \frac{\partial F'_c}{\partial x} + \frac{\partial G'_c}{\partial y} + \frac{\partial H'_c}{\partial z} = -\frac{\rho e^*_{vib} - \rho e_{vib}}{\tau} \quad , \tag{26}$$

where F'_c, G'_c, and H'_c are defined in Equation (14), e^*_{vib} is the equilibrium vibrational energy given by

$$e^*_{vib} = \frac{N v k_p}{e^{\theta_v/T} - 1} \quad , \tag{27}$$

and the characteristic vibrational relaxation time scale by

$$\tau = \frac{1}{K_{1,0}\left(1 - e^{\theta_v/T}\right)} \quad . \tag{28}$$

48

In these equations, N represents the total number of oscillators, $\Theta v = k_p v/k_B$, with k_p being Planck's constant, v the frequency, and k_B Boltzmann's constant. $K_{1,0}$ is a constant dependent on the particular molecule.

Another physical process that could be important for hypersonic flow analysis is radiation. The incorporation of radiation effects involves rewriting the energy equation to include the radiant heat flux from the gas. Applying the first law of thermodynamics the modified energy equation can be written as

$$\frac{\partial(\rho e_i)}{\partial t} + \frac{\partial F'_c}{\partial x} + \frac{\partial G'_c}{\partial y} + \frac{\partial H'_c}{\partial z} = -\frac{\partial q_j^R}{\partial x_j} \quad , \tag{29}$$

where the heat-flux vector q_j^R can be expressed in terms of the frequency-dependent species intensity I_v as

$$q_j^R = \int_0^\infty \int_0^{4\pi} I_v l_j \, d\Omega dv \quad , \tag{30}$$

where l_j is the unit vector specifying the direction of propagation of I_v and l_1, l_2, l_3 are the associated direction cosines. I_v can be evaluated using the equation of radiative transfer in the quasi-equilibrium form as

$$l_j \frac{\partial I_v}{\partial x_j} = -\alpha_v \left(I_v - B_v \right) \quad , \tag{31}$$

where the unsteady term has been dropped due to the fact that the speed of light is many orders of magnitude greater than typical fluid speeds and α_v is the frequency-dependent absorption coefficient. The Planck function B_v is given by

$$B_v(T) = \frac{2k_p v^3/c^2}{\exp(vk_p/k_B T) - 1} \quad , \tag{32}$$

where k_p is the Planck constant, v is the frequency, c is the speed of light, and k_B is the Boltzmann constant. Thus, the energy equation is described by a complicated integro-differential relation. This equation can be greatly simplified by assuming the gas to be

thick and emission-dominated. Vincenti (Ref. 21) outlines how these simplifications can be implemented.

In addition, both translation and rotation nonequilibrium processes tend to reach equilibrium in approximate 10 collisions (Ref. 21). Consideration of physical events occurring in 10 mean free paths (10 collisions) would require solving the noncontinuum equations. Thus, rotation and translation can always be modeled as being in equilibrium within the Navier-Stokes approximation.

The various conservation equations are summarized in Figure 12. These equations can be solved in a variety of ways resulting in different levels of nonequilibrium physics. Several combinations of these equations are depicted in Figure 13.

No.	Conservation equations	No. of eq.	What quantities are obtained
1	Overall mass conservation eq.	1	ρ
2	Overall momentum conservation eq.	3	u, v, w
3	Overall energy conservation eq.	1	$E \longrightarrow T_{trans}$
4	Mass conservation eq. for each species	N_s	ρ_i
5	Vibrational energy conservation eq. for diatomic molecules	N_d	$e_{vib,s} \longrightarrow T_{vib,s}$
6	Electron momentum conservation eq.	3	Electric field $\vec{E}$
7	Electron energy conservation eq.	1	$e_{elec} \longrightarrow T_e$

Mach number range 10-30
Altitude 100,000 ft - non-continuum limit (~275,000ft)

Figure 12. Defining Equations for Multi-Temperature Hypersonic Flows

Model number	Model type	Temperatures modeled	Conservation equations (figure 12) to be solved
M-1	NS	T_{trans}	1, 2, 3
M-2	NS + CNE	$T_{trans} = T_{rot} = T_{vib}$,	1, 2, 3, 4
M-3	NS + CNE + TNE	$T_{trans} = T_{rot}, T_{vib}$	1, 2, 3, 4, 5
M-4	NS + CNE + TNE	$T_{trans} = T_{rot}, T_{vib}, T_{elec}$	1, 2, 3, 4, 5, 6
M-5	NS + CNE + TNE	$T_{trans} = T_{rot}, T_{vib}, T_{elec}$	1, 2, 3, 4, 5, 6, 7

NS — Navier-Stokes
CNE — Chemical non-equilibrium
TNE — Thermal non-equilibrium

Figure 13. Equation Modeling Hierarchy

An extensive literature search was performed for chemical and thermal nonequilibrium measurements. Several sources of shock tube experiments were found (Refs. 23 and 24) that could be used to calibrate nonequilibrium air chemistry mechanisms. The data was considered sufficiently accurate to compare various chemical nonequilibrium models (i.e. one-temperature models). The same was not true, however, for thermal nonequilibrium (multi-temperature) experimental data sets. Very few data sets were found which contained useful measurements of thermal nonequilibrium processes. Based on the results of the literature search, it was decided that only one-temperature air chemistry models could be calibrated to engineering accuracy and would be considered in this phase of the contract. Thus, rotation, translation, and vibration modes would all be assumed to be in equilibrium. The conservation equations needed to model this type of flow is depicted as model 2 (M-2) in Figure 13.

Thermal radiation from the shock front can be significant at extremely high speeds (above 8-10 km/sec). In general, thermal radiation from the shock front is dependent on the body bluntness and the free-stream velocity and density of the gas. The radiation contribution to the total (convective and radiative) stagnation point heat transfer increases with velocity, density, and body bluntness while the depth of the nonequilibrium region behind the bow shock varies inversely with gas density. For a blunt (nose radius of 3 m.) vehicle traveling at 7.6 km/sec, the convective heating will be at least an order of magnitude larger than the (equilibrium) radiative contribution above an altitude of 46 km (Ref. 25). The radiative contribution will be even smaller if this vehicle had a sharper nose geometry and/or traveled at higher altitudes. Hence, thermal radiation from the shock front can be assumed to be small relative to convective heat transport mechanisms and was not modeled.

3.3 CHEMICAL REACTION MODEL DEVELOPMENT

A summary of the chemical reaction model development is depicted in Figure 14. Details of all stages of the development process are documented below.
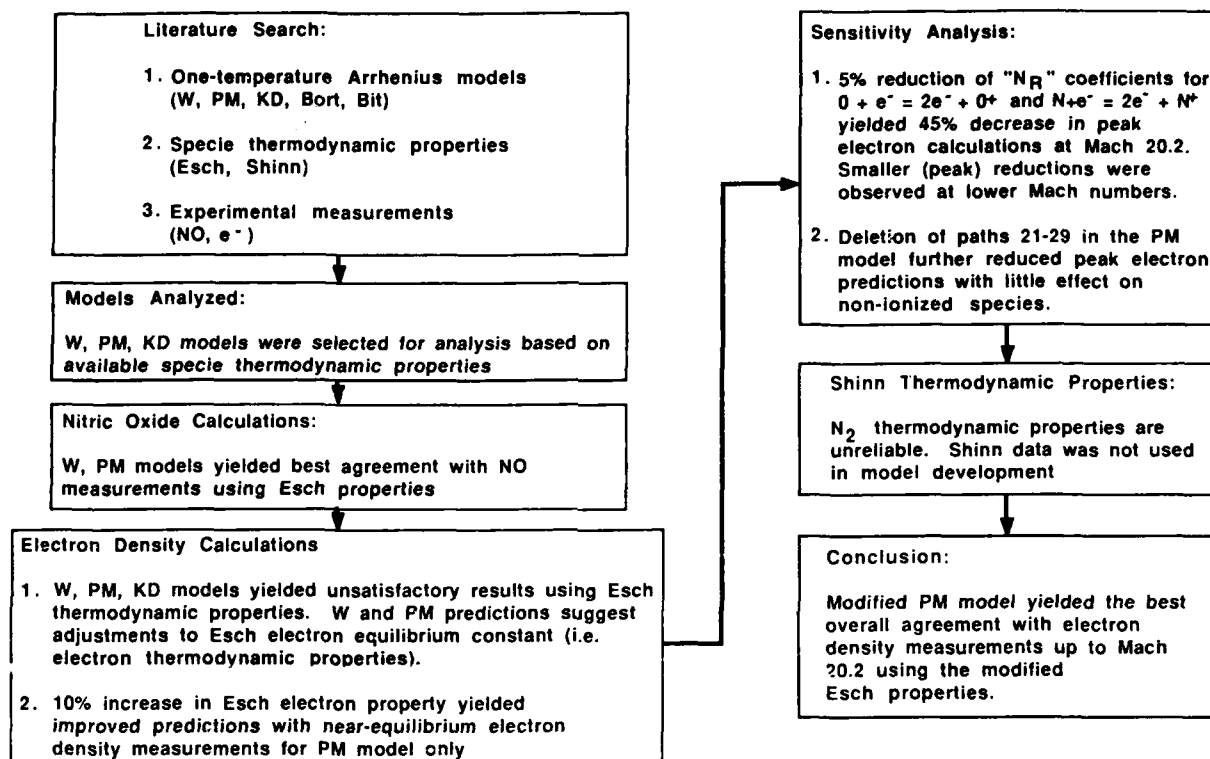
Figure 14. Summary of Air Chemistry Model Development Process

3.3.1 Literature Search

An extensive literature search for air ionization models, specie thermodynamic properties (enthalpy, specific heat capacity, entropy, and Gibb's free energy) and specie experimental measurements was performed during Phase I. Many air ionization models were identified, with each model utilizing different chemical species, reaction paths, rate coefficients, and application features. For instance, a model may depend on one (translation) or two (translation and vibration) temperatures, may have up to 15 chemical species, may use an Arrhenius or non-Arrhenius reaction rate, and may have as many as 50-60 reaction paths. These variations make a thorough analysis extremely tedious and difficult. To insure a feasible analysis, the following assumptions and restrictions were employed:

a. only Arrhenius reaction rates were considered;

b. chemical reaction rates were assumed to depend only on the translational temperature (T), i.e., one temperature reaction rates;

52

c. chemical reaction rates were assumed to be valid up to 17000 K;

d. argon has a negligible effect in high temperature air reactions.

Of the many models examined only five air ionization models utilized an Arrhenius reaction model of the form $A_r(T)^{N_r}\exp(-E_r/T)$ where A_r, N_r, E_r are rate coefficients. These models were developed by K. Wray (hereafter abbreviated by W), C. Park and G. Menees (PM), S. Kang and M. Dunn (KD), D. Bittker (Bit), and M. Bortner (Bort) (Refs. 26-30). The W model is well known and represents one of the simplest (18 reaction paths, 7 species) ionization models conceived. The PM model was derived to investigate meteoroid wakes and both the KD and Bort models were employed in flowfield analyses about reentry vehicles. Finally, the Bit model was employed in Ref. 29 to analyze shock-tube air reactions. The reaction paths and rate coefficients for each model are depicted in Tables 1 through 5 and summarized in Table 6. Note that the W model depicted in Table 1 has been modified from its original form. Modifications included the elimination of $N_2 + O_2 = 2$ NO, based on Camac and Feinberg's recommendation (Ref. 23) and the assumption that argon has a negligible effect in high temperature air reactions.

Table 1. Wray Air Model

Reaction	M	A_r	N_r	E_r
$O_2 + M \rightarrow 2O + M$	N, NO	3.62×10^{19}	-1.0	59500
	N_2	4.8×10^{20}	-1.5	59500
	O_2	1.9×10^{21}	-1.5	59500
	O	6.4×10^{23}	-2.0	59500
$N_2 + M \rightarrow 2N + M$	$O, O_2,$ NO	1.9×10^{17}	-0.5	113000
	N_2	4.8×10^{17}	-0.5	113000
	N	4.1×10^{22}	-1.5	113000
$NO + M \rightarrow N + O + M$	N_2, O_2	3.9×10^{20}	-1.5	75500
	NO, O, N	7.9×10^{21}	-1.5	75500
$NO + O \rightarrow O_2 + N$		3.2×10^{9}	1.0	19700
$N_2 + O \rightarrow NO + N$		7.0×10^{13}	0.0	38000
$N + O \rightarrow NO^+ + e^-$		6.5×10^{11}	0.0	31900

M represents the collision specie in a given reaction

Table 2. Park and Menees Air Model

Reaction	M	A_r	N_r	E_r
$O_2 + M \rightarrow O + O + M$	N	8.25×10^{19}	-1.0	59,500
	O	8.25×10^{19}	-1.0	59,500
	N_2	2.75×10^{19}	-1.0	59,500
	O_2	2.75×10^{19}	-1.0	59,500
	NO	2.75×10^{19}	-1.0	59,500
$N_2 + M \rightarrow N + N + M$	N	1.11×10^{22}	-1.6	113,200
	O	1.11×10^{22}	-1.6	113,200
	N_2	3.7×10^{21}	-1.6	113,200
	O_2	3.7×10^{21}	-1.6	113,200
	NO	3.7×10^{21}	-1.6	113,200
$NO + M \rightarrow N + O + M$	N	4.6×10^{17}	-0.5	75,500
	O	4.6×10^{17}	-0.5	75,500
	N_2	2.3×10^{17}	-0.5	75,500
	O_2	2.3×10^{17}	-0.5	75,500
	NO	2.3×10^{17}	-0.5	75,500
$NO + O \rightarrow N + O_2$		2.16×10^{8}	1.29	19,220
$O + N_2 \rightarrow N + NO$		3.18×10^{13}	0.10	37,700
$N + O \rightarrow NO^+ + e^-$		1.53×10^{10}	0.37	32,000
$O + e^- \rightarrow O^+ + e^- + e^-$		1.95×10^{34}	-3.78	158,500
$N + e^- \rightarrow N^+ + e^- + e^-$		1.25×10^{35}	-3.82	168,600
$O + O \rightarrow O_2^+ + e^-$		3.85×10^{10}	0.49	80,600
$O + O_2^+ \rightarrow O_2 + O^+$		6.85×10^{13}	-0.52	18,600
$N_2 + N^+ \rightarrow N + N_2^+$		9.85×10^{12}	-0.18	12,100
$N + N \rightarrow N_2^+ + e^-$		1.79×10^{10}	0.77	67,500
$O + NO^+ \rightarrow NO + O^+$		2.75×10^{13}	0.01	51,000
$N_2 + O^+ \rightarrow O + N_2^+$		6.33×10^{13}	-0.21	22,200
$N + NO^+ \rightarrow NO + N^+$		2.21×10^{15}	-0.02	61,100
$O_2 + NO^+ \rightarrow NO + O_2^+$		1.03×10^{16}	-0.17	32,400
$NO^+ + N \rightarrow N + N_2^+$		1.70×10^{13}	0.40	35,500

M represents the collision specie in a given reaction

54

Table 3. Dunn and Kang Air Model

Reaction	M	A_r	N_r	E_r
$O_2 + M \rightarrow 2O + M$	N, NO	3.6×10^{18}	-1.0	59400
$N_2 + M \rightarrow 2N + M$	O, NO, O_2	1.9×10^{17}	-0.5	113000
$NO + M \rightarrow N + O + M$	O_2, N_2	3.9×10^{20}	-1.5	75500
$O + NO \rightarrow N + O_2$		3.2×10^{9}	1.0	19700
$O + N_2 \rightarrow N + NO$		7.0×10^{13}	0.0	38000
$N + N_2 \rightarrow 2N + N$		4.085×10^{22}	-1.5	113000
$O + N \rightarrow NO^+ + e^-$		1.4×10^{6}	1.5	31900
$O + e^- \rightarrow O^+ + 2e^-$		3.6×10^{31}	-2.91	158000
$N + e^- \rightarrow N^+ + 2e^-$		1.1×10^{32}	-3.14	169000
$O + O \rightarrow O_2^+ + e^-$		1.6×10^{17}	-.98	80800
$O + O_2^+ \rightarrow O_2 + O^+$		2.92×10^{18}	-1.11	28000
$N_2 + N^+ \rightarrow N + N_2^+$		2.02×10^{11}	0.81	13000
$N + N \rightarrow N_2^+ + e^-$		1.4×10^{13}	0.0	67800
$O + NO^+ \rightarrow NO + O^+$		3.63×10^{15}	-.6	50800
$N_2 + O^+ \rightarrow O + N_2^+$		3.4×10^{19}	-2.0	23000
$N + NO^+ \rightarrow NO + N^+$		1.0×10^{19}	-.93	61000
$O_2 + NO^+ \rightarrow NO + O_2^+$		1.8×10^{15}	0.17	33000
$O + NO^+ \rightarrow O_2 + N^+$		1.34×10^{13}	0.31	77270
$O_2 + O \rightarrow 2O + O$		9.0×10^{19}	-1.0	59500
$O_2 + O_2 \rightarrow 2O + O_2$		3.24×10^{19}	-1.0	59500
$O_2 + N_2 \rightarrow 2O + N_2$		7.2×10^{18}	-1.0	59500
$N_2 + N_2 \rightarrow 2N + N_2$		4.7×10^{17}	-0.5	113000
$NO + M \rightarrow N + O + M$	O, N, NO	7.8×10^{20}	-1.5	755000
$O_2 + N_2 \rightarrow NO + NO^+ + e^-$		1.38×10^{20}	-1.84	141000
$NO + N_2 \rightarrow NO + e^- + N_2$		2.2×10^{15}	-0.35	108000
$NO + O_2 \rightarrow NO^+ + e^- + O_2$		8.8×10^{15}	-0.35	108000

M represents the collision specie in a given reaction

Table 4. Bittker Air Model

Reaction	M	A_r	N_r	$E_r R$
$N + O_2 \rightarrow NO + O$		6.4×10^9	1.0	6250
$O + N_2 \rightarrow NO + N$		1.8×10^{14}	0.0	76250
$N + O + M \rightarrow NO + M$	All but N_2O	6.4×10^{16}	-0.5	0
$N + O + N_2O \rightarrow NO + N_2O$		1.44×10^{17}	-0.5	0
$O + O + M \rightarrow O_2 + M$	All	5.7×10^{13}	0	-1788
$N + N + M \rightarrow N_2 + M$	All	2.8×10^{17}	-0.75	0
$NO + O + M \rightarrow NO_2 + M$	All but N_2	5.62×10^{15}	0	-1160
$NO + O + N_2 \rightarrow NO_2 + N_2$		8.71×10^{15}	0	-1160
$N_2O + M \rightarrow N_2 + O + M$	All	1.42×10^{14}	0	51280
$O + N_2O \rightarrow N_2 + O_2$		6.23×10^{13}	0	24520
$NO^+ + e^- \rightarrow N + O$		1.45×10^{21}	-1.5	0
$O^+ + e^- + M \rightarrow O + M$	All but N, O_2, NO, O	2.0×10^{26}	-2.5	0
$O^+ + e^- + N \rightarrow O + N$		6.0×10^{24}	-2.5	0
$O^+ + e^- + O_2 \rightarrow O + O_2$		9.0×10^{26}	-2.5	0
$O^+ + e^- + NO \rightarrow O + NO$		1.0×10^{28}	-2.5	0
$O^+ + e^- + O \rightarrow O + O$		6.0×10^{24}	-2.5	0
$O_2 + e^- + M \rightarrow O_2^- + M$	All but N_2	1.52×10^{21}	-1.0	1190
$O_2 + e^- + N_2 \rightarrow O_2^- + N_2$		3.04×10^{16}	-1.0	1190
$O_2 + O^- \rightarrow O_2^- + O$		6.0×10^{12}	0	0

M represents the collision specie in a given reaction

Table 5. *Bortner Air Model*

Reaction	A_r	N_r	E_r
$O_2 + M \rightarrow O + O + M$			
$M = O_2$	1.37×10^{-5}	-.83	59400
O	1.50×10^{-4}	-1	59400
N_2	2.2×10^{-3}	-1.7	59400
N, NO	2.4×10^{-3}	-1.8	59400
$N_2 + M \rightarrow N + N + M$			
$M = N_2$	8.3×10^{-6}	-.75	113200
N	5.0×10^{-2}	-1.5	113200
O_2, O, NO	4.8×10^{-6}	-.82	113200
$NO + M \rightarrow N + O + M$			
$M = NO, O, N$	1.32×10^{-2}	-1.5	75400
O_2, N_2	1.5×10^{-9}	0	75400
$O_3 + M \rightarrow O + O_2 + M$			
$M = N_2$	2.1×10^{-5}	-1.35	12300
O_2, N, O, NO	2.3×10^{-5}	-1.35	12300
$O + N_2 \rightarrow N + NO$	1×10^{-10}	0	38000
$O + NO \rightarrow N + O_2$	7.2×10^{-17}	1.5	19100
$O_2 + O_2 \rightarrow O + O_3$	2.9×10^{-11}	0	50190
$N + O \rightarrow NO^+ + e^-$	8.6×10^{-13}	0	31900
$N_2 + M \rightarrow N_2^+ + e^- + M$			
$M = N_2$	3.0×10^{-20}	2.0	181000
e^-	5.3×10^{-11}	0.5	181000
$O_2 + M \rightarrow O_2^+ + e + M$			
$M = N_2$	1.0×10^{-20}	1.5	140000
O_2	2.0×10^{-20}	1.5	140000
e^-	2.2×10^{-11}	0.5	140000
$O_2 + e^- + M \rightarrow O_2^- + M$			
$M = O_2$	4.2×10^{-27}	-1.0	600
N_2	1×10^{-21}	0	0
$O_2^- + O_3 \rightarrow O_2^- + O_3^-$	3×10^{-10}	T/300	0
$O_2^- + O \rightarrow O_3 + e^-$	2.5×10^{-10}	T/300	0
$O_3 + e^- \rightarrow O^- + O_2$	4×10^{-11}	T/300	0
$X^+ + Y^- \rightarrow X + Y$	6×10^{-5}	-1	0
$X^+ Y^- + M \rightarrow X + Y + M$	3×10^{-19}	-2.5	0
$N_2^+ + O_2 \rightarrow N_2 + O_2^+$	1×10^{-10}	T/300	0
$N_2^+ + NO \rightarrow N_2 + NO^+$	5×10^{-10}	T/300	0
$N_2^+ + O \rightarrow NO^+ + N$	2.5×10^{-10}	T/300	0
$O_2^+ + NO \rightarrow O_2 + NO^+$	8×10^{-10}	T/300	0

M represents the collision specie in a given reaction

Table 6. Summary of Species, Paths, and Rate Constants for Various Air Models

Reference	Species	Number of reaction paths	Forward reaction rate
K. L. Wray	$O, O_2, N, N_2, NO, NO^+, e^-$	18	$A_r (T)^{N_r} exp(-E_r/T)$
D. A. Bittker	$O, O^+, O^-, O_2^-, O_2, N, N_2, NO,$ NO^+, N_2O, NO_2, e^-	89	$A_r (T)^{N_r} exp(-E_r/T)$
M. H. Bortner	$O, O^-, O_2, O_2^-, O_2^+, O_3, O_3^-$ $N, N^+, N^-, N_2, N_2^+, NO, NO^+$	>38	$A_r (T)^{N_r} exp(-E_r/T)$
C. Park & G. P. Menees	$O, O^+, O_2, O_2^+ +, N, N^+, N_2, N_2^+,$ NO, NO^+, e^-	29	$A_r (T)^{N_r} exp(-E_r/T)$
M. G. Dunn & S. W. Kang	$O, O^+, O_2, O_2+, N, N^+, N_2, N_2^+$ NO, NO^+, e^-	32	$A_r (T)^{N_r} exp(-E_r/T)$

where A_r, N_r, E_r = reaction rate constants
T = temperature

Specie thermodynamic properties, specifically entropy, Gibbs free energy, enthalpy, and specific heat capacity are important components to model development. These properties must be accurately known up to very high temperatures (15000 K-25000 K). Two sources for thermodynamic properties were found. D. Esch et al, (Ref. 31) derived polynomial relationships for the thermodynamic properties of 99 elemental and molecular species More than one half of all the species were modeled up to 15000 K. Similarly, J. Shinn (Ref. 32) obtained polynomial relationships for thermodynamic properties of 11 air ionization species ($O, O_2, N, N_2, NO, O+, O_2+, N+, N_2+, NO+, e^-$) up to 30000 K. Both Esch and Shinn utilized the following relationships for the specific heat capacity (C_{ps}), enthalpy (h_s), entropy (S_s), and Gibbs free energy (f_s) of specie s:

$$C_{Ps}/R = Z_{1s} + Z_{2s}T + Z_{3s}T^2 + Z_{4s}T^3 + Z_{5s}T^4, \tag{33}$$

$$h_s/RT = Z_{1s} + Z_{2s}T/2 + Z_{3s}T^2/3 + Z_{4s}T^3/4 + Z_{5s}T^4/5 + Z_{6s}/T, \tag{34}$$

$$S_s/R = Z_{1s}ln(T) + Z_{2s}T + Z_{3s}T^2/2 + Z_{4s}T^3/3 + Z_{5s}T^4/4 + Z_{7s}, \tag{35}$$

$$f_s/RT = Z_{1s}[1.-ln(T)] - Z_{2s}T/2 - Z_{3s}T^2/6 - Z_{4s}T^3/12 - Z_{5s}T^4/20 + Z_{6s}/T - Z_{7s}. \tag{36}$$

A careful examination of Shinn's curve-fit coefficients revealed that inaccurate results are obtained for N_2 near 13500 K - 14990 K. Specifically, negative N_2 heat

capacities were calculated using coefficients Z_{1s} through Z_{5s}. Coefficients Z_{1s}-Z_{5s} are also used to estimate entropy, enthalpy, and free energy, hence, these properties are also unreliable. No anomaly was identified for the remaining 10 species. Because of the discrepancies in Shinn's data, Esch's thermodynamic data was used in the model development.

Near the end of Phase I a third source of thermodynamic properties was obtained from R. Gupta of NASA Langley Research Center. Gupta's curve-fit coefficients models the previously mentioned 11 air species up to 25000 K in the same form as Equations (33) through (36). Unfortunately, it was not made available in time to use in the development of the chemistry reaction model, however, his results will be examined in Phase II.

Not all species of interest have been modeled to high temperatures (15000 K-25000 K). Molecular species N_2O and NO_2 used by Bittker can be computed only up to 6000 K while species O_3 and O_3^- considered by Bortner have not been modeled at all. Due to the lack of adequate thermodynamic data for these species both Bittker and Bortner models were not analyzed.

Finally, experimental measurements are needed to validate the air models at high speeds. An extensive literature search identified only two useful sources of specie measurements. Camac and Feinberg (Ref. 23) recorded the formation of nitric oxide (NO) in shock heated air for Mach Numbers 6-11. Peak NO concentrations and time-to-peak periods were measured in this Mach number range. For Mach numbers above 14, electron density measurements behind a shock front were investigated by Lin (Refs. 24, 33). Complete electron density histories were measured for Mach Numbers 14-20.

3.3.2 Nitric Oxide Calculations

In this part of the analysis the accuracy of the W, PM, and KD models were assessed in a comparison of nitric oxide calculations with shock tube measurements by Camac and Feinberg (Ref. 23). Peak NO predictions and measurements are depicted in Figure 15. The W, PM, and KD models yielded results within the measurement band.
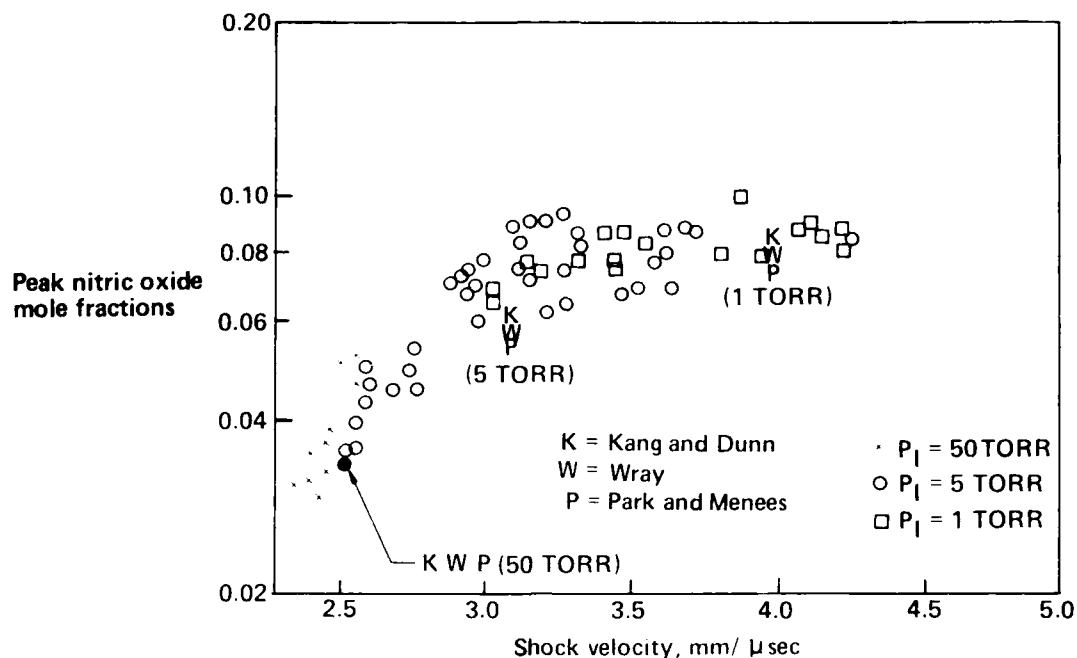
Figure 15. Comparison of KD, W, and PM Model Calculations With Peak Nitric Oxide Measurements of Camac and Feinberg (Reference 23)

The predicted time-to-peak periods are revealed in Figure 16. All models predicted much higher peak periods at a shock velocity of 2.5 mm/micro-sec. The differences between measurements and predictions may be due to Camac and Feinberg's interpretation of the peak time. Infrared radiation histories (from which NO concentrations were obtained) at this shock velocity have longer molecular relaxation periods resulting in a "flat" peak history that can be difficult to interpret. Nevertheless, all models predicted identical results at this velocity. Calculations at higher velocities indicated that the W and PM models yielded good agreement with measurements. Examination of Figures 15 and 16 show that the W and PM models are suitable for high temperature NO calculations.

3.3.3 Electron Density Calculations

W, PM, and the KD electron density histories downstream of a shock wave are compared with Lin et. al. (Ref. 24) shock tube measurements in Figures 17 through 19 for Mach 15.6, 18.5, and 20.2. All results were computed with the original Esch thermodynamic properties. Figure 17 shows all models underpredicted peak and
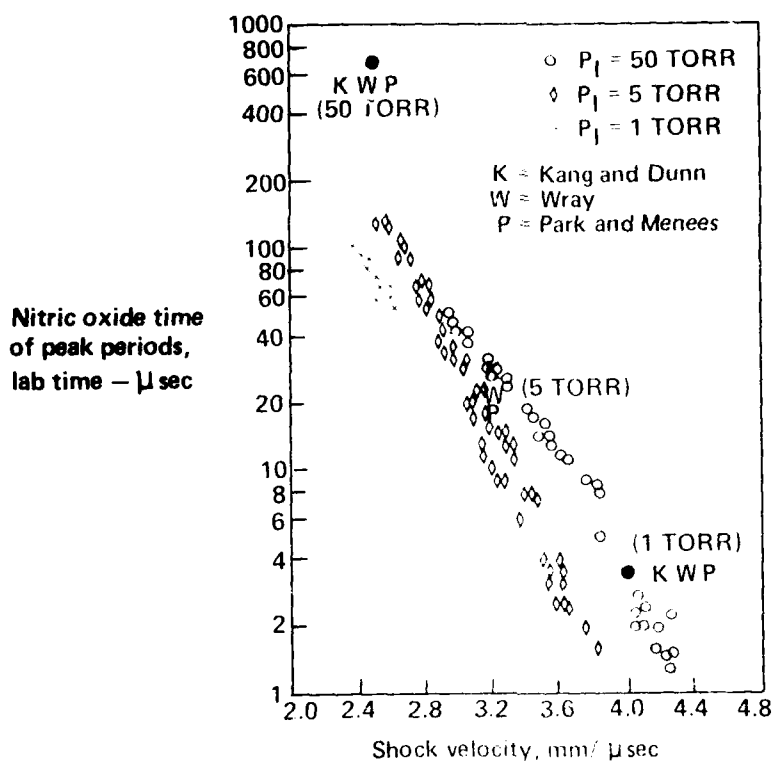
Figure 16. Comparison of KD, W, and PM Model Calculations With Camac and Feinberg's Measured Nitric Oxide "Time-of-Peak" Periods

Figure 17. W, PM, and KD Electron Density Calculations (particles/cm^3) Versus Distance, (cm) Downstream of a Shock Front for Mach 15.6 Using Esch Thermodynamic Properties

Figure 18. W, PM, and KD Density Calculations (particles/cm^3) Versus Distance (cm) Downstream of a Shock Front for Mach 18.5 Using Esch Thermodynamic Properties

Figure 19a. W, PM, and KD Electron Density Calculations (particles/cm^3) Versus Distance (cm) Downstream of a Shock Front for Mach 20.2 Using Esch Thermodynamic Properties

Figure 19b. W and PM Electron Density Calculations (particles/cm³) Versus Distance (cm) Downstream of a Shock Front for Mach 20.2 Using Esch Thermodynamic Properties

equilibrium electron measurements by approximately 40% at Mach 15.6 and identify the importance of obtaining accurate equilibrium predictions. At Mach 18.5 (Fig. 18) the KD model overpredicted peak electron measurements by approximately 4 times while both W and PM results underestimated measurements. The differences between models is more evident at Mach 20.2 depicted in Figure 19 (a and b). The KD peak electron densities are now 25 times larger than measurements, the PM results are 50% larger, and again the W model underpredicted measurements by 70%. The W model yielded results that were consistently lower than the measurements at all shock velocities. All models predicted earlier time-to-peak periods at Mach 18.5 and 20.2.

The results presented in Figures 17 through 19 illustrate the importance of obtaining accurate equilibrium electron densities. The equilibrium concentration is governed by the equilibrium constant (K_{eq}) which can be defined in terms of entropy and enthalpy,

$$K_{eq} = \left[p_{atm} / RT \right]^{\sum_{s=1}^{N_S} \left(b_{rs} - a_{rs} \right)} \exp\left[(S_s / R) - (h_s / RT) \right]$$

$$= \left[p_{atm} / RT \right]^{\sum_{S=1}^{N_S} \left(b_{rs} - a_{rs} \right)} \exp\left\{ \sum_{s=1}^{N_S} \left(b_{rs} - a_{rs} \right) \left[Z_{1s} (\ln T - 1) \right. \right.$$

$$\left. \left. + Z_{2s} T/2 + Z_{3s} T^2/6 + Z_{4s} T^3/12 + Z_{5s} T^4/20 - Z_{6s} T + Z_{7s} \right] \right\} \tag{37}$$

where N_S = the number of species, a_{rs}, b_{rs} = stoichiometric coefficients of the sth specie in the rth reaction. The latter expression was obtained from polynomial relationships for entropy and enthalpy mentioned earlier. Note that K_{eq} can be modified by varying the "Z_{7s}" coefficient.

Improved results were obtained using the (modified) Esch thermodynamic properties when the Z_{7s} coefficient for the electron density was increased by 10% from its original value. These results are shown in Figures 20 through 22. All models showed significant improvements at Mach 15.6 (Fig. 20). A 10% increase in (electron) Keq resulted in a 45% increase in peak and equilibrium concentrations. At Mach 18.5 (Fig. 21) the KD model continued to overpredict measurements at all locations downstream of the shock front. The PM model adequately predicted equilibrium concentrations but overshoots peak experimental data. Satisfactory results were obtained with the W model at all stations. Electron histories at Mach 20.2 are depicted in Figure 22 (a and b). The PM and KD models yielded results much higher than measurements. The W model accurately reproduced the peak concentration and the time-to-peak period but underpredicted the near-equilibrium value.

Figure 20. W, PM, and KD Electron Density Calculations (particles/cm³) Versus Distance (cm)
Downstream of a Shock Front for Mach 15.6 Using Modified Esch Thermodynamic Properties
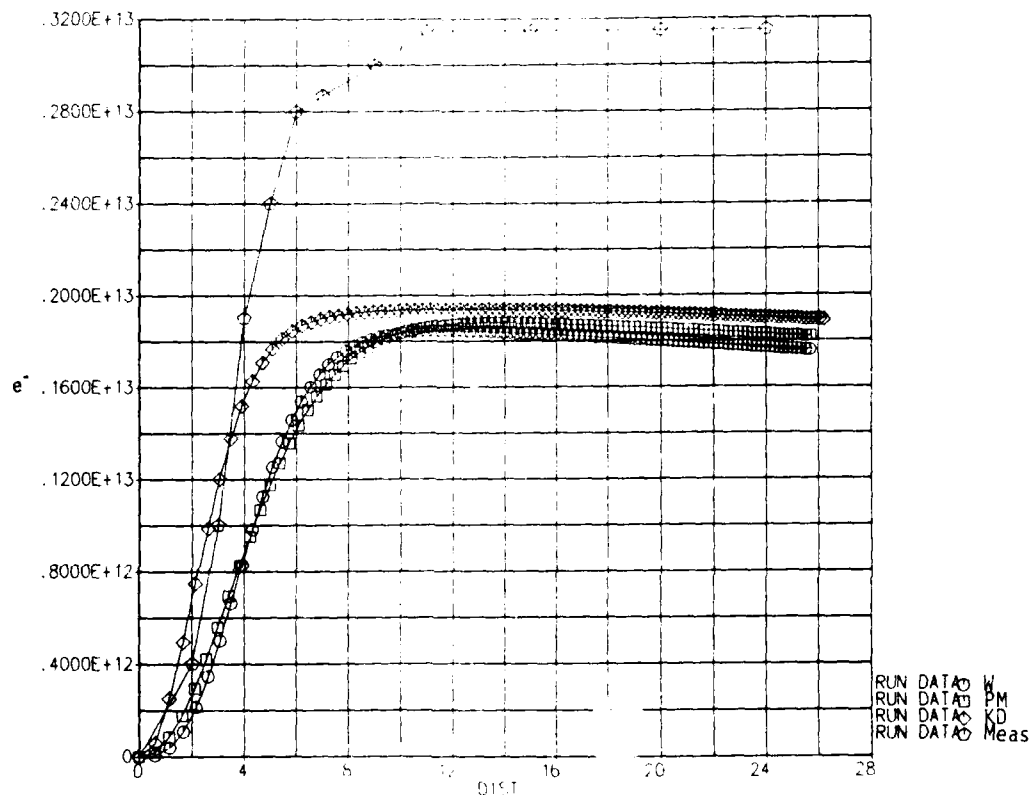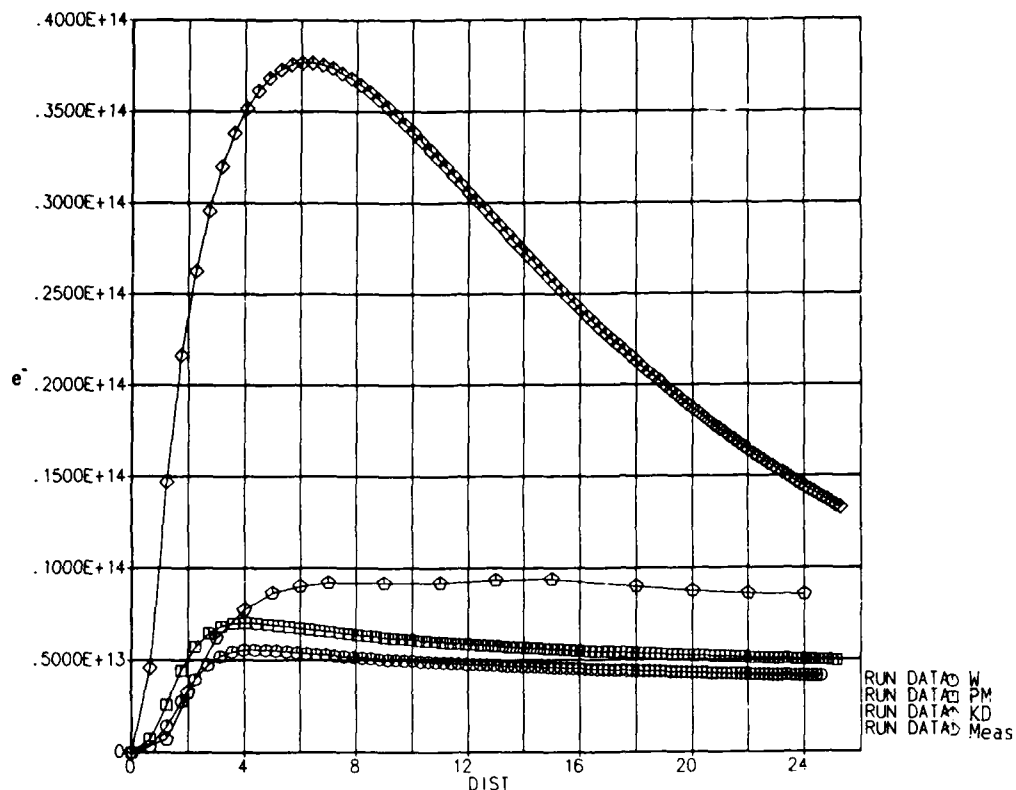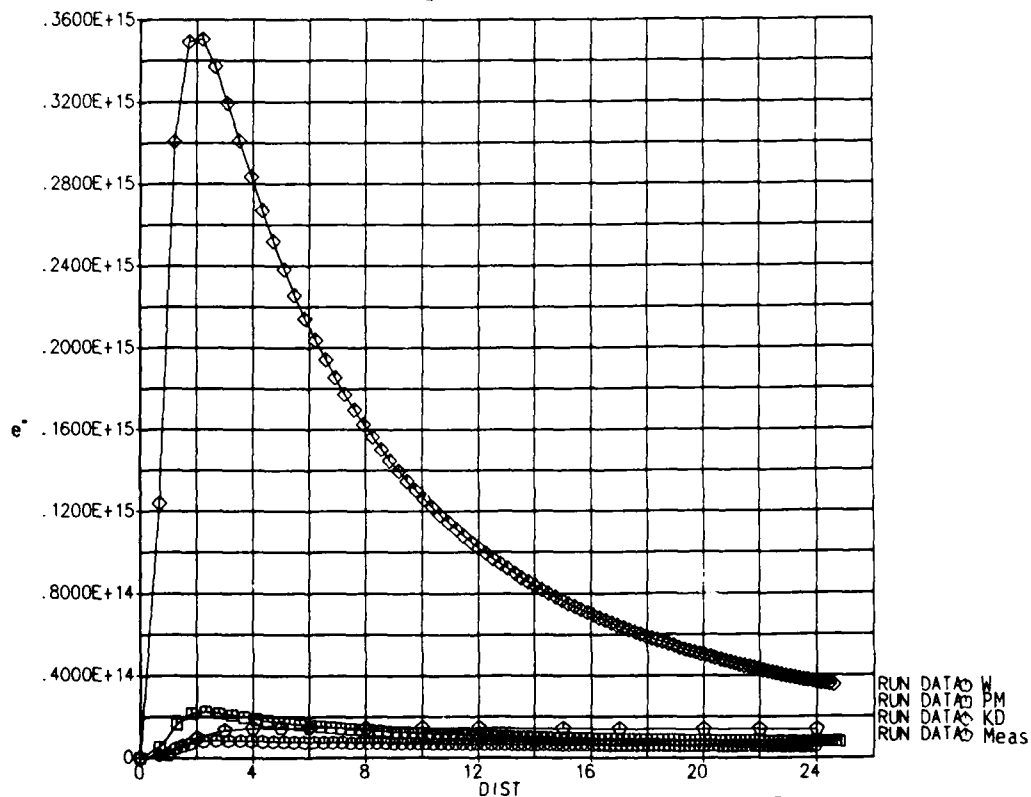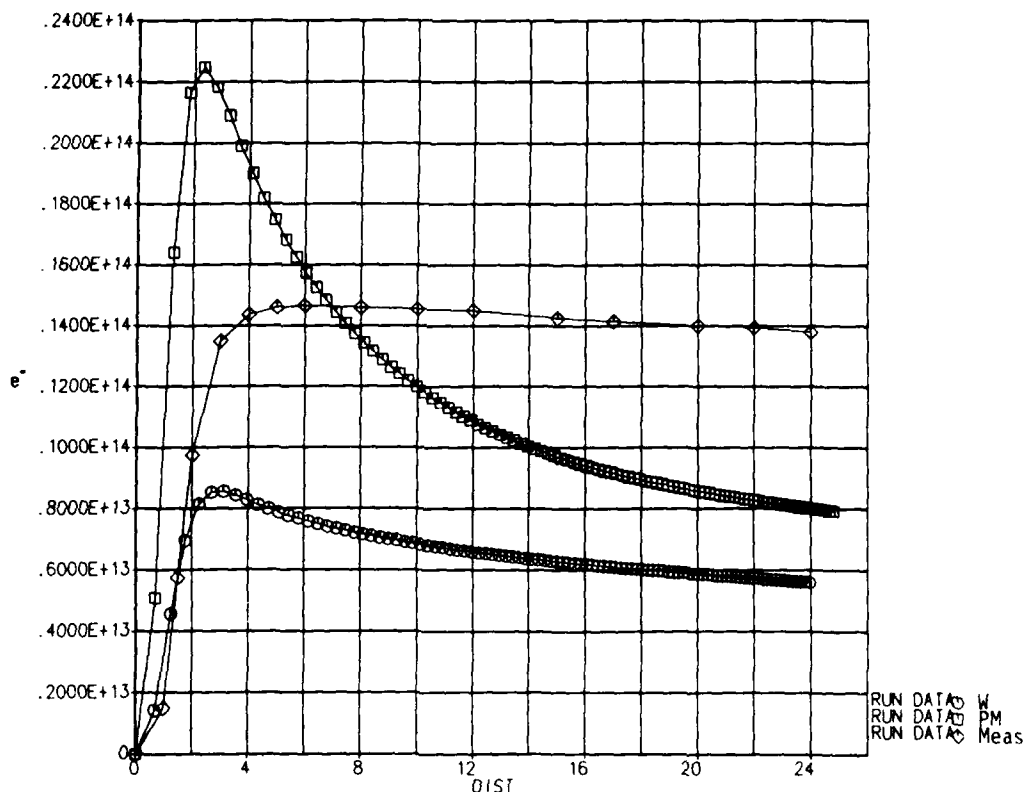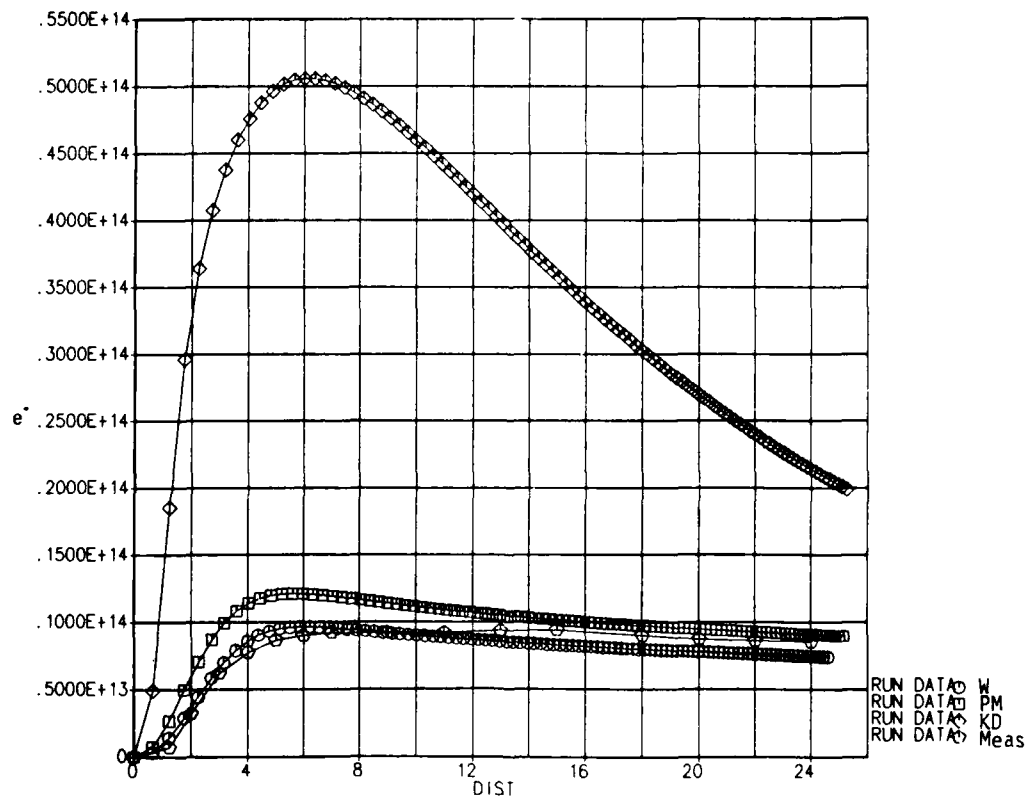

Figure 21. W, PM, and KD Electron Density Calculations (particles/cm³) Versus Distance (cm)
Downstream of a Shock Front for Mach 18.5 Using Modified Esch Thermodynamic Properties

65
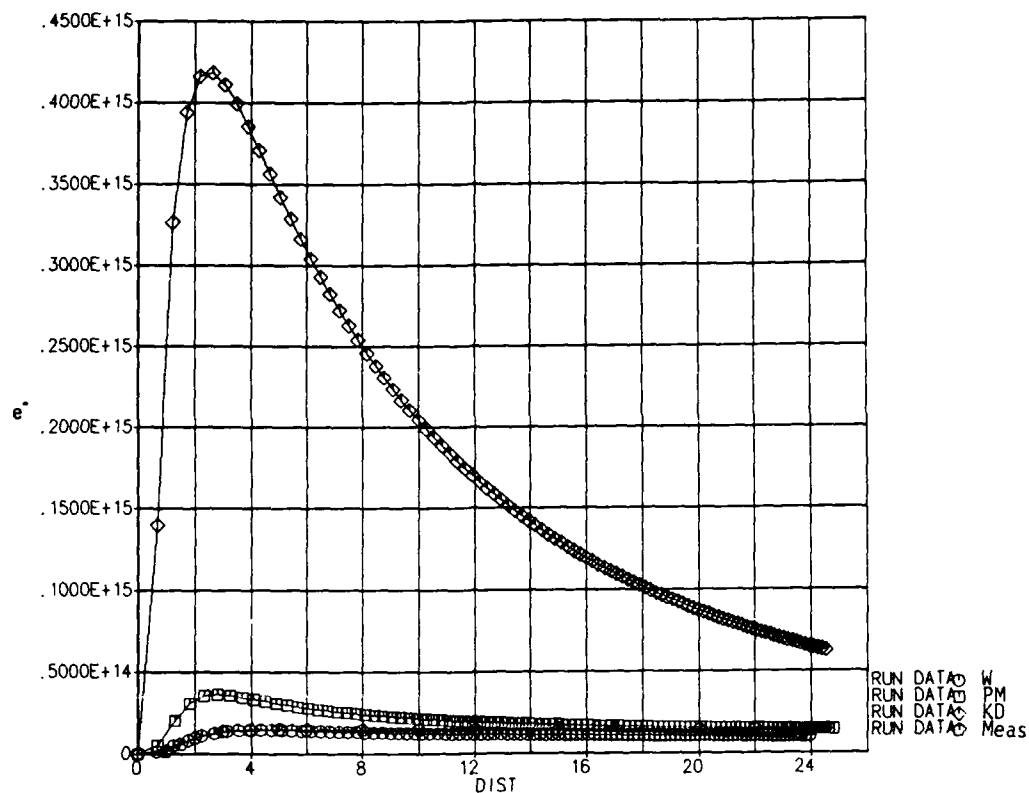
Figure 22a. W, PM, and KD Electron Density Calculations (particles/cm^3) Versus Distance (cm)
Downstream of a Shock Front for Mach 20.2 Using Modified Esch Thermodynamic Properties
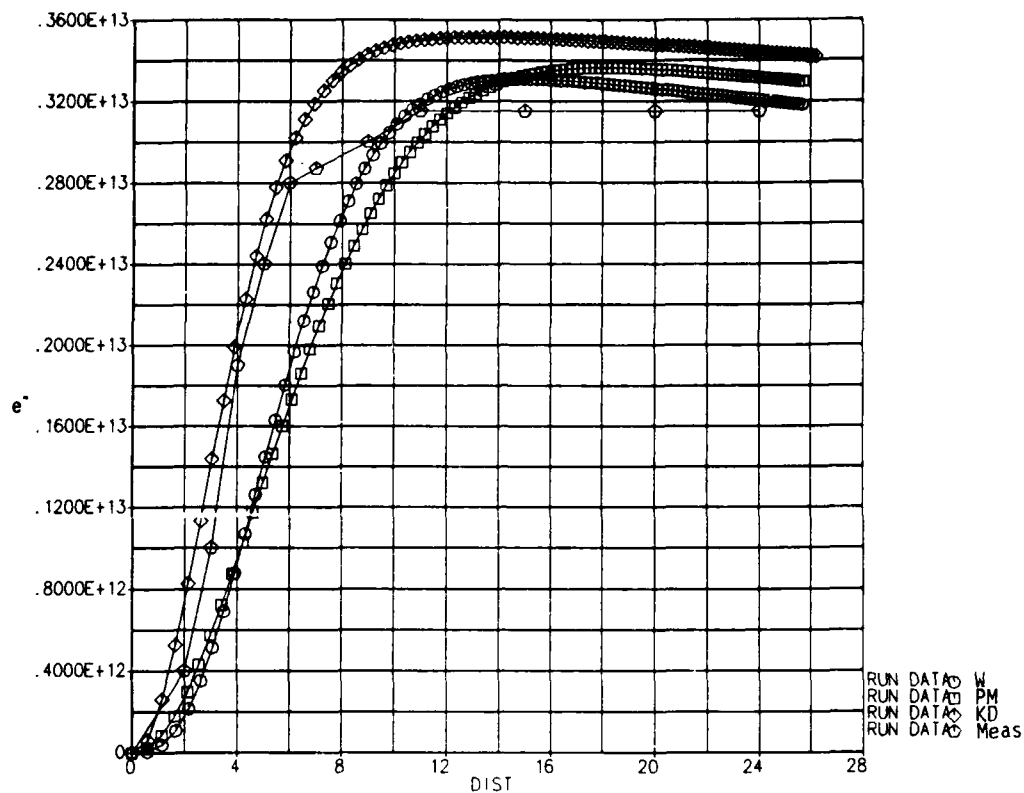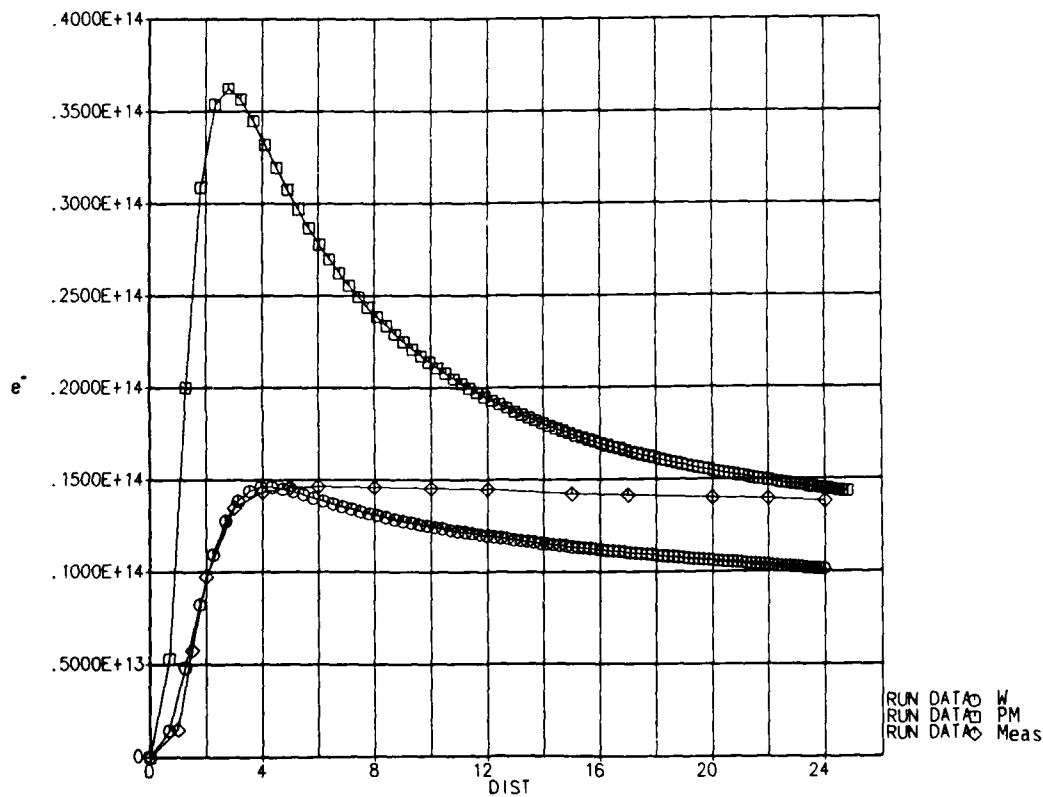

Figure 22b. W and PM Electron Density Calculations (particles/cm^3) Versus Distance (cm) Downstream
of a Shock Front for Mach 20.2 Using Modified Esch Thermodynamic Properties

3.3.4 Sensitivity Analysis

W and PM analytical results depicted in Figures 20 through 22 are rearranged in Figures 23 and 24 for Mach 15.6, 18.5, and 20.2. Although the W and PM models continue to yield unsatisfactory results they represent a feasible beginning for the sensitivity analysis.

The W model satisfactorily predicted peak concentrations but underpredicted near-equilibrium concentrations above Mach 15.6 (Fig. 23). The W model has only one reaction path directly responsible for electron production and several non-ionized paths that can have an indirect effect (Table 1). Perturbation of the W model rate coefficients (A_r, N_r, E_r) by one or two orders of magnitude failed to yield satisfactory peak and near-equilibrium values.

The PM model, on the other hand, yielded satisfactory equilibrium concentrations but predicted higher peak densities above 15.6 (Fig. 24). The PM model (Table 2) has many more reaction paths (and rate coefficients) which directly and indirectly affect

Figure 23. W Electron Density Calculations (particles/cm^3) Versus Distance (cm) Downstream of a Shock Front for Mach 15.6, 18.5, and 20.2 Using Modified Esch Thermodynamic Properties
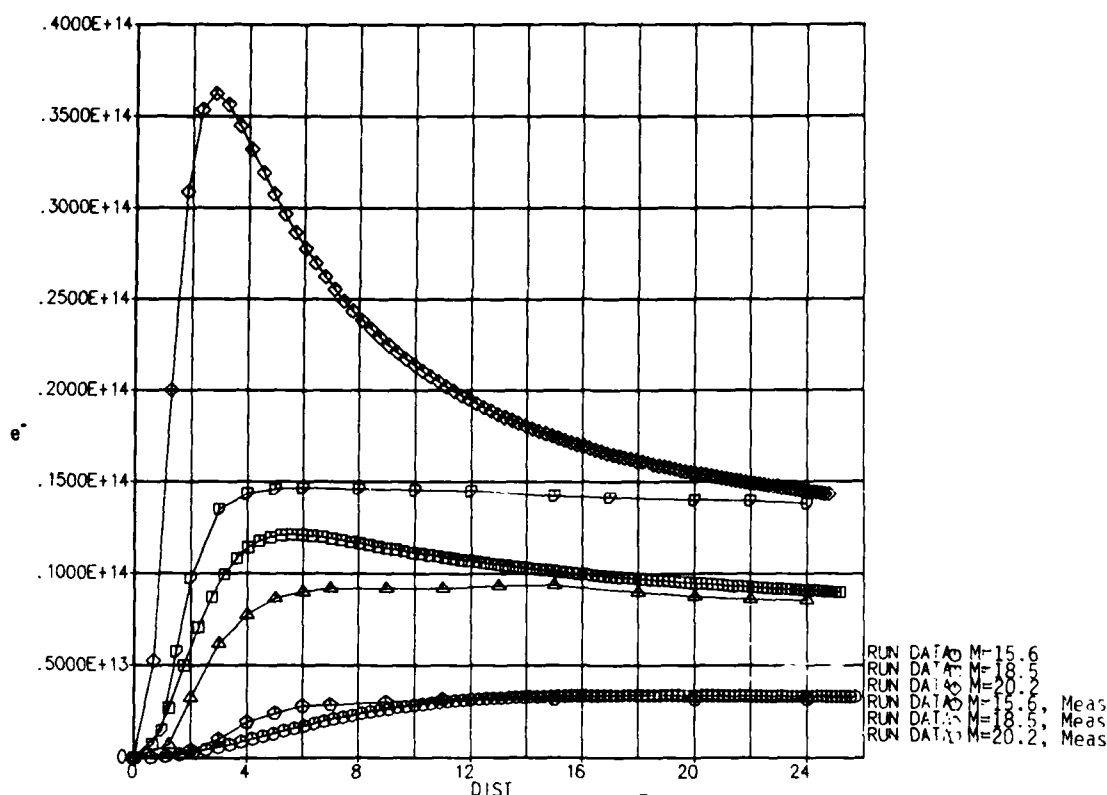
Figure 24. PM Electron Density Calculations (particles/cm^3) Versus Distance (cm) Downstream of a Shock Front for Mach 15.6, 18.5, and 20.2 Using Modified Esch Thermodynamic Properties

electron production, hence, it is more likely to yield improved results in a sensitivity analysis. Perturbation of several reaction rate coefficients yielded significant reductions in peak values while having little effect on equilibrium calculations. For instance, a 5% decrease in the "N_r" coefficient for the $O + e- = 2e^- + O^+$ and $N + e- = 2e^- + N^+$ reaction paths resulted in a 45% reduction in peak electron concentrations at Mach 20.2. Much smaller peak reductions were observed at lower Mach numbers. Larger reductions in the "N_r" coefficient were ineffective. Perturbation of the rate coefficients for all other paths had little effect on the results. Finally, further reduction of peak values were obtained by deleting paths 21 through 29 in Table 2. These paths generated excessive quantities of electrons at the higher Mach numbers and had little effect on the non-ionized species (O,O_2,N,N_2,NO) . This version of the PM model (Table 7) yielded the best overall agreement with electron density measurements up to Mach 20.2 (Fig. 25) using the modified Esch thermodynamic properties.

68

Table 7. Modified Park and Menees Air Model

Reaction	M	A_r	N_r	E_r	
$O_2 + M \rightarrow O + O + M$	N	8.25×10^{19}	-1.0	59,500	
	O	8.25×10^{19}	-1.0	59,500	
	N_2	2.75×10^{19}	-1.0	59,500	
	O_2	2.75×10^{19}	-1.0	59,500	
	NO	2.75×10^{19}	-1.0	59,500	
$N_2 + M \rightarrow N + N + M$	N	1.11×10^{22}	-1.6	113,200	
	O	1.11×10^{22}	-1.6	113,200	
	N_2	3.7×10^{21}	-1.6	113,200	
	O_2	3.7×10^{21}	-1.6	113,200	Modified
	NO	3.7×10^{21}	-1.6	113,200	Park and Menees
					Air Model
$NO + M \rightarrow N + O + M$	N	4.6×10^{17}	-0.5	75,500	
	O	4.6×10^{17}	-0.5	75,500	
	N_2	2.3×10^{17}	-0.5	75,500	
	O_2	2.3×10^{17}	-0.5	75,500	
	NO	2.3×10^{17}	-0.5	75,500	
$NO + O \rightarrow N + O_2$		2.16×10^8	1.29	19,220	
$O + N_2 \rightarrow N + NO$		3.18×10^{13}	0.10	37,700	
$N + O \rightarrow NO^+ + e^-$		1.53×10^{10}	0.37	32,000	
$O + e^- \rightarrow O^+ + e^- + e^-$		1.95×10^{34}	-4.0 *	158,500	
$N + e^- \rightarrow N^+ + e^- + e^-$		1.25×10^{35}	-4.0 #	168,600	
$O + O \rightarrow O_2^+ + e^-$		3.85×10^{10}	0.49	80,600	
$O + O_2^+ \rightarrow O_2 + O^+$		6.85×10^{13}	-0.52	18,600	
$N_2 + N^+ \rightarrow N + N_2^+$		9.85×10^{12}	-0.18	12,100	
$N + N \rightarrow N_2^+ + e^-$		1.79×10^{10}	0.77	67,500	
$O + NO^+ \rightarrow NO + O^+$		2.75×10^{13}	0.01	51,000	
$N_2 + O^+ \rightarrow O + N_2^+$		6.33×10^{13}	-0.21	22,200	
$N + NO^+ \rightarrow NO + N^+$		2.21×10^{15}	-0.02	61,100	
$O_2 + NO^+ \rightarrow NO + O_2^+$		1.03×10^{16}	-0.17	32,400	
$NO^+ + N \rightarrow N + N_2^+$		1.70×10^{13}	0.40	35,500	

M represents the collision specie in a given reaction

* Originally - 3.78

Originally - 3.82

3.3.5 Transport Properties

The transport of specie momentum, thermal energy, and mass is characterized by the coefficient of viscosity (μ_s), thermal conductivity (λ_s), and (concentration) diffusion (D_{st}), respectively. Transport properties can have a considerable impact on nonequilibrium flow calculations. For instance, viscosity affects the growth of the

69
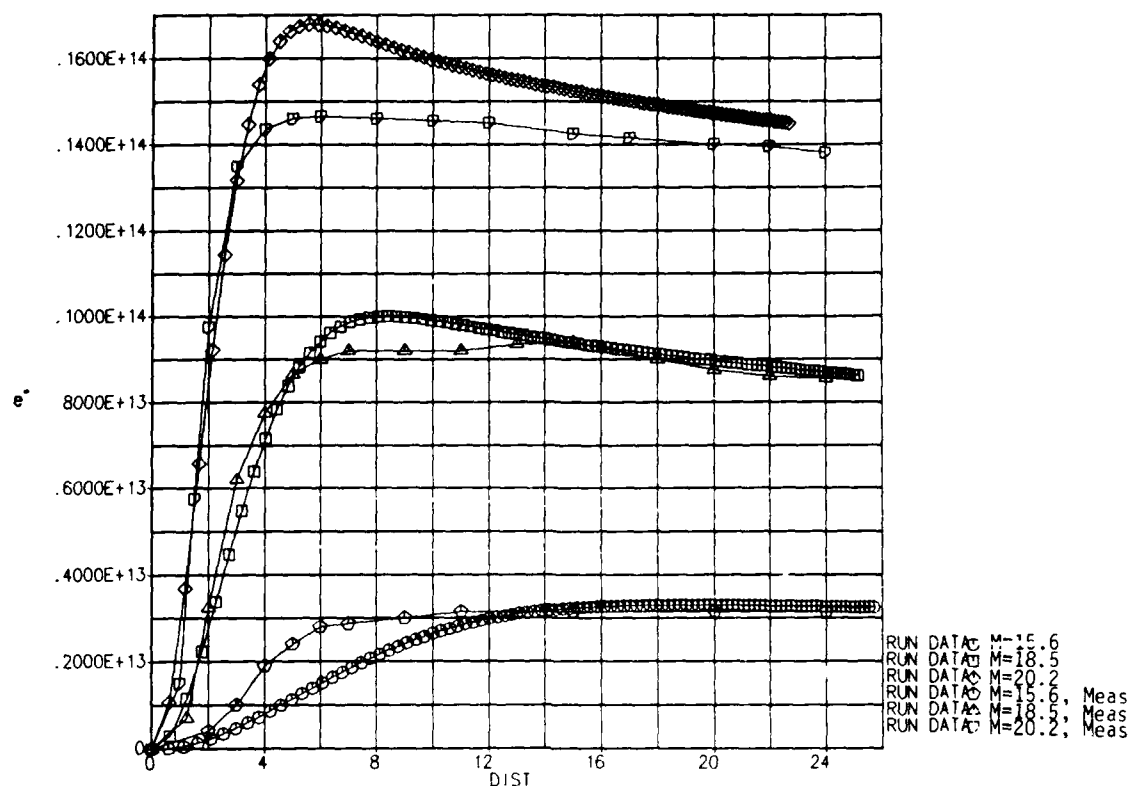
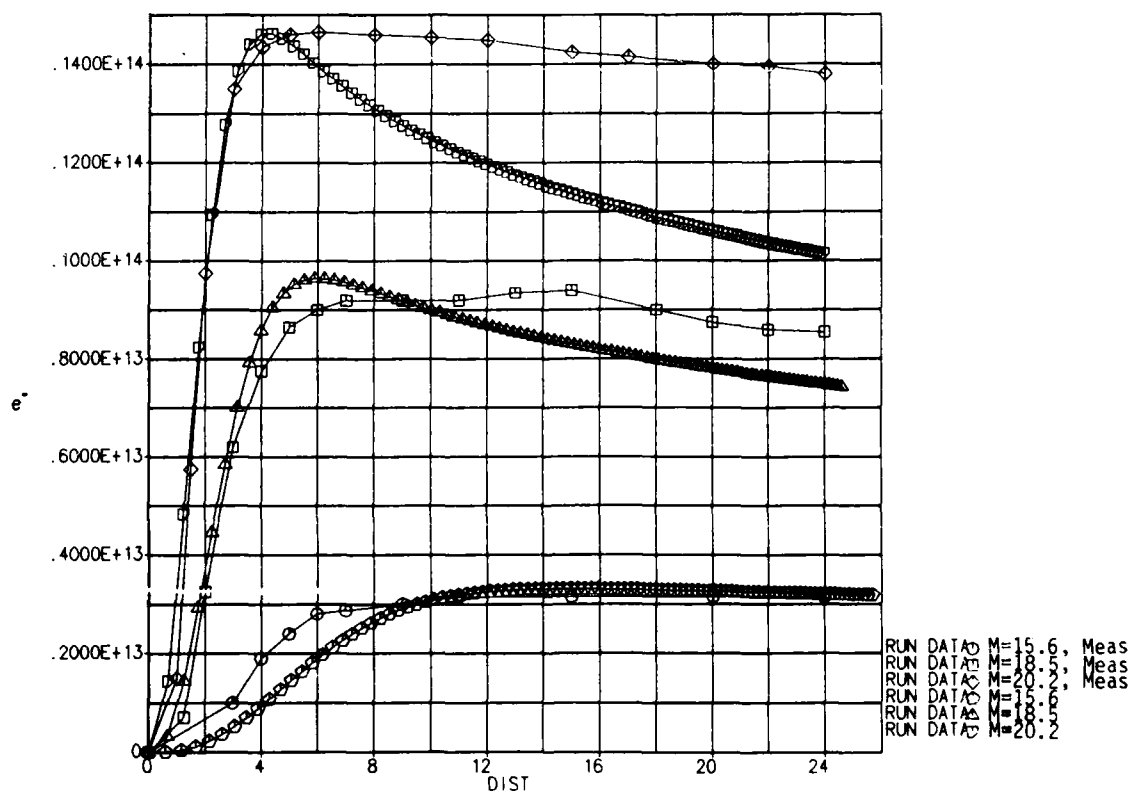*Figure 25. Modified PM Electron Density Calculations (particles/cm³) Versus Distance (cm) Downstream of Shock Front for Mach 15.6, 18.5, and 20.2 Using Modified Esch Thermodynamic Properties*

boundary layer, hence, influences the distance (and time) particles and energy must travel to reach the wall surface. Conversely, thermal conductivity regulates the transfer of heat, thus, influences particle motion (i.e. specie concentration). Finally, it will be shown that moderately accurate prediction methods are typically costly and lengthy.

All chemical nonequilibrium methods require the computation of each transport property for individual species in the reactive flowfield. A formula is then used to obtain the mixture value of the property. This procedure is depicted in Figure 26. Also shown is the functional dependence of each property on other parameters. It is worthy to note that all properties depend on the collision cross-section $\sigma^2 \Omega^{(l,m)}$ which is defined as the probable collision area between species s and t. The collision cross-section is dependent on specie mass, velocity, temperature, collision deflection angle, and an assumed potential force function. Details can be found in Ref. 34.

70

Calculation of the transport properties of individual species
$\mu_s = \mu_s \left[M_s, T, \sigma_s^2 \Omega_s^{(2,2)} (T) \right]$ $\lambda_s = \lambda_s \left[M_s, T, \sigma_s^2 \Omega_s^{(2,2)} (T), C_{p\,s} \right]$ $D_{st} = D_{st} \left[M_s, M_t, T, \sigma_{st}^2 \Omega_{st}^{(1,1)} (T), p \right]$

Calculation of the mixture value of each property
$\mu_{mix} = \mu_{mix} [\mu_s, C_s, M_s]$ $\lambda_{mix} = \lambda_{mix} [\lambda_s, C_s, M_s]$ $D_s = D_s [D_{st}, C_s, M_s]$

where
μ	=	viscosity
λ	=	thermal conductivity
D	=	concentration diffusion
s	=	chemical specie s
mix	=	mixture value
M	=	molecular weight
T	=	temperature
$\sigma^2 \Omega^{(l,m)}$	=	collision cross-section area
C_p	=	specific heat capacity at constant pressure
p	=	pressure
C	=	concentration

Figure 26. Typical Transport Properties Methodology

Specifically, first-approximations to the specie transport properties can be represented as follows (Ref. 34):

$$\mu_s = 266.93 \times 10^{-7} \frac{\sqrt{M_s T}}{\sigma_s^2 \, \Omega_s^{(2,2)*} (T)} \tag{38}$$

$$\lambda_s = 1989.1 \times 10^{-7} \frac{\sqrt{T/M_s}}{\sigma_s^2 \, \Omega_s^{(2,2)*} (T)} \tag{39}$$

$$p D_{st} = 2.628 \times 10^{-3} \frac{\sqrt{T^3 (M_s + M_t)/2 M_s M_t}}{\sigma_s^2 \, \Omega_{st}^{(1,1)*} (T)} \tag{40}$$

where $\sigma^2 \Omega^{(l,m)*}$ is the collision cross-section normalized to its rigid-sphere value. Equations (38) to (40) are based on kinetic theory of dilute gases and complete derivations are provided in Ref. 34.

Simplifications to Equations (38) to (40) have been developed by Tong (Ref. 35). The transport properties were curve-fitted with an equation of the form

$$Q = \exp\left[\alpha_s (\ln 1.8T)^2 + \beta_s (\ln 1.8T) + \gamma_s\right] \tag{41}$$

where Q represents μ_s, λ_s, pD_{st} and α_s, β_s, γ_s are the curve-fit coefficients. The coefficients for each specie property are listed in Tables 8 through 17. Equation (41) is accurate to within 0.5% of the source data which was generated from a computer program developed by Hatch (Ref. 36) and Pindroh (Ref. 37). The source data is valid up to 20,000K and this method will most likely reduce computation time and storage requirements. Note that Tong's method does include collisions with non-ionized and ionized species but has neglected coulomb effects (i.e. electron collisions). The effect of neglecting coulomb collisions can be evaluated during the Phase II validation test trials.

Once the specie transport properties are known a mixture value for each property may be obtained by one of several formulas. An excellent review of mixture relationships for thermal conductivity and viscosity are discussed in Refs. 38 and 39, respectively. In general, nonequilibrium mixture formulas involve the summation of the product (and/or quotient) of the specie concentration and its transport property for each specie in the flow. One of the simplest and straightforward method to compute the thermal conductivity is a linear mixing formula (Refs. 38, 40),

Table 8. Specie Dynamic Viscosity

Specie	α	β	γ
O	.03044	.2242	-11.04
O_2	-.01718	.9345	-13.69
NO	-.01578	.9147	-13.69
N	.03811	.09672	-10.49
NO^+	-.0153	4.856	-41.10
N_2	.0110	-16.14	50.39
N^+	-.1530	4.856	-41.48
O^+	-.1530	4.856	-41.41

$\ln \mu_s = \alpha (\ln 1.8T)^2 + \beta (\ln 1.8T) + \gamma$,

$\mu \left(\dfrac{gm}{cm\text{-}sec}\right)$, T (°K)

Table 9. Specie Thermal Conductivity

Specie	α	β	γ
O	.03045	.2242	-11.80
O_2	-.01718	.9346	-15.15
NO	-.01578	.9147	-15.08
N	.03811	.09674	-11.12
NO^+	-.1530	4.856	-42.49
N_2	1.097	-16.14	49.07
N^+	-.1530	4.856	-42.11
O^+	-.1530	4.856	-42.17

$\ln \lambda_s = \alpha (\ln 1.8T)^2 + \beta (\ln 1.8T) + \gamma$,

$\lambda \left(\dfrac{cal}{cm\text{-}sec\text{-}K}\right)$, T (°K)

Table 10. *Binary Diffusion Coefficient of Specie O Into Specie s*

Specie	α	β	γ
O	.03344	1.18750	-9.55591
O_2	.04139	1.07857	-9.65397
NO	.04060	1.09031	-9.70358
N	.01866	1.50710	-11.19786
NO^+	.04060	1.09031	-9.70358
N_2	.05342	.88732	-8.94594
N^+	.06302	.75995	-9.16222
O^+	.00169	1.55148	-11.69451

$$\ln (pD_{Os}) = \beta\,(\ln 1.8T)^2 + \beta\,(\ln 1.8T) + \gamma,$$

$$D_{Os}\left(\frac{cm^2}{sec}\right),\ p(atm),\ T\,(^\circ K)$$

Table 11. *Binary Diffusion Coefficient of Specie O_2 Into Specie s*

Specie	α	β	γ
O	.04139	1.07857	-9.65397
O_2	-.005643	1.77269	-12.49255
NO	-.000376	1.69266	-12.20127
N	-.009046	1.81422	-12.27983
NO^+	-.000376	1.69266	-12.20127
N_2	-.002632	1.64120	-11.99645
N^+	-.0090458	1.81422	-12.27983
O^+	.04139	1.07857	-9.65397

$$\ln (pD_{O_2s}) = \alpha\,(\ln 1.8T)^2 + \beta\,(\ln 1.8T) + \gamma,$$

$$D_{O_2s}\left(\frac{cm^2}{sec}\right),\ p(atm),\ T\,(^\circ K)$$

Table 12. *Binary Diffusion Coefficient of Specie NO Into Specie s*

Specie	α	β	γ
O	.040598	1.09031	-9.70358
O_2	-.000376	1.69266	-12.20127
NO	.0017725	1.66381	-12.10346
N	-.0097108	1.82599	-12.33594
NO^+	.0032396	1.56533	-12.42772
N_2	.022085	1.35095	-10.94333
N^+	-.0097108	1.82598	-12.33594
O^+	.040598	1.09031	-9.70358

$$\ln (pD_{NOs}) = \alpha\,(\ln 1.8T)^2 + \beta\,(\ln 1.8T) + \gamma,$$

$$D_{NOs}\left(\frac{cm^2}{sec}\right),\ p(atm),\ T\,(^\circ K)$$

Table 13. *Binary Diffusion Coefficient of Specie N Into Specie s*

Specie	α	β	γ
O	.018664	1.50710	-11.19786
O_2	-.0090458	1.81422	-12.27983
NO	-.0097108	1.82599	-12.33594
N	.028369	1.30193	-10.05754
NO^+	-.0097108	1.82599	-12.33594
N_2	.075705	.563218	-7.77918
N^+	.001265	1.55013	-11.64697
O^+	-.063017	.75995	-9.16222

$$\ln (pD_{Ns}) = \alpha\,(\ln 1.8T)^2 + \beta\,(\ln 1.8T) + \gamma,$$

$$D_{Ns}\left(\frac{cm^2}{sec}\right),\ p(atm),\ T\,(^\circ K)$$

Table 14. *Binary Diffusion Coefficient of Specie NO^+ Into Specie s*

Specie	α	β	γ
O	.04060	1.09031	-9.70358
O_2	-.000376	1.69266	-12.20127
NO	.0032394	1.56533	-12.42772
N	-.0097108	1.82599	-12.33594
NO^+	.0032394	1.56533	-12.42772
N_2	.022085	1.35095	-10.94333
N^+	-.0097108	1.82599	-12.33594
O^+	.040598	1.09031	-9.70358

$$\ln (pD_{NO^+s}) = \alpha\,(\ln 1.8T)^2 + \beta\,(\ln 1.8T) + \gamma,$$

$$D_{NO^+s}\left(\frac{cm^2}{sec}\right),\ p(atm),\ T\,(^\circ K)$$

Table 15. *Binary Diffusion Coefficient of Specie N_2 Into Specie s*

Specie	α	β	γ
O	.053422	.887319	-8.94594
O_2	.002632	1.64120	-11.99645
NO	.022085	1.35095	-10.94333
N	.075705	.563218	-7.77918
NO^+	.022085	1.35095	-10.94333
N_2	1.12800	-15.58970	52.74193
N^+	7.57048	.563218	-7.77918
O^+	.053422	.887319	-8.94594

$$\ln (pD_{N_2s}) = \alpha\,(\ln 1.8T)^2 + \beta\,(\ln 1.8T) + \gamma,$$

$$D_{N_2s}\left(\frac{cm^2}{sec}\right),\ p(atm),\ T\,(^\circ K)$$

Table 16. Binary Diffusion Coefficient of Specie N^+ Into Specie s

Specie	α	β	γ
O	.063017	.759948	-9.162217
O_2	-.0090458	1.81422	-12.27983
NO	-.0097108	1.825985	-12.33594
N	.001265	1.550133	-11.64697
NO^+	-.0097108	1.825985	-12.33594
N_2	.075705	.563218	-7.77918
N^+	.0012645	1.55013	-11.64697
O^+	.063017	.759948	-9.162217

$$\ln(pD_{N^+s}) = \alpha\,(\ln 1.8T)^2 + \beta\,(\ln 1.8T) + \gamma.$$

$$D_{N^+s}\left(\frac{cm^2}{sec}\right),\ p(atm),\ T\,(^\circ K)$$

Table 17. Binary Diffusion Coefficient of Specie O^+ Into Specie s

Specie	α	β	γ
O	.001690	1.55148	-11.69451
O_2	.041390	1.07857	-9.?5397
NO	.040598	1.09031	-9.70358
N	.0630167	.759948	-9.16222
NO^+	.040598	1.09031	-9.70358
N_2	.053422	.887319	-8.94594
N^+	.0630167	.759948	-9.16222
O^+	.0016898	1.55148	-11.69451

$$\ln(pD_{O^+s}) = \alpha\,(\ln 1.8T)^2 + \beta\,(\ln 1.8T) + \gamma.$$

$$D_{O^+s}\left(\frac{cm^2}{sec}\right),\ p(atm),\ T\,(^\circ K)$$

$$\Lambda_{mix} = M_{mix} \sum_{s=1}^{N_s} \frac{C_s}{M_s} \Lambda_s \ , \tag{42}$$

where C_s = mass fraction of specie s,

Λ_s = thermal conductivity of specie s,

M_s = molecular weight of specie s,

M_{mix} = mixture molecular weight.

Results obtained from Equation (42) are typically larger than experimental measurements (Refs. 38, 41-43). On the other hand, the reciprocal mixing rule,

$$\frac{1}{\Lambda_{mix}} = M_{mix} \sum_{s=1}^{N_s} \frac{C_s}{M_s \Lambda_s} \ , \tag{43}$$

yield results smaller than measured values (Ref. 43). Subsequently, Burgoyne and Weinberg (Refs. 38, 42) recommended combining Equations (42) and (43) to obtain

$$\Lambda_{mix} = \tfrac{1}{2}\left[M_{mix} \sum_{s=1}^{N_s} \frac{C_s \Lambda_s}{M_s} + \frac{1}{M_{mix} \sum_{s=1}^{N_s} \frac{C_s}{M_s \Lambda_s}} \right] \tag{44}$$

Equation (44) has been validated for rare gases (Ref. 44), Ar-He systems (Ref. 45), and polyatomic gases (Ref. 46) with moderate accuracy (less than 20% deviations). The simplicity of this expression makes it attractive for numerical programming.

For diatomic and polyatomic molecules λ_s must include effects due to internal degrees of freedom not present in monatomic species. A modified Eucken expression for the thermal conductivity is suggested (Ref. 47),

$$\lambda_{s,E} = \left[.352 \, \frac{C_{p_s} M_s}{R} + .12 \right] \lambda_s \quad , \tag{45}$$

where C_{p_s} = specie specific heat capacity,

 R $\;=\;$ universal gas constant.

The specie thermal conductivity can be shown to be directly proportional to the specie viscosity (based on first-order approximations, Ref. 34), hence, a relationship analogous to Equation (44) can be obtained for the dynamic viscosity,

$$\mu_{mix} = \tfrac{1}{2} \left[M_{mix} \sum_{s=1}^{N_S} \frac{C_s \mu_s}{M_s} + \frac{1}{M_{mix} \displaystyle\sum_{s=1}^{N_S} \frac{C_s}{M_s \mu_s}} \right] \quad . \tag{46}$$

The accuracy of Equation (46) is expected to be similar to its thermal conductivity counterpart.

Finally, the reciprocal of the mixture diffusion coefficient has been found to be approximately equal to the mass average of the reciprocal of the binary coefficient (Refs. 48, 49), that is,

$$D_{mix,t} = \frac{\displaystyle\sum_{s=1, s \neq t}^{N_S} C_s}{M_{mix} \displaystyle\sum_{s=1, s \neq t}^{N_S} \frac{C_s}{M_s D_{st}}} \quad . \tag{47}$$

Individual species formulas 38-40 and mixture Equations (44), (46), and (47) are the recommended relationships for determining the transport properties. These equations

may be utilized several million times in a complete three-dimensional, Navier-Stokes calculation about a simple geometry. The transport property process, therefore, requires considerable computational effort and cost-effectiveness/accuracy will be carefully assessed during Phase II. If necessary a scheme to discriminately employ these relationships at selected conditions (temperature ranges, locations) may be utilized to reduce computational effort. These equations also preclude the effects of chemical reactions (dissociations, recombinations) on the transport properties. Chemical reactions have a significant effect on the total thermal conductivity and a moderate influence on concentration diffusion at verv high temperatures (Ref. 37). To include these effects would require additional lengthy calculations and increase the total computation time. Nevertheless, the effectiveness of the above method to predict heat transfer and electron density histories can only be assessed during Phase II test trials.

3.4 WALL CATALYSIS

In this task the appropriate boundary conditions were developed to account for wall catalytic effects. Details of this procedure will depend on the numerical algorithm selected. In the nonequilibrium flow over a body at hypersonic speeds, the body surface may act as a catalyst for the recombination of atoms and ions, hence increasing the heat transfer at the surface. Reentry heating data derived from STS-2, STS-3, and STS-5 missions clearly showed the significance of nonequilibrium gas chemistry on aerodynamic heating in a high-velocity, low-density flight regime. As altitude and/or velocity is increased above STS reentry levels, nonequilibrium effects will become even more pronounced. Consequently, having the capability to treat chemical reactions, including surface kinetics, is essential in developing a flowfield code for treating high-speed, low-density flows.

The chemistry conditions considered at the wall include non-catalytic, finite rate, and fully-catalytic processes. Each condition is summarized below with reference to Figure 27:
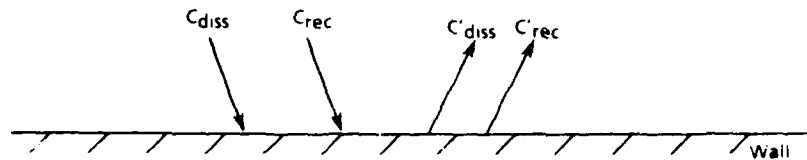
Figure 27. Specie Catalysis at the Wall Surface

Non-catalytic

$$C'_{diss} = C_{diss}$$

$$C'_{rec} = C_{rec}$$

Finite rate

$$C'_{diss} = A_{diss}C_{diss}, \quad 0 < A_{diss} < 1$$

$$C'_{rec} = B_{rec}C_{rec}, \quad 0 < B_{rec} < 1$$

Fully-catalytic

$$C'_{diss} = 0$$

$$C'_{rec} = C_{rec}|stoichiometric$$

where C =   specie concentration

         A_{diss}, B_{rec} = constants indicating the extent of finite rate wall catalysis

         diss   = dissociated species

         rec   = recombined species

At least two different types of thermal boundary conditions will be modeled. The first case involves specifying a constant, uniform wall temperature and the second case assumes the wall to be adiabatic. In both cases the degree of wall catalicity is variable.

IV. LEESIDE EFFECTS AND TURBULENCE MODELS

4.1 LEESIDE EFFECTS

4.1.1 Statement of Work

The objective of the leeside model task was to develop an improved flowfield model for leeward surfaces of hypersonic vehicles at angle-of-attack. An accurate determination of the aerothermal environment in these regions is needed to ensure an adequate thermal protection system/structural design, and to avoid the cost and performance penalties associated with over-design.

4.1.2 Background

When vehicle angle-of-attack is sufficient to separate the flow over leeside surfaces, vortices are formed that can strongly influence heating patterns. These leeside flows are highly sensitive to vehicle geometry, angle-of-attack, and Reynolds number, and have proven very difficult to analyze.

To minimize empiricism in the present analysis (and thus increase reliability and generality), the Phase I leeside flow analysis attempted to calculate leeside flows directly, without adding any empiricism over and above that introduced by the turbulence models to be discussed in Section 4.2. Minimizing empiricism was considered important since the sensitivity exhibited by leeside flows studied to date suggests that direct extrapolations to flight conditions may not be very reliable. An additional advantage of the current (direct) approach is that it facilitates the inclusion of chemical reaction effects in the leeside vortices.

4.1.3 Technical Development

The standard Baldwin-Lomax turbulence model (Ref. 50) has been widely applied to computing supersonic turbulent flowfields around conical bodies at low and moderate angles of attack. Good agreement between computed results and experimental data can

be obtained except in the leeside region where vortex flow separation occurs. The reasons for this discrepancy are twofold: improper determination of the turbulence length scale and poor grid resolution incapable of handling the leeside vortex flow structure.

The major difficulty encountered in the leeside computation is the determination of the proper length scale upon which to base the change in the eddy viscosity calculation from the formula valid in the inner region to that in the outer. In the original Baldwin-Lomax model this length scale, y_{max}, was determined as the y value for which F(y) below was a maximum:

$$F(y) = \omega y [1 - \exp(-y^+/26)], \qquad (48)$$

where ω is the vorticity, y is the distance normal to the wall, and y^+ is the law-of-the-wall coordinate. In the leeside region vortex flow separation causes F(y) to have two or more maxima. The original Baldwin-Lomax formulation would choose the second maximum, yielding an improperly high value of outer eddy viscosity. Degani and Schiff (Ref. 51) suggested a modification to the Baldwin-Lomax model, choosing invariably the first maximum of F(y) in the leeside region (Fig. 28). Using grids with adequate resolution for the leeside vortices, they applied the modified Baldwin-Lomax model to supersonic flows around various ogive-cylinder bodies and cones at high angle-of-attack. The computed results thus obtained were in good agreement with the experiment data
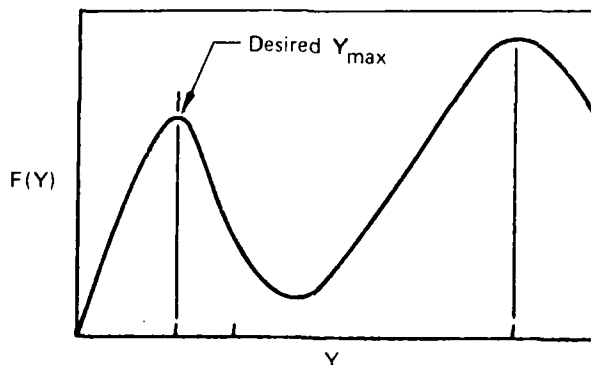

Figure 28. Behavior of Leeside Function F (Y) at High Angle-of-Attack

even in the leeside region.   Figures 29, 30 show some typical results obtained by

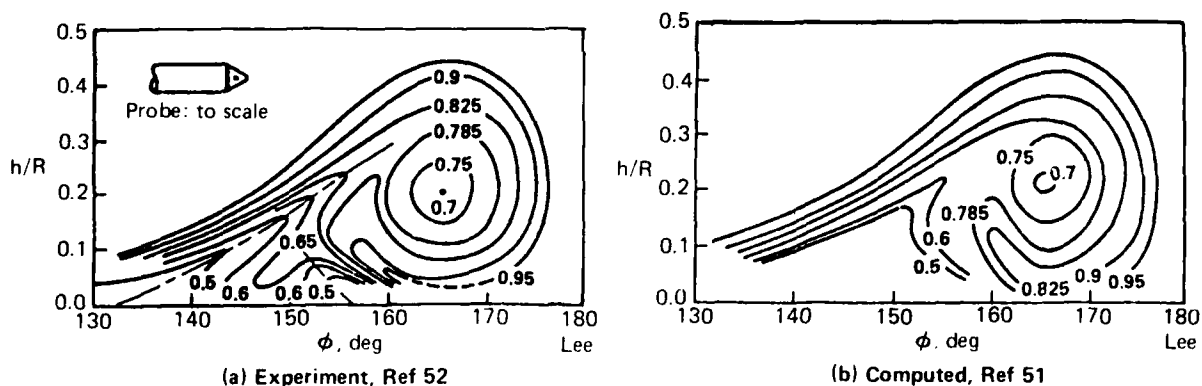Rainbird (Ref. 52) using the modified Baldwin-Lomax formulation.

(a) Experiment, Ref 52   (b) Computed, Ref 51

Figure 29. Normalized Pitot-Pressure Contours in Flowfield for a Yawed 5-deg Cone
$(M_\infty = 1.8, \alpha = 12.5\text{-deg}, Re_x = 28.9\ (10^6))$
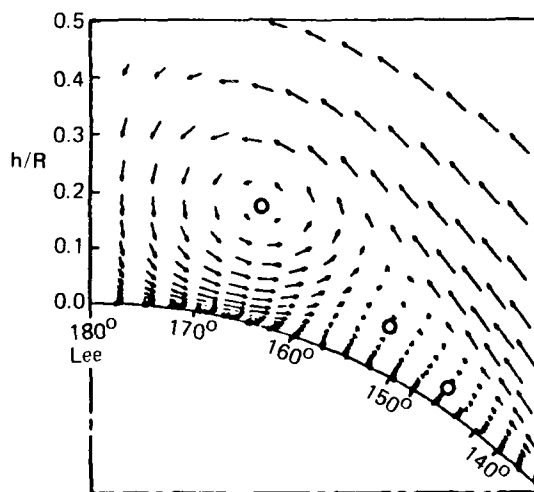
Figure 30. Computed Crossflow Plane Velocity Vectors on a 5-deg Cone
$(M_\infty = 1.8, \alpha = 12.5\text{-deg}, Re_x = 28.9\ (10^6))$

It is concluded that using the Baldwin-Lomax model with Degani-Shiff

modifications is adequate to compute the flowfield on the leeside region of a body at

various angles of attack and mach numbers, and should be sufficient to satisfy the

leeside calculation requirements of the present contract.

Part of the work performed for this task included a literature review to identify

data sets that could be used to evaluate the leeside calculation capability of the code to

be developed during Phase II. Six candidate cases have been identified, and are listed in

Table 18 below. These cases span a wide range of Mach number/angle-of-attack combinations, and should provide an adequate supply of test results to compare against. These cases will be supplemented during Phase II if necessary, and if new test data is identified.

Table 18. Candidate Leeside Evaluation Cases

Configuration	Flight condition		Reference
	α, deg	Mach	
5° sharp cone	12 5	1.8, 4 25	52
5.6° sharp cone	2 to 18	14.2	53
9° sharp cone	0 to 20	7 0	54
15° sphere cone	-5 to 15	5 25, 7 40, 10 6	55
12.8/7° biconic	-10 to 40	6 0	56
13°/7° biconic	0 to 10	10 0	57

4.2 TURBULENCE MODELS

4.2.1 Statement of Work

The high-altitude, low-density (and thus low Reynolds number) flows to be considered in the current contract will be primarily laminar flows. In the late phase of re-entry, however, transition to turbulence will occur. Therefore, a contract requirement was to include at least one turbulence model. This model was, in principal, separate from the leeside turbulence model.

4.2.2 Background

The turbulence expected for the case of interest in this contract will include shear layer type turbulence on the windward side of the re-entry vehicle as well as vortex separated flows on the leeward side of the vehicle. Windward turbulence of the shear layer type is expected to occur as a shock/boundary layer interaction at a deflected control surface, for example. This shear layer type turbulence is relatively simple to model, even with basic algebraic turbulence models such as the Baldwin-Lomax (Ref. 50) model. For the Phase I work described here, both algebraic and two-equation turbulence models were studied. Leeside models were discussed in Section 4.1.

4.2.3 Technical Development

Extensive literature review indicated that the standard Baldwin-Lomax eddy viscosity turbulence model (Ref. 50) has been successfully used in wide ranges of applications in computational fluid dynamics. This algebraic turbulence model is relatively simple to implement and gives accurate results in transonic and supersonic flows without separation. Its accuracy deteriorates somewhat in flows with separation but nonetheless it still gives acceptable results in many engineering applications. As the first step of this task the standard Baldwin-Lomax turbulence model was installed into the prototype three-dimensional explicit Navier-Stokes code. The implementation was validated under independent research and development funding using two-dimensional viscous transonic flows around airfoils. Excellent agreement between the computed results and wind tunnel data were obtained (Ref. 58).

In order to study the option of a more sophisticated turbulence model for flows in the hypersonic Mach number range, a literature review was carried out with emphasis on two-equation models. In general, two-equation turbulence models show a slight improvement over the standard Baldwin-Lomax model for computing the flowfields at the flight conditions prescribed in this contract. The slight improvement in solution thus gained, however, may not be very cost-effective due to the nature of the expected flowfields and the severe computational cost penalty associated with two-equation formulation.

One candidate turbulence model for possible inclusion in the code is the Jones-Launder model. This model was introduced in 1972 (Ref. 59) and has proved very popular among two-equation models. The Jones-Launder model adds one partial differential equation for the turbulent kinetic energy and one for the energy dissipation rate. A comparison of the Jones-Launder model with other turbulence models for many of the expected flows mentioned above is reported by Viegas and Horstman (Ref. 60). In this paper, the Jones-Launder model was compared with the Wilcox-Rubesin two-equation model (Ref. 61), the Viegas one-equation model (Ref. 62), and the Baldwin-

Lomax (Ref. 50) model for a variety of flow problems. As expected, the two-equation models generally yielded better results.

The recent approach of adding wall functions to the turbulence models has circumvented the need for clustering many grid points near solid surfaces. The reduced grid clustering permits longer time steps to be taken and improves computational efficiency. A typical wall function was suggested by Viegas and Rubesen (Ref. 63). Results of calculations using this wall function with the Jones-Launder model compared to those using the Baldwin-Lomax model for a compression ramp test case are reported by Knight, et. al. (Ref. 64). The combination of the two-equation model together with the wall-function boundary conditions yields slightly better results in general. The computational time required, however, is higher and the complexity of the code will be greatly increased. Therefore, it is not recommended that a two-equation turbulence model be added to the Navier-Stokes code under development.

V. CONCLUSIONS AND RECOMMENDATIONS

The Phase I effort of the current contract was intended to identify components of a combined fluid dynamic/chemistry solution algorithm for calculating low density real gas flows about hypersonic vehicles. It is believed that, by utilizing results of related Air Force funded research and Boeing project and research work, the Phase I study was more thorough than originally planned. In particular, results from Air Force contracts AFOSR-85-0372 and F33315-86-C-3015 supporting research work at Stanford University under Professor R. W. MacCormack, and Air Force contract F04611-86-C-0015 awarded to Boeing Aerospace Company for the development of an advanced Navier-Stokes rocket base flow calculation capability, have proved most useful for the current contract effort. The combined results of these supporting contracts and the development work performed in Phase I of this contract will provide a strong basis for the Phase II program development effort.

At the start of this contract it was believed that, in the present computer hardware environment, software portability would play a major role in the long-range success of the code to be developed. Experience gained during the Phase I effort, in particular during the evaluation of vectorization and parallel processing requirements, has served to reinforce the importance of portable software systems.

Sections II-IV have discussed in detail the conclusions derived from the Phase I technical effort in the areas of solution algorithm and chemistry model development, turbulence modeling, leeside modeling and wall catalysis. The recommendations derived from the Phase I conclusions for application to the Phase II program development effort are summarized below:

- Target Computers: Cray X-MP/Y-MP and Cray 2/3
- Multiprocessing: Cray microtasking

- **Algorithm:**   Fully coupled chemistry

                      Implicit formulation with flux splitting

                      Gauss-Seidel line relaxation solution procedure

- **Chemistry:**   Modified Park and Menees air chemistry model with 9
                      species and 20 reaction paths

                      Modified Esch thermodynamic properties up to 15,000 K

                      Tong simplification of Pindroh model for transport
                      properties

- **Turbulence Model:**   Modified Baldwin-Lomax model

Basing the Phase II program development effort upon the above recommendations will result in computer program capable of accurately and efficiently predicting trends in the heating rates, pressures, forces, and moments on complex shapes in low-density reacting gas hypersonic flows.

REFERENCES

1. MacCormack, R. W., "Current Status of Numerical Solutions of the Navier-Stokes Equations," AIAA Paper 85-0032, AIAA 23rd Aerospace Sciences Meeting, January 1985.

2. MacCormack, R. W., and Candler, G. V., "The Solution of the Navier-Stokes Equations Using Gauss-Seidel Line Relaxation," to be published.

3. Anderson, J. D., "A Survey of Modern Research in Hypersonic Aerodynamics," AIAA Paper 84-37983.

4. Power, G. D., and Barber, T. J., "Analysis of Complex Hypersonic Flows with Strong Viscous/Inviscid Interaction," AIAA Paper 87-1189, AIAA 19th Fluid Dynamics, Plasma Dynamics and Lasers Conference, June 1987.

5. Barnett, M., and Davis, R. T., "A Procedure for the Calculation of Supersonic Flows with Strong Viscous-Inviscid Interaction," AIAA Paper 85-0166, January 1985.

6. Pulliam, T. H., "Euler and Thin Layer Navier-Stokes Codes: ARC2D, ARC3D," Notes for Computational Fluid Dynamics User's Workshop, University of Tennessee Space Institute, Tullahoma, TN, March 12-16, 1984.

7. Beam, R. M., and Warming, R. F., "An Implicit Factored Scheme for the Compressible Navier-Stokes Equations," **AIAA Journal**, Vol. 16, No. 4, pp 393-402, 1978.

8. Beam, R. W., and Warming, R. F., "An Implicit Finite-Difference Algorithm for Hyperbolic Systems in Conservation-Law Form," *Journal of Computational Physics,* Vol. 22, pp 87-110, 1976.

9. MacCormack, R. W., "The Effect of Viscosity in Hypervelocity Impact Cratering," AIAA Paper 69-354, 1969.

10. Shinn, J. L., Yee, H. C., and Uenishi, K., "Extension of a Semi-Implicit Shock-Capturing Algorithm for 3-D Fully Coupled, Chemically Reacting Flows in Generalized Coordinates," AIAA Paper 87-1577, AIAA 22nd Thermophysics Conference, June 1986.

11. Yee, H. C., and Shinn, J. L., "Semi-Implicit and Fully Implicit Shock-Capturing Methods for Hyperbolic Conservation Laws with Stiff Source Terms," NASA Technical Memorandum 89415, December 1986.

12. Jameson, A., Schmidt, W., and Turkel, E., "Numerical Solutions of the Euler Equations by Finite Volume Methods Using Runge-Kutta Time-Stepping Schemes," AIAA Paper 81-1259, AIAA 14th Fluid and Plasma Dynamics Conference, 1981.

13. Yee, H. C., "Upwind and Symmetric Shock-Capturing Schemes," NASA Technical Memorandum 89464, May 1987.

14. Steger, J. L., and Warming, R. F., "Flux Vector Splitting of the Inviscid Gasdynamic Equations with Application to Finite-Difference Methods," *Journal of Computational Physics,* Vol. 40, pp 263-293, 1981.
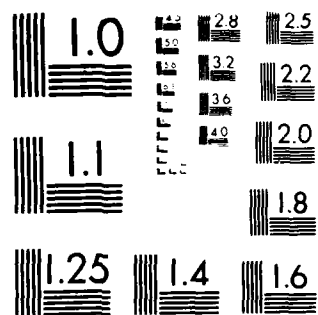
MICROCOPY RESOLUTION TEST CHART

NATIONAL BUREAU OF STANDARDS 1963-A

15. "Equations, Tables, and Charts for Compressible Flow," NACA Report 1135, 1953.

16. Liepmann, H. W., and Roshko, A., Elements of Gasdynamics, New York: John Wiley and Sons, Inc., p 105, 1957.

17. Cray Microtasking Workshop, May 1987.

18. Bussing, T. R. A., "A Finite Volume Method for the Navier-Stokes Equations with Finite Rate Chemistry," MIT Doctorate Thesis, 1985.

19. Williams, A. F., Combustion Theory, Addison-Wesley, 1965.

20. Drummond, J. P., Hussaini, M. Y., Zang, T. A., "Spectral Methods for Modeling Supersonic Chemical Reacting Flow Fields," AIAA Paper 85-0302, 1985.

21. Vincenti, W. G., Kruger, C. H. J., Introduction to Physical Gas Dynamics, Robert Krieger Publishing Co., 1962.

22. Wagner, P. P., Nonequilibrium Flows, Marcel Dekker, 1970.

23. Camac, M. and Feinberg, R. M., "Formation of NO in Shock-Heated Air," 11th Symposium (International) on Combustion, 1966.

24. Lin, S., Neal, R., and Fyfe, W., "Rate of Ionization Behind Shock Waves in Air. Part I. Experimental Results," Physics of Fluids, Vol. 5., No. 12, 1962.

25. Teare, J.D., Georgiev, S., Allen, R.A., "Radiation from the Nonequilibrium Shock Front," **Hypersonic Flow Research,** Vol. 7, 1962.

26. Wray, K., "Chemical Kinetics of High Temperature Air," **Hypersonic Flow Research,** Vol. 7, 1962.

27. Park, C. and Menees, G.P., "Odd Nitrogen Production by Meteoroids," **Journal of Geophysical Research,** Vol. 83, No. C8, 1978.

28. Kang, S.W., and Dunn, M. G., "Theoretical and Experimental Studies of Reentry Plasmas," NASA CR-2232, 1973.

29. Bittker, D. A., and Scullin, V. J., "GCKP84-General Chemical Kinetics Code for Gas-Phase Flow and Batch Processes Including Heat Transfer Effects," NASA Paper 2320, 1984.

30. Bortner, M. H., "A Review of Rate Constants of Selected Reactions of Interest in Reentry Flow Fields in the Atmosphere," National Bureau of Standards Technical Note 484, 1969.

31. Esch, D., Siripong, A., and Pike, R., "Thermodynamic Properties in Polynomial Form for Carbon, Hydrogen, and Oxygen Systems from 300K - 30000 K," NASA-RFL-TR-70-3, 1970.

32. Shinn, J., Personal Communication, NASA Langley Research Center, Hampton, Virginia.

33. Lin, S. and Teare, J. D., "Rate of Ionization Behind Shock Waves in Air. Part 2. Theoretical Interpretations," **Physics of Fluids,** Vol. 6., No. 3, 1963.

34. Hirschfelder, J. O., Curtiss, C. F., Bird, R. B., <u>Molecular Theory of Gases and Liquids,</u> John Wiley and Sons, 1954.

35. Tong, H., "Simplified Analytic Functions for the Calculation of Thermodynamic and Transport Properties," Boeing Document D2-113328-1, 1966.

36. Hatch, D. J., "Generalized Program for High Temperature Gas Transport Properties," The Boeing Company, AS-2112, 1964.

37. Pindroh, A. L., "Transport Properties of an Arbitrary High Temperature Gas Mixture," *Boeing* Document D2-36120-1, 1967.

38. Touloukian, Y. S., et. al., "Thermal Conductivity," **Thermophysical Properties of Matter,** Vol. 3, 1970.

39. Touloukian, Y. S., et. al., "Viscosity," **Thermophysical Properties of Matter,** Vol. 11, 1975.

40. Kennard, E. H., <u>Kinetic Theory of Gases with Introduction to Statistical Mechanics,</u> McGraw-Hill, 1938.

41. Brokaw, R. S., "Estimating Thermal Conductivity for Nonpolar Gas Mixtures Simple Empirical Methods," **Ind. Eng. Chem.,** Vol. 47, 1955.

42. Burgoyne, J. H., Weinberg, F., "A Method of Analysis of a Plane Combustion Wave," Fourth Symposium on Combustion, 1953.

43. Gandhi, J. M., Saxena, S. C., "Thermal Conductivity of Multicomponent Mixtures of Inert Gases: Part III- Some Simpler Methods of Computation," **Indian J. Pure Appl. Phys.**, Vol. 4, No. 12, 1966.

44. Mathur, S., Tondon, P. K., Saxena, S. C., "Thermal Conductivity of the Gas Mixtures: D_2-Xe, D_2-Ne-Kr, D_2-Ne-Ar, D_2-Ar-Kr-Xe," **J. Phys. Soc. Japan**, Vol. 25, No. 2, 1968.

45. Saxena, S. C., Discussion on the paper "High Temperature Thermal Conductivity of Rare Gases and Gas Mixtures," **J. Heat Transfer,** Tran. ASME, Vol. 90C, 1968.

46. Gupta, G. P., Mathur, S. Saxena, S. C., "Certain Methods for Calculating Thermal Conductivity of Multicomponent Mixtures Involving Polyatomic Gases," **Defense Sci. J.,** Vol. 18, No. 4, 1968.

47. Svehla, R. A., "Estimated Viscosities and Thermal Conductivities of Gases at High Temperatures," NASA TR-R-132, 1962.

48. Kee, R. J., Warnatz, J., Miller, J. A., "A Fortran Computer Code Package for the Evaluation of Gas-Phase Viscosities, Conductivities, and Diffusion Coefficients," Sandia Lab Report SAND 83-8209, 1983.

49. Curtiss, C. F., Hirschfelder, J. O., " Transport Properties of Multicomponent Gas Mixtures," **J. Chem. Phys.,** Vol. 12, No. 6, 1949.

50. Baldwin, B. S., and Lomax, H., "Thin Layer Approximation and Algebraic Model for Separated Turbulent Flows," AIAA Paper 78-0257, January 1978.

51. Degani, D. and Shiff, L. B., "Computation of Supersonic Viscous Flows Around Pointed Bodies at Large Incidence," AIAA Paper 83-0034, January 1983.

52. Rainbird, W. J., "The External Flow Field about Yawed Circular Cones," AGARD Conference Proceeding No. 30, May 1986.

53. Stetson, K. F., "Boundary-Layer Separation on Slender Cones at Angle of Attack," **AIAA Journal,** Vol. 10, No. 5, pp 642-648, May 1972.

54. Marcillat, J., and Roux, B., "Experimental and Theoretical Study of Supersonic Viscous Flow over a Yawed Circular Cone," **AIAA Journal,** Vol. 10, No. 12, pp 1625-1630, Dec. 1972.

55. Cleary, J. W., "Effects of Angle of Attack and Nose Bluntness on the Hypersonic Flow over Cones," AIAA-66414, AIAA 4th Aerospace Sciences Meeting, June 1966.

56. Miller, C. G., and Gnoffo, P. A., "An Experimental Investigation of Hypersonic Flow over Biconics at Incidence and Comparison to Prediction," AIAA-82-1382, AIAA 9th Atmospheric Flight Mechanics Conference, August 1982.

57. Miller, C. G., Gnoffo, P. A., Wiler, S. E., "Measured and Predicted Heating Distributions for Biconics at Mach 10," **Journal of Spacecraft,** Vol. 23, No. 3, pp 251-258, May-June 1986.

58. Chan, J. S., "Multizone Navier-Stokes Computations of Viscous Transonic Flows Around Airfoils," AIAA Paper 88-0103, January 1988.

59. Jones, W. P., and Launder, B. E., "The Prediction of Laminarization with a Two-Equation Model of Turbulence," *International Journal of Heat and Mass Transport*, Vol. 15, pp. 301-414, 1972.

60. Viegas, J. R., and Horstman, C. C., "Comparison of Multiequation Turbulence Models for Several Shock Boundary-Layer Interactions," **AIAA Journal**, Vol. 17, pp. 811-820, August 1979.

61. Wilcox, D. C., and Rubesin, M. W., "*Progress in Turbulence Modeling for Complex Flow Fields, Including Effect of Compressibility*," NASA TN 1517, 1980.

62. Viegas, J. R., and Horstman, C. C., "Comparison of Multiequation Turbulence Models for Several Shock Separated Boundary-Layer Interaction Flows," AIAA Paper 78-1165, July 1978.

63. Viegas, J. R. and Rubesin, M. W., "Wall-Function Boundary Conditions in the Solution of the Navier-Stokes Equations for Complex Compressible Flows," AIAA Paper 83-1694, July 1983.

64. Knight, D., Horstman, C. C., Ruderich, R., Mao, M.-F., and Bogdonoff, S., "Supersonic Turbulent Flow Past a 3-D Swept Compression Corner at Mach 3," AIAA Paper 87-0551, January 1987.

ABBREVIATIONS

ADI	alternating direction implicit
AFB	Air Force Base
BAC	Boeing Aerospace Company
Bit	Bittker air chemistry model
Bort	Bortner air chemistry model
CFD	computational fluid dynamics
FNS	full Navier-Stokes
GS	Gauss-Seidel
KD	Kang-Dunn air chemistry model
NS	Navier-Stokes
PM	Park-Menees air chemistry model
PNS	parabolized Navier-Stokes
RFP	request for proposal
RNS	reduced Navier-Stokes
TLNS	thin layer Navier-Stokes
TVD	total variation diminishing
W	Wray air chemistry model
2D	two-dimensional
3D	three-dimensional

NOMENCLATURE

Math Symbols

∂	=	partial derivative
$D+$	=	forward difference
$D-$	=	backward difference
$D\pm$	=	alternating forward and backward differences
exp	=	exponential
ln	=	natural logarithm
Δt	=	time increment
∞	=	infinity
Σ	=	summation
δU^{n+1}	=	implicit change in solution vector
ΔU^n	=	explicit change in solution vector
$\rightleftharpoons$	=	forward-backward chemical reaction
$\rightarrow$	=	forward chemical reaction
$\rightharpoonup$	=	vector
$\int$	=	integral
$\sqrt{}$	=	square root
$\prod\limits_{s=1}^{N_S}$	=	product of terms with index from $s = 1$ to $s = N_S$

Units

m/s	=	meters per second
ft/s	=	feet per second
N/m^2	=	Newtons per square meter
lbf/ft^2	=	pound-force per square foot
K	=	Kelvin

°R	=	degrees Rankine
cm	=	centimeters
cal	=	calories
sec	=	seconds
atm	=	atmospheres
km	=	kilometers
m	=	meters

Subscripts

i, j, k	=	coordinate index discretizations
r	=	r-th reaction
s, t	=	species designators
inv	=	inviscid
vis	=	viscous
max	=	maximum

Superscripts

'	=	refers to physical (nontransformed) flux vectors
+	=	positive eigenvalue contributions (except for y^+ in Equation 48)
~	=	negative eigenvalue contributions (except for e^- electron designation)
n	=	time level discretization
T	=	vector transpose
$\wedge$	=	refers to diffusion velocities

Greek Symbols

α_v	=	absorption coefficient (Equation 31)
$\alpha_s, \beta_s, \gamma_s$	=	curve-fitted coefficients for the specie transport properties (Equation 41)
ξ, η, ζ	=	general curvilinear coordinates
ξ_x, ξ_y, ξ_z	=	metrics of the general curvilinear transformation
η_x, η_y, η_z	=	metrics of the general curvilinear transformation
$\zeta_x, \zeta_y, \zeta_z$	=	metrics of the general curvilinear transformation
$\sigma^2_{st}\Omega_{st}^{(l, m)*}$	=	collision cross-sectional area between species s and t, normalized to its rigid sphere value (Equations 38-40)
Θ_v	=	characteristic vibration temperature (Equation 28)
$\Lambda_A, \Lambda_B, \Lambda_C$	=	diagonal matrices of the eigenvalues of A, B, C, respectively
λ	=	thermal conductivity
μ	=	dynamic viscosity
μ_B	=	bulk viscosity $= -\frac{2}{3}\mu$
v	=	frequency (Equation 27)
ρ	=	total density
τ	=	shear stress
ω	=	vorticity
$\dot{\omega}$	=	specie net production rate

English Symbols

a_{rs}, b_{rs}	=	stoichiometric coefficients of the reactants and products, respectively, for specie s in the r-th reaction path (Equation 15)
$a_0, a_1, a_2, a_3, a_4, a_5, a_6$	=	coefficient matrices for the linearized 3D Navier-Stokes finite difference algorithm
A, B, C	=	Jacobians of the flux vectors F, G, H, respectively

A_r, N_r, E_r	=	Arrhenius rate for r-th reaction path (Equation 19)
B_v	=	Planck's function (Equation 32)
c	=	speed of light
C	=	specie concentration
C_p	=	specific heat capacity at constant pressure
D_{st}	=	(concentration) diffusion coefficient of specie s into specie t
e^-	=	electron
e	=	total energy per unit volume = $\rho[e_i + \frac{1}{2}(u^2+v^2+w^2)]$
e_i	=	total internal energy per unit mass = $e_{diss}+e_{elect}+e_{kin}+e_{rot}+$ $e_{trans}+e_{vib}$
e_{diss}	=	internal energy per unit mass due to dissociation
e_{elect}	=	internal energy per unit mass due to electrons
e_{kin}	=	internal energy per unit mass due to kinetic energy
e_{rot}	=	internal energy per unit mass due to rotation
e_{trans}	=	internal energy per unit mass due to translation
e_{vib}	=	internal energy per unit mass due to vibration
e^*_{vib}	=	equilibrium vibrational internal energy per unit mass
f	=	Gibb's free energy (Equation 36)
F(y)	=	function in the Baldwin-Lomax turbulence model
F, G, H	=	x, y, z momentum flux vectors for the Navier-Stokes equations
F_ξ, F_η, F_ζ	=	transformed components of Navier-Stokes x-momentum viscous flux
G_ξ, G_η, G_ζ	=	transformed components of Navier-Stokes y-momentum viscous flux
H_ξ, H_η, H_ζ	=	transformed components of Navier-Stokes z-momentum viscous flux
h_s	=	specie enthalpy

I	=	identity matrix
I_v	=	intensity
J	=	Jacobian of general curvilinear coordinate transformation
k_B	=	Boltzmann's constant (Equation 28)
k_{fr}, k_{br}	=	forward and backward reaction rates, respectively, for the rth reaction path (Equation 15)
k_p	=	Planck's constant (Equation 27)
K_{eq}	=	k_{fr}/k_{br} = equilibrium constant for the rth reaction (Equation 37)
l_i	=	unit vector in the direction of I_v
M	=	specie molecular weight
N	=	total number of harmonic oscillators (Equation 27)
N_c	=	matrix relating coupled Navier-Stokes/chemistry conservative and nonconservative solution vectors
N_f	=	matrix relating fluid dynamic (Navier-Stokes) conservative and nonconservative solution vectors
N_R	=	total number of chemical reaction paths
N_S	=	total number of chemical species
p	=	pressure
q	=	heat flux
R	=	universal gas constant
S	=	entropy (Equation 35)
S_A, S_A^{-1}	=	similarity matrices which diagonalize the flux Jacobian A
S_B, S_B^{-1}	=	similarity matrices which diagonalize the flux Jacobian B
S_C, S_C^{-1}	=	similarity matrices which diagonalize the flux Jacobian C
t	=	time
T	=	temperature
U	=	conservative solution vector = $[\rho, \rho u, \rho v, \rho w, e]^T$

u, v, w	=	cartesian components of velocity
$\hat{u}, \hat{v}, \hat{w}$	=	cartesian components of specie diffusion velocities
V	=	nonconservative solution vector = $[\rho, u, v, w, e_j]^T$
$\dot{\mathbf{W}}$	=	chemistry source term vector = $[\dot{\omega}_1, ..., \dot{\omega}_{N_S}, 0, 0, 0, 0]^T$
x, y, z	=	cartesian coordinate system
y^+	=	law-of-the-wall coordinate
Z	=	curve-fitted coefficients for the thermodynamic properties
		(Equations 33-36)

ATE
LMED
8